ABSTRACT

Convection from Laser-Scanned Ice Roughness
at Multiple Accretion Event Times

Jaime Lynn McCarrell, M.S.M.E.

Mentor: Stephen T. McClain, Ph.D.

Ice accretions degrade aircraft flight safety and performance by decreasing the lift and stall angle, increasing the drag, and increasing the aircraft weight. A recent study found that the commonly used realistic ice roughness models did not replicate the convective heat transfer results of one real ice roughness surface. The current study characterizes the convective heat transfer of four ice roughness surfaces exposed to accelerating flow similar to that experienced by a NACA 0012 airfoil and flow with negligible acceleration. The velocity boundary layer development along these surfaces was characterized as well. Each of the roughness surfaces was exposed to similar supercooled cloud conditions for different lengths of time to observe the changes in convective heat transfer with increasing accumulation parameter. The ice surfaces for this study were created from geometrically unwrapped laser scans of ice accretions to form a flat plate representation of the airfoil surface roughness.

Convection from Laser-Scanned Ice Roughness at Multiple Accretion Event Times

by

Jaime Lynn McCarrell, B.S.M.E.

A Thesis

Approved by the Department of Mechanical Engineering

Kenneth Van Treuren, Ph.D., Chairperson

Submitted to the Graduate Faculty of
Baylor University in Partial Fulfillment of the
Requirements for the Degree
of
Master of Science in Mechanical Engineering

Approved by the Thesis Committee

Stephen T. McClain, Ph.D., Chairperson

Jill Klentzman, Ph.D.

Randall Jean, Ph.D.

Accepted by the Graduate School

December 2017

J. Larry Lyon, Ph.D., Dean

Page bearing signatures is kept on file in the Graduate School.

TABLE OF CONTENTS

LIST OF FIGURES

LIST OF TABLES

NOMENCLATURE

A_c	Accumulation parameter
A_t	Total area of heated section
b_n	Winning codebook vector
C_f	Skin friction coefficient
C_k	Conduction parameter for the k^{th} heated section (0.9, 0.9, 1.05, 1.1, 1.05)
c_p	Specific heat of fluid
C_p	Pressure coefficient
E	Voltage across heater
h	Convective heat transfer coefficient
I	Current through heater
J	Number of points on a surface for which b_n is the closest vector
K	Droplet inertial parameter
K_0	Modified inertial parameter
k_f	Thermal conductivity of fluid
k_p	Thermal conductivity of Plexiglas
L	Length scale of Stokes number
$m_w^{'}$	Mass flux
n	Freezing fraction
N	Sample size
$N_{f,stag}$	Freezing fraction
$\overline{N}_{0,R}$	Stagnation point fully-dense rime ice stagnation thickness

N_x^j	Orthogonal distance from an ice surface point to the mean ice shape
p	Pressure
Pr	Prandtl number
$\dot{Q}_{CONV}$	Convected heat
$\dot{Q}_{GEN}$	Energy supplied
$\dot{Q}_{HL}$	Heat loss
$\dot{Q}_{RAD}$	Radiated heat
q''_w	Wall heat flux
Re	Reynolds number
Re_δ	Droplet Reynolds number
R_q	Root-mean-square roughness height (also called RMS)
r_0	Leading edge radius
S	Standard deviation
St	Stanton number
Sk	Stokes Number
T_{BL}	Thermal boundary layer temperature
T_{FSi}	Average freestream temperature over i^{th} surface panel
T_{IR}	Infrared camera temperature reading
T_S	Surface temperature
T_{SS}	Steady state temperature
T_{total}	Total temperature
T_{UP}	Temperature under plate
T_∞	Freestream temperature

t_p	Plexiglas sub-plate thickness
t	Student's t-value
u	Streamwise velocity
U_e	Edge velocity
U_{random}	Random uncertainty
U_∞	Freestream velocity
V	IRT tunnel velocity
V_{eff}	Effective velocity measured by hot-film wire(s)
V_{meas}	Measured velocity by pitot-static probe
V_N	Normal velocity component
V_T	Tangential velocity component
x	Streamwise location on plate
x_{cr}	Critical distance for flow transition
x_k	Sand grain equivalent roughness height
w	Wall-normal velocity
z	Wall-normal distance from plate surface

Greek

α	Thermal diffusivity OR angle of x-array probe
β_0	Stagnation point collection efficiency
β_s	Local cloud collection efficiency
γ_s	Angle of surface relative to airfoil design flow coordinates
δ	Velocity boundary layer thickness

δ_T	Thermal boundary layer thickness
Δt_s	Exposure time
ε	Emissivity (0.95)
ζ	Dummy variable representing x in Stanton number correlations
κ	Tangential velocity attenuation factor (0.115)
μ	Fluid dynamic viscosity
μ_{air}	Dynamic viscosity of air
v	Fluid kinematic viscosity
ξ	Unheated starting length (1.7285")
ρ	Fluid density
ρ_{ice}	Ice density at freestream temperature
ρ_w	Droplet density
σ	Stefan-Boltzmann constant (5.67E-8 W/m^2K^4)
τ_w	Wall shear stress

Subscripts

TC, cal	Thermocouple temperature measurement during calibration
TC, test	Thermocouple temperature measurement during test
IR, cal	Infrared temperature measurement during calibration

Abbreviations

ARES	Airfoil Roughness Evaluation System
BUSWT	Baylor University Subsonic Wind Tunnel
FAA	Federal Aviation Administration

IRT	Icing Research Tunnel
LEWICE	Lewis Ice Accretion Code
LWC	Liquid water content
MVD	Median volumetric Diameter
NACA	National Advisory Committee of Aeronautics
NASA	National Aeronautics and Space Administration
RMH	Roughness maximum height
RMS	Root-mean-square roughness height
SLD	Supercooled large droplets
SOM	Self-organizing map
VIST	Vertical Icing Studies Tunnel

ACKNOWLEDGMENTS

I owe much thanks to Dr. Stephen McClain for his support and guidance as my advisor. Thank you for allowing me to work in your research group and for your time spent assisting throughout this project. I would also like to thank Dr. Jill Klentzman and Dr. Randall Jean for serving on my thesis committee. Your assistance is greatly appreciated.

I would also like to thank my predecessors on this project, Logan Tecson, Chris Walker, Tim Shannon, Michael Hughes, and Matt Hawkins, for laying the ground work that allowed me to continue expanding on this research grant. Many thanks are extended to Mr. Ashley Orr for the long hours spent machining complex surface roughness panels. I would also like to thank my fellow grad students John-Mark Clemenson, Zac Williams, Nic Mosser, and Berkley Bonjonia for your assistance with both this project.

Many thanks also extend to my parents for their continuous love and encouragement, my sister for never hesitating to snap me back to reality, and my fiancé Michael for his support of everything I do.

Finally, I would like to thank the icing branch at NASA Glenn Research Center for allowing me to work with you over the summer and the NASA Collaborative Agreement No. NNX16AN32A which funded this research.

DEDICATION

To my family and my fiancé, Michael

CHAPTER ONE

Introduction

Motivation

Since the beginning of powered flight, in-flight icing has proven detrimental to the safety of an aircraft. Ice accreted on aircraft wings causes a reduction in lift and stall margin along with an increase in drag and aircraft weight [1]. With these alterations to the flight safety and performance of the aircraft, accidents are more likely to occur. Avoiding flight through these icing conditions is ideal, but not always practical. As air traffic continues to grow, evading icing conditions is becoming nearly impossible. For this reason, designing aircrafts that can safely and successfully operate in common icing conditions has become crucial.

Some design alterations intended to achieve this goal include anti-icing methods, while others incorporate de-icing methods. Anti-icing methods aim to prevent ice formation during operation, and can involve the use of electric heaters or routing relatively warmer air through the wing to heat the surface. De-icing methods attempt to remove ice that has already formed on a wing using methods like pneumatic boots or glycol spray [2]. The method classification is commonly designated by its time of use, if ice has yet to form on the wing it is classified as an anti-icing method; if ice is already present the method is classified as de-icing. Some of these methods may remove only part of the ice, while others require extra power to be routed away from the engine. Both

anti-icing and de-icing design variations often require a sacrifice in efficiency from the aircraft.

With flight safety in mind, the Federal Aviation Administration (FAA) began requiring that an aircraft be designed to safely navigate with a certain amount of in-flight icing. Until 2014 the FAA specifications required aircrafts to be capable of operation in Appendix C icing conditions which are defined in Appendix C of the U.S. Code of Federal Regulations [3]. Then in 2014 the specifications were updated to instead require safe operation in Appendix O icing conditions [4].

With these FAA requirements in place, the need arose for the ability to predict aircraft icing to test new designs and ensure efficiency. The costly nature of full scale experimental testing makes the use of a simulation code very appealing. The proposed code would be used to simulate ice accretion development on the new designs as a more cost effective preliminary testing option.

Various ice simulation codes have been developed; one of specific importance to this paper is the Lewis Ice Accretion Code, also known as LEWICE, which is used for the design of de-icing systems. LEWICE was developed by the engineers at NASA Glenn Research Center for the purpose of mass distribution to aircraft manufacturers, and is the leading code of its type. The LEWICE prediction model is widely used, but has room for improvement in its prediction capabilities. One such improvement is in its ability to predict the convective heat transfer changes due to the ice roughness formation on the airfoil surface [5]. The LEWICE convection prediction methods are based on a sand grain roughness model which has regular, ordered elements of a specified geometry and experiences a constant freestream flow. The LEWICE code uses a constant roughness

height that does not change in time in its model. In reality, the freestream flow over an airfoil is not constant and roughness elements on a real ice surface are placed in a stochastic pattern with varying heights and the roughness evolves in time. The simplistic models used by LEWICE are thought to be the cause of its prediction discrepancies [6].

The formation of large ice protrusions depends heavily on the layer of ice roughness that is formed within the first few minutes of an icing event [5]. If LEWICE does not accurately predict this roughness layer, the predictions for the larger protrusions which form after longer accretion times will also be inaccurate. Figure 1.1 shows an example of a LEWICE profile prediction compared to the experimental results of a profile formed in the Icing Research Tunnel (IRT) at NASA Glenn. LEWICE has had marginal success because of its ability to predict separation points in the flow due to ice shapes, but its convective heat transfer prediction model makes little physical sense. To improve this model, the physics of ice accretion must be better understood.

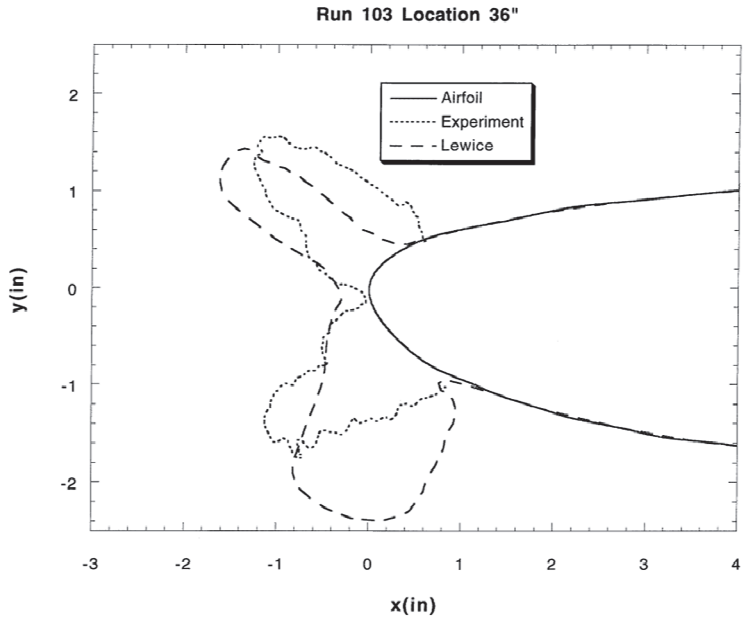

Figure 1.1: Comparison of LEWICE Prediction to Experimental Accretion Ice Shape Formed in the NASA Glenn Icing Research Tunnel [7]

Many studies have been performed to improve the LEWICE heat transfer characterization capabilities. Each of these studies focuses on an individual aspect of the iced profiles. Earlier studies done by Tecson [8], Walker [9], Shannon [10], and Hughes [11] focused on realistic ice roughness profiles made of simplified geometries and distributions, while Hawkins [12] introduced a real ice roughness profile. The study done by Tecson [8] investigated the convective heat transfer enhancement on realistic ice roughness distributions experiencing negligible flow acceleration. Following that, Walker [9] studied the effect of varying boundary conditions on the convection of realistic ice roughness. The surfaces studied by Tecson [8] and Walker [9] involved an abrupt smooth to rough transition which is unrealistic according to laser scans of real ice surfaces. Shannon [10] addressed this issue by comparing the convective heat transfer of the historical realistic ice surfaces to a surface involving a more gradual smooth to rough transition with fixed thermal boundary conditions. Hughes [11] then studied the effect of realistic ice roughness in the stagnation region (the leading 2%) on the heat transfer of an iced profile. This was done in the Vertical Icing Studies Tunnel (VIST) at NASA Glenn Research Center to accurately model the stagnation region of the airfoil. Most recently Hawkins [12] used the setup of Tecson [8], Walker [9], and Shannon [10] to compare convective heat transfer results from a real ice roughness surface to those of a realistic ice roughness surface created by Shannon [10]. This real ice surface was fabricated from a laser scanned ice roughness profile created in the IRT.

Objective

The purpose of this investigation is to expand on the work of Tecson [8], Walker [9], Shannon [10], Hughes [11], and Hawkins [12] by collecting both heat transfer and

velocity data for multiple real ice roughness profiles representing different times in the early ice accretion process. Three real ice roughness surfaces were fabricated to replicate the laser scans of ice roughness taken during testing in the IRT. These three laser scanned surfaces combined with that used to create the real ice surface created by Hawkins [12] were formed with different exposure times to the same icing conditions. Together they provide a progression of roughness development with respect to increasing exposure time. For each of the surfaces convective heat transfer and velocity boundary layer profiles were measured as the surfaces experienced both accelerating flow like that found on an airfoil and flow with negligible acceleration caused by wind tunnel friction.

This investigation aims to improve the heat transfer characterization of LEWICE by providing experimental convection measurements for real ice roughness formation with differing amounts of exposure to an accretion event. These measurements will ultimately be used to create a correlation for the prediction of convection in the presence of ice roughness.

Order of Presentation

Chapter Two provides a summarized technical background of heat transfer, fluid mechanics, airfoils, surface roughness, and historical ice accretion studies. Chapter Three discusses the methodology and materials used to perform the experimentation in this study. Chapter Four provides the experimental results and a discussion of their significance. Chapter Five presents the conclusions made from the results, recommendations for improvement, and future work.

CHAPTER TWO

Technical Background

A certain amount of background is necessary to demonstrate the relevance, details, and purpose of this study. This chapter will outline the basic concepts of aircraft icing, as well as viscous and thermal boundary layers, and fluid flow over an airfoil. Additionally, the historical ice accretion studies and ice accretion modeling will be described along with a background on surface roughness measurement techniques.

Aircraft Icing

Basic Concepts

The term ice accretion describes the collection of ice on a surface over a period of time. In this study, the surface of interest is an airfoil. Two quantities used to define ice accretion conditions are liquid water content (LWC) and median volumetric diameter (MVD). LWC is the amount of liquid water per unit volume of air, a high LWC means either a high quantity of droplets are present or the droplets are very large. The MVD is the droplet diameter that represents the center of the droplet diameter range within the LWC. If all the droplets in the air were ordered in terms of size, half of the droplet diameters would be larger than the MVD while the other half would be smaller [13]. The LWC affects the speed of the ice accumulation while the MVD affects its extent. The MVD is the controlling parameter in both quantifying icing conditions and designating the conditions in which an aircraft must be able to safely operate.

Appendix C conditions were of utmost concern to the aircraft industry until the safety guidelines and requirements for aircraft operation in icing conditions were changed in 2014. Because of this, most historical ice accretion studies were performed using these conditions. Appendix C conditions consist of supercooled or partially frozen droplets with an MVD of 1-50 μm, and are commonly referred to as "freezing drizzle" [3]. The conditions of interest for this study and the current aircraft safety requirements are designated as Appendix O icing conditions. Appendix O icing conditions are commonly called "freezing rain" and include partially frozen or supercooled droplets with an MVD > 50 μm, commonly referred to as supercooled large droplets (SLD) [4].

As ice accretions form they can be classified into two regimes: glaze ice and rime ice. Glaze ice is characterized by a layer of liquid water runback caused when impinging droplets do not freeze immediately. The runback layer continues to flow along the airfoil until freezing occurs resulting in clear, dense ice shapes. Since glaze ice usually forms close to the freezing temperature of water, there is less heat transfer and its formation process is relatively slow. Rime ice, on the other hand, occurs well below the freezing point of water and is the result of every droplet freezing upon contact with the aircraft surface. Rime ice forms a much rougher ice shape that is brittle due to air trapped between the droplets. This trapped air causes its cloudy, opaque appearance.

The accumulation parameter is a non-dimensional representation of the mass flux equation which is presented in Eq. (2.1)

$$m_w^{'} = LWC \cdot V \cdot \beta \cdot \Delta t_s \tag{2.1}$$

where V is the freestream velocity, Δt_s is the exposure time, and β is the cloud collection efficiency which will be discussed in the following paragraph [14]. The accumulation

parameter represents the length of ice growth, in terms of the airfoil leading edge radius, that would theoretically form on a flat plate placed perpendicular to the freestream flow for the designated exposure time [15]. In ice accretion studies this parameter is used to characterize the roughness accumulation on a surface. The definition of the accumulation parameter is presented in Eq. (2.2)

$$A_c = \frac{LWC \cdot V \cdot \Delta t_s}{2 \cdot r_0 \cdot \rho_{ice}} \tag{2.2}$$

where r_0 is the leading-edge radius of curvature of the airfoil, a NACA 0012 in this case, and ρ_{ice} is the density of ice at the freestream temperature. The importance of accumulation parameter arises from its ability to account for exposure time [15]. The accumulation parameter is proportional to the rate at which water impinges the surface and the icing time and is a normalized thickness representation of the ice shape on the airfoil surface [16]. A high accumulation parameter indicates a high accretion rate.

Not all droplets in the flow impinge with the surface; some of the smaller droplets follow the path of the flow around the airfoil. The amount of droplets impinging depends on the MVD of the droplet distribution. A collection efficiency term was originally derived by Ruff [14], and is used to account for the fraction of the total droplets that impinge the surface. This derivation uses a droplet inertial parameter, *K*, which was established by Tsao and Lee [17] and Tsao and Kreeger [18] by applying a different length scale to the Stokes number equation. The equations for the Stokes number, *Sk*, and the inertial parameter are presented in Eq (2.3) and (2.4), respectively.

$$Sk = \frac{\rho_w \cdot V \cdot MVD^2}{18 \cdot \mu_{air} \cdot L} \tag{2.3}$$

$$K = \frac{\rho_w \cdot V \cdot MVD^2}{18 \cdot \mu_{air} \cdot r_0} \tag{2.4}$$

The stagnation point collection efficiency of Langmuir and Blodgett [19], β_0, can be calculated using Eq. (2.5)

$$\beta_0 = \frac{1.4\left(K_0 - \frac{1}{8}\right)}{1+1.4\left(K_0 - \frac{1}{8}\right)} \tag{2.5}$$

where K_0, is a modified version of K known as the modified inertial parameter of Langmuir and Blodgett [19] and defined in Eq. (2.6).

$$K_0 = \frac{1}{8} + \frac{\lambda}{\lambda_{Sk}}\left(K - \frac{1}{8}\right) \tag{2.6}$$

In Eq. (2.6) $\frac{\lambda}{\lambda_{Sk}}$ is the droplet range parameter which is a function of droplet Reynolds number, Re_δ. The droplet Reynolds number and the droplet range parameter are defined in Eq. (2.7) and (2.8), respectively.

$$Re_\delta = \frac{\rho V MVD}{\mu} \tag{2.7}$$

$$\frac{\lambda}{\lambda_{Sk}} = \frac{1}{0.8388+0.001483Re_\delta+0.01847\sqrt{Re_\delta}} \tag{2.8}$$

Once the stagnation collection efficiency is known, the local cloud collection efficiency, β_s, at different locations along an airfoil can be calculated from the stagnation point collection efficiency using Eq. (2.9).

$$\beta_s = \beta_0 cos(\gamma_s + \alpha) \tag{2.9}$$

The local cloud collection efficiency includes an angular term to account for both the angle of attack, α, and the angle of the surface relative to the airfoil design flow coordinates, γ_s [20]. Higher collection efficiency is the result of a higher cloud MVD and represents a higher percentage of the cloud droplets impinging the surface.

Eq. (2.10) can be used to calculate the stagnation point leading-edge, fully dense, theoretical rime ice thickness, $\overline{N}_{0,R}$. According to this equation, higher cloud collection efficiency will also result in a greater theoretical rime ice stagnation thickness.

$$\overline{N}_{0,R} = 2r_0 A_c \beta_0 \tag{2.10}$$

This parameter combines the accumulation parameter and the cloud collection efficiency, and is used in scaling roughness and thickness geometry based on an assumed freezing fraction of 100% to quantify the stagnation point thickness differences seen in glaze-ice conditions. The stagnation point fully dense rime ice thickness allows the temporal roughness development to be scaled in terms of a relative maximum roughness height of the ice profiles.

The greatest difference between glaze ice and theoretical rime ice stems from their convective heat transfer capabilities. When droplets impinge the surface of an airfoil in rime ice conditions, the latent heat of fusion is convected away quickly as a result of the low temperature environment. The higher temperature experienced during glaze ice formation results in insufficient heat transfer to remove all of this latent heat [21]. Lower heat transfer means that not all droplets freeze upon impingement with the airfoil. This difference in convective heat transfer due to temperature causes the glaze ice liquid layer runback.

Glaze ice liquid layer runback is a layer of liquid water that is present on the surface of glaze ice shapes. The layer is the result of unfrozen supercooled droplet accumulation in the stagnation region of the airfoil and has an extremely high thermal conductivity. When the droplets accumulate and reach a size where the drag forces acting on them are able to overcome their surface tension forces, the droplets begin traveling

toward the trailing edge of the airfoil. This travel leaves behind a thin liquid layer, known as a trailing tail, where new droplets begin to form and accumulate [22]. The droplets will begin to freeze as they travel along the airfoil; the location of this freezing is the beginning of the smooth-to-rough transition and the end of the ice plateau region.

The ice plateau region is an area of smooth thick ice formed from the liquid layer of droplets traveling downstream from the stagnation point. This region occurs in the laminar flow regime where the heat transfer is low, resulting in a uniform water film coating the surface. The water film breaks down as the droplets begin to freeze and form ice roughness. The film breakdown location is also known as the smooth-to-rough transition region, where the ice accretion transitions to begin forming roughness elements. The film breakdown occurs when the boundary layer begins its transition from laminar to turbulent flow [20]. Once film breakdown occurs, the roughness elements collect later droplets traveling downstream increasing the size and height of the roughness elements. The smooth-to-rough transition region generally migrates toward the stagnation point with increasing exposure time [21]. Hence, increasing the accumulation parameter is expected to result in an earlier smooth-to-rough transition.

Heat Transfer and Fluid Mechanics Background

Boundary Layers

The two boundary layers of interest in this study are the velocity (also known as viscous) boundary layer and the thermal boundary layer. Both types form due to interactions between the properties of an object and the fluid flowing over it. Velocity and thermal boundary layers will be further described in the subsections to follow.

Velocity boundary layers. In 1904 Ludwig Prandtl revolutionized fluid dynamics with the idea that a fluid experiences frictional effects only very close to the surface of an object moving through it. Prandtl called this region close to the surface a boundary layer [23]. The velocity boundary layer is a thin region, relative to the size of the body or flat plate, on the surface of a body where viscous effects are important. Outside of the boundary layer the fluid behaves as if it were inviscid. As the fluid flow progresses along a body, the boundary layer grows in height because of the no slip condition which was also established by Prandtl. The no slip condition states that the friction between a fluid and the surface of a body is so great that the velocities between the surface and the fluid must be equal. Further from the surface, the frictional forces are overcome by the inertial forces of the fluid forming a developing boundary layer that varies as a function of distance from the body, vertical distance in the case of a flat plate [24].

Figure 2.1 depicts the viscous boundary layer development as a fluid flows over a flat plate. In its early formation the boundary layer is classified in the fully laminar flow regime. Once the flow reaches a critical distance from the leading edge (x_{cr}), it enters the transitional flow regime followed by the turbulent regime. Even after transitioning to turbulent flow the region of the boundary layer closest to the wall remains viscous and behaves as it would in laminar flow, as seen in Figure 2.1. This region, defined as the viscous sublayer, affects the shape of the boundary layer profile and causes larger velocity gradients at the wall than those formed in the laminar flow regime. For any location along the plate, the velocity in a boundary layer (u) is assumed to vary as a function of vertical distance from the surface ($u(z)$). The viscous boundary layer

thickness (δ) is generally assumed to end where *u(z)* is approximately 99% of the freestream flow velocity (U_∞).

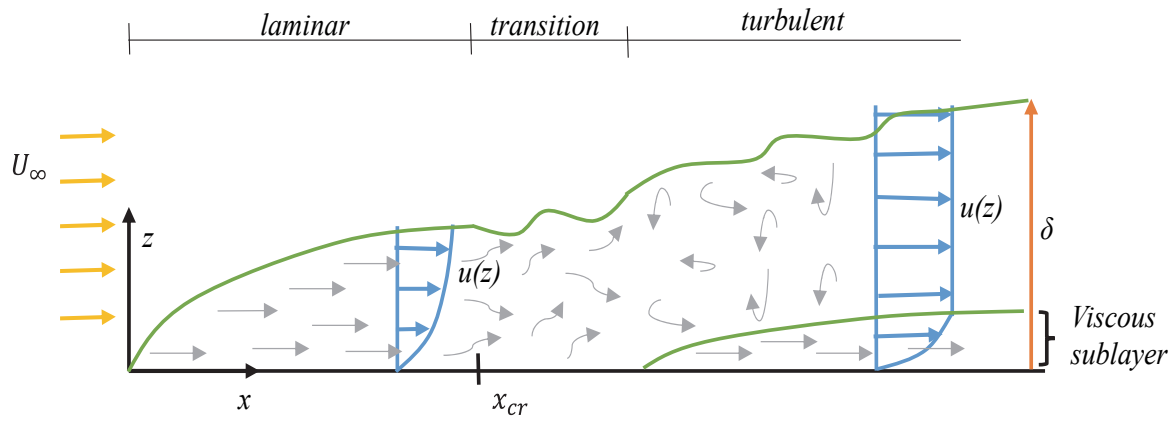

Figure 2.1: Viscous Boundary Layer Development over a Flat Plate

The Reynolds number is an important parameter in velocity boundary layer analysis. The Reynolds number (*Re*) is non-dimensional and is used to characterize and compare flow patterns of different fluids. The local Reynolds number for flow over a flat plate is defined in Eq. (2.11)

$$Re = \frac{\rho U_\infty x}{\mu} \tag{2.11}$$

where μ is the dynamic viscosity of the fluid, ρ is the fluid density, x is the distance from the leading edge of the flat plate, and U_∞ is the freestream fluid velocity. For a flat plate, larger Reynolds numbers result in smaller regions where viscous effects are influential, hence smaller boundary layers. For flow over a flat plate in typical conditions a Reynolds number of 5 x 10^5 or greater is considered turbulent flow, while flow with a smaller Reynolds number is considered laminar [24].

A wall shear stress occurs on the surface of a flat plate as a result of the fluid motion and the no slip condition. The wall shear stress definition for a Newtonian fluid is given by Eq. (2.12).

$$\tau_w = \mu \left.\frac{\partial u}{\partial z}\right|_{z=0} \tag{2.12}$$

The wall shear stress can be converted to a non-dimensional form called the skin friction coefficient, which is defined in Eq. (2.13).

$$C_f = \frac{\tau_w}{\frac{1}{2}\rho U_\infty^2} \tag{2.13}$$

This non-dimensional coefficient allows for comparison of wall shear stress values between different surfaces experiencing similar flow conditions [24].

Thermal boundary layers. The concept of a thermal boundary layer is similar to that of a velocity boundary layer. If a temperature difference exists between the surface of a body and the fluid in contact, a thermal boundary layer will form. Similar to the no-slip condition, the fluid in contact with the surface will have the same temperature as the surface (T_S). As the distance from the body increases (the vertical distance in the case of a flat plate), the temperature changes until the difference between the boundary layer temperature and the surface temperature (T_{BL}- T_S) is approximately 99% of the temperature difference between the surface and the freestream (T_S - T_∞). At this point the thermal boundary layer height (δ_T) has been reached. The thermal boundary layer height increases as the flow progresses downstream from the leading edge of a flat plate (x), and the boundary layer temperature at any location along a flat plate varies only in the vertical direction ($T_{BL(z)}$) [25]. Figure 2.2 depicts the development of a thermal boundary layer when the surface temperature is greater than the freestream temperature, $T_\infty < T_S$.

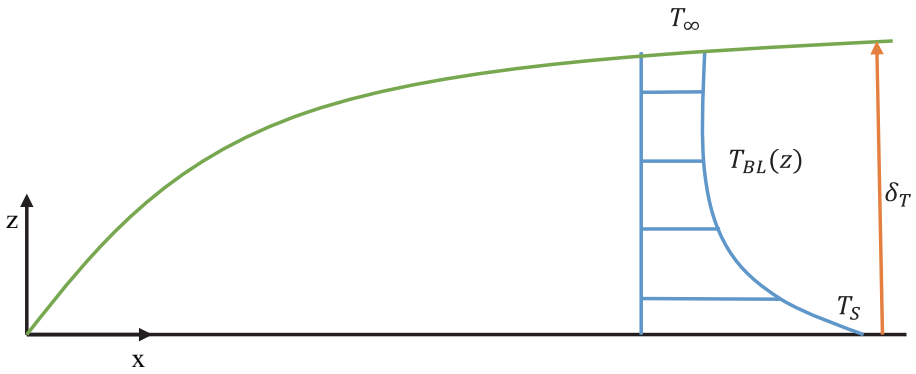

Figure 2.2: Thermal Boundary Layer on a Flat Plate, $T_\infty < T_S$

The Prandtl number is a non-dimensional parameter used to relate thermal and velocity boundary layers. This parameter can be considered a geometric scaling factor relating the sizes of the viscous and thermal boundary layers by comparing the thermal and viscous diffusivity rates. The definition of the Prandtl number is given in Eq. (2.14)

$$Pr = \frac{c_p \mu}{k_f} = \frac{v}{\alpha} \tag{2.14}$$

where c_p is the fluid specific heat, k_f is the thermal conductivity of the fluid, v is the fluid kinematic viscosity, and α is the thermal diffusivity of the fluid. For an isothermal plate, a Prandtl number less than one implies a thicker thermal boundary layer, while a Prandtl number greater than one implies a thicker velocity boundary layer [25].

The presence of a thermal boundary layer causes a heat flux between the surface of the flat plate and the fluid. This heat flux is defined in Eq. (2.15).

$$q''_w = k_f \frac{\partial T}{\partial z}\bigg|_{z=0} \tag{2.15}$$

The heat flux can be represented using a non-dimensional parameter called the Stanton number. Stanton numbers can be calculated using either heat fluxes or the convective heat transfer coefficients, which were calculated in this study. This parameter is useful when comparing different test data because it accounts for differences in ambient

environment, fluids, and flow fields between tests. This study used the local Stanton numbers for comparison between tests performed on different dates. The definition of the local Stanton number can be seen in Eq. (2.16)

$$St_x = \frac{q''_w}{\rho U_\infty c_p (T_S - T_\infty)} = \frac{h}{\rho U_\infty c_p} \tag{2.16}$$

where h is the convective heat transfer coefficient. For a boundary layer, Reynolds analogy relates the local non-dimensional parameters of velocity ($C_{f,x}$) and thermal boundary (St_x) layers. The analogy is presented in Eq. (2.17).

$$\frac{C_{f,x}}{2} = St_x \tag{2.17}$$

Reynolds analogy quantifies boundary layers, allowing the calculation of other flow parameters [26]. It should be noted that this analogy is only valid for smooth flat plates, which only includes the leading edge region of the surfaces tested in this study.

Theoretical Stanton number correlations for laminar and turbulent flow over a flat plate were used in this study for result comparison. For the negligible flow acceleration cases, the laminar and turbulent flow correlations are given in Eq. (2.18) and Eq. (2.19), respectively. These correlations assume constant heat flux and unheated starting length (ξ) boundary conditions.

$$St_{x,\ lam,\ no\ xcel} = \left[1-(\xi/x)^{3/4}\right]^{-1/3} 0.453 Re_x^{-1/2} Pr^{-2/3} \tag{2.18}$$

$$St_{x,turb,no\ xcel} = \left[1-(\xi/x)^{9/10}\right]^{-1/9} 0.0308 Re_x^{-1/5} Pr^{-2/3} \tag{2.19}$$

New correlations were developed to account for the flow acceleration over the plate. Equations (2.18) and (2.19) were used as the basis for these new correlations, with the same boundary condition assumptions. The theoretical laminar correlation for accelerating flow over a flat plate was developed by applying the correction method of

Smith and Spaulding [27] to Eq. (2.18), while the theoretical turbulent correlation was found by applying the correction methods of Ambrok [28] to Eq. (2.19). The new correlations for laminar and turbulent accelerating flow over a flat plate are shown in Eq. (2.20) and Eq. (2.21), respectively. See Shannon [10] for more information about the derivation of these correlations.

$$St_{x,\ lam,\ xcel} = \left[1-(\xi/x)^{3/4}\right]^{-1/3} \frac{0.453 Re_x^{-1/2} Pr^{-2/3}}{\left[\int_0^{\zeta}\left(\frac{U_e(\zeta)}{U_e(x)}\right)^{(2.95Pr^{0.07})-1}\frac{d\zeta}{x}\right]^{1/2}} \tag{2.20}$$

$$St_{x,\ turb,\ xcel} = \left[1-(\xi/x)^{9/10}\right]^{-1/9} \frac{0.0308 Re_x^{-1/5} Pr^{-2/3}}{\left[\int_0^{\zeta}\left(\frac{U_e(\zeta)}{U_e(x)}\right)\frac{d\zeta}{x}\right]^{1/5}} \tag{2.21}$$

In these equations ζ is a dummy variable used to represent the location where the velocity is found, and U_e is the edge velocity at the same location.

Airfoils

Airfoils are designed to induce flow acceleration, usually along the top surface. Flow velocity and pressure along the surface of an airfoil are inversely related, so as the flow accelerates, velocity increases and pressure decreases. This is due to Bernoulli's equation, which is defined in Eq. (2.22)

$$p + \frac{1}{2}\rho U_\infty{}^2 = \text{constant} \tag{2.22}$$

where p is the pressure over the surface and the elevation term is considered negligible for this application. The distribution of pressure, or pressure gradient, along the surface is not constant and changes in response to velocity changes. As the fluid flows over the airfoil surface a certain pressure gradient forms. The accelerating flow causes the pressure gradient to drop and form a favorable pressure gradient until a minimum

pressure is reached. After reaching this minimum, the pressure gradient begins to rise again, causing an adverse pressure gradient. Typical pressure gradients along an airfoil surface are evident in Figure 2.3. As shown in the figure, the top surface, or suction surface, has a pressure less than zero while the bottom surface, or pressure surface, shows the opposite trend.

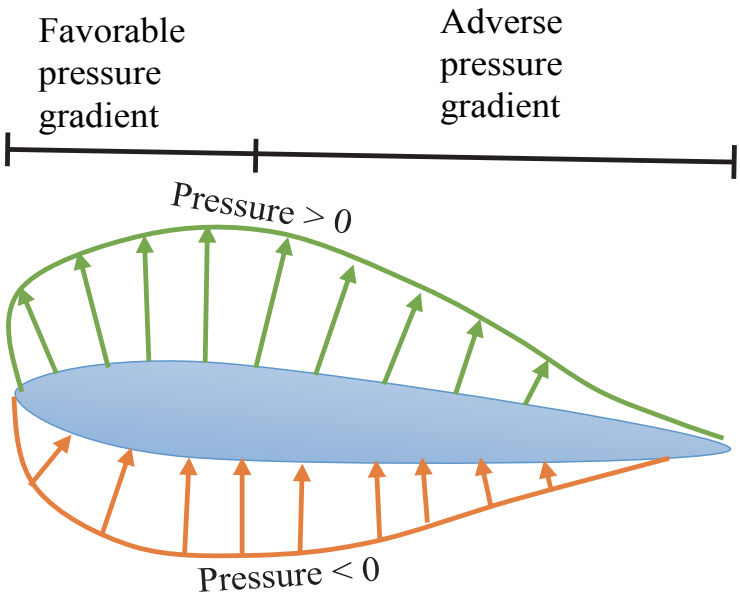

Figure 2.3: Pressure Distribution on an Airfoil Surface

As the flow continues the adverse pressure gradient increases until reaching a separation point. A separation point occurs when the adverse pressure gradient causes enough of a fluid momentum deficit that the fluid cannot overcome the friction between itself and the surface, resulting in zero fluid velocity. The fluid and boundary layer then detach from the wall creating a region of flow reversal called a wake region [24]. Figure 2.4 depicts the velocity boundary layer development as a fluid accelerates over an airfoil surface and experiences separation. The flow reversal and wake region formation are also evident in this Figure 2.4.

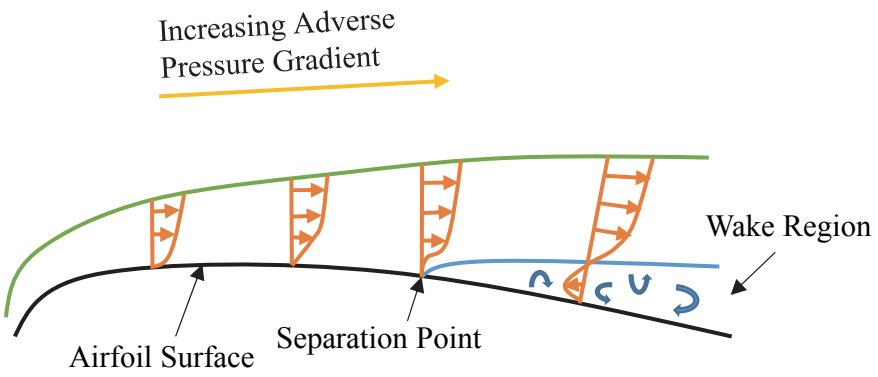

Figure 2.4: Flow Separation Diagram

The instrumentation needed to measure the fluid flow properties and heat transfer on a surface would be costly and complex to implement on a realistic airfoil. For these experiments it is useful to geometrically flatten the airfoil surface and perform representative tests on a flat plate surface experiencing the same flow acceleration. Flat plate representations allow for less complex boundary conditions and assumptions to be applied to current models, as well as the use of interchangeable surface features. While it is possible to perform heat transfer and velocity testing on an instrumented airfoil surface, the use of a flat plate representation is more conducive to this study.

Ice Accretion Modeling

Messinger [29] developed the foundational model for aircraft icing in 1953. Messinger's model executes an energy balance on an unheated airfoil in icing conditions. The energy input for this model resulted from the combination of the kinetic energy of impinging water droplets, frictional heating in the boundary layer, and the latent heat of fusion. Convection, sublimation/evaporation, and energy absorption by impinging supercooled droplets were combined to form the energy losses in the model [29]. While

there are many modes of energy transfer, both losses and gains, to consider for an airfoil in icing conditions, convection is the most influential to the heat transfer of the airfoil. A correct convection measurement greatly improves the accuracy of ice shape formation and growth rate predictions [30]. The modes of energy transfer experienced by an unheated airfoil in icing conditions in Messinger's model are shown in Figure 2.5.

Messinger [29] also introduced the concept of a freezing fraction, because every supercooled droplet does not fully freeze upon impingement. The freezing fraction is a non-dimensional representation of the portion of droplets that freeze upon impact as compared to the total number of droplets present in the flow. A freezing fraction of one represents a rime ice shape, while anything less than one is considered glaze ice. Accounting for the unfrozen liquid in the impingement region helps to quantify and explain variations in the ice formation.

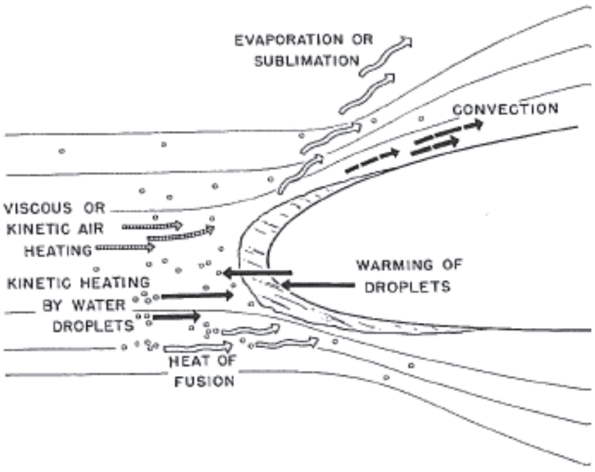

Figure 2.5: Modes of Energy Transfer for an Unheated Airfoil in Icing Conditions [29]

Versions of the Messinger model are still in use today. One such version is used in NASA's Lewis Ice Accretion Code, also known as LEWICE. The LEWICE code uses modified versions of Messinger's freezing fraction and energy balance concepts along

with a sand grain equivalent roughness model from Nikuradse [31] and Schlicting [32] to estimate ice roughness formation and growth rate at each point along an airfoil surface [33]. The sand-grain roughness height equation used by LEWICE is seen in Eq. (2.23)

$$x_k = \frac{1}{2}\sqrt{0.15+\frac{0.3}{N_{f,stag}}} \tag{2.23}$$

where $N_{f,stag}$ represents the freezing fraction and x_k is the dimensionless surface roughness height, or equivalent sand grain roughness height. An integral boundary layer method is then used to calculate the heat transfer coefficients and characterize the convective heat loss from the surface. LEWICE also has the ability to model both the mass flux on the surface for the runback water layer and the skin friction coefficient development along the roughening surface [33].

The roughness modeling of LEWICE has been questioned as a study done by Shin [6] observed that the sand grain roughness model does not produce similar results to those found experimentally using the IRT. Because the roughness model used in LEWICE depends only on Messinger's freezing fraction, Shin also found that the code prediction did not change when parameters other than the freezing fraction were altered. In this particular study, Shin found that when varying the temperature, LWC, and airspeed of the icing conditions, the LEWICE results did not match those found experimentally in terms of trend or magnitude in most cases. An example of the differing results can be seen in Figure 2.6. The LEWICE roughness models are suspected of being too simplistic for accurate convective heat transfer modeling [6]. Bons [34] and Bons and McClain [35] found that the modeling of the roughness elements in ordered and repeatable geometric patterns, as is done in the sand grain roughness model, produced results not similar to those seen in experimental testing of realistic ice roughness.

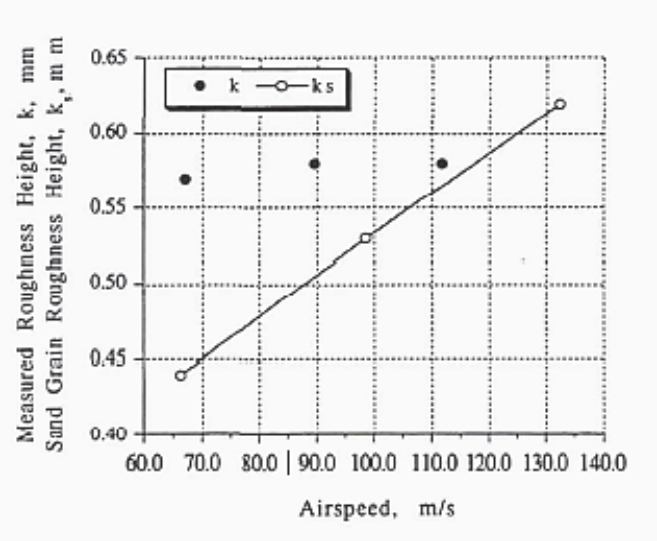

Figure 2.6: Comparison of Measured Roughness Height to Sand Grain Roughness Height Predictions [6]

Vargas [36] observed that for ice accretions that fall into the pure rime ice regime, LEWICE is able to accurately predict the roughness and growth rate because all of the droplets freeze immediately upon impact. When the air temperature is not low enough, and glaze ice forms, the LEWICE prediction methods become less effective. The models used by LEWICE experience prediction issues when liquid water runback is present. These prediction issues are suspected to be due to the multiphase icing that occurs on the surface in glaze ice conditions.

Historical Ice Accretion Studies

The effect of ice roughness on the convective heat transfer of an airfoil has been thoroughly investigated to characterize its development and improve the initial models. Poinsatte et al. [30] studied ice roughness created both in flight and in the IRT in an effort to characterize the effect of convective heat transfer on an airfoil. The investigation involved the addition of uniform hemispherical roughness elements in four different ordered patterns to a smooth NACA 0012 airfoil surface. These patterns are presented in

Figure 2.7. The study found good agreement between the measurements taken in the two environments. It also found that the addition of roughness elements to an airfoil greatly increased the heat transfer downstream of the stagnation region. Poinsatte et al. observed that when the density of the roughness was increased, for example Figure 2.7 (b) roughness density increasing to that of 2.7 (d), the heat transfer increased yet again. Roughness at the leading edge as seen in Figure 2.7 (a) forced the flow to transition into turbulence earlier than with the smooth surface, resulting in a slight increase in heat transfer.

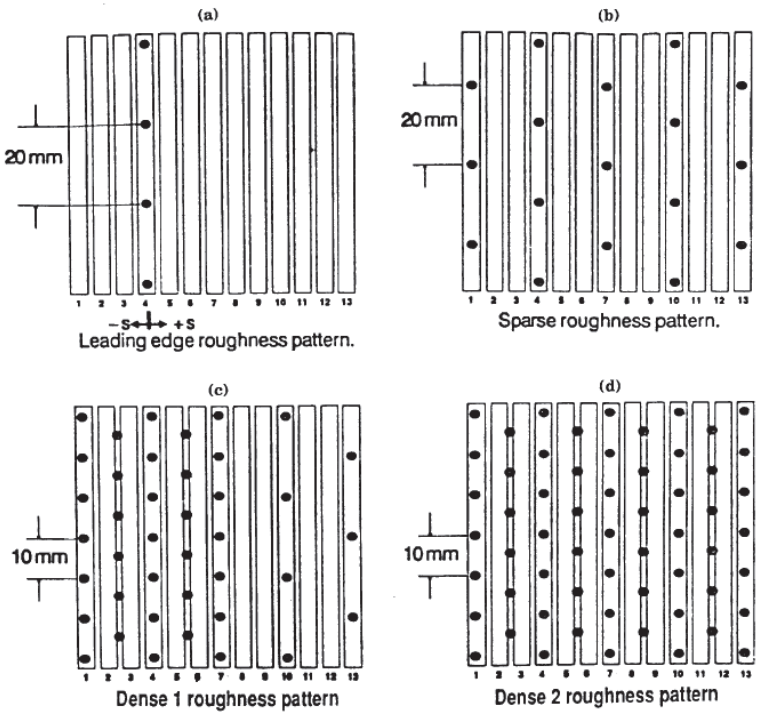

Figure 2.7: Ordered Roughness Distributions studied by Poinsatte et al. [30]

Bragg et al. [37] studied the effect of roughness on the velocity boundary layer. Using ordered hemispherical roughness elements on a NACA 0012 airfoil and fluorescing oil particles in the air flow of a wind tunnel, turbulence intensity profiles were recorded at different locations along the chord of the airfoil. Roughness elements

were found to cause earlier transition into turbulent flow along the airfoil. Bragg et al. [38] further expanded on these results by considering the effect of this transition on the heat transfer at the smooth-to-rough boundary transition. This study used hot-wire anemometry to vary the freestream turbulence intensity over a surface consisting of ordered hemispherical elements. The study concluded that the varying turbulence intensity did little to change the heat transfer of the leading 20-40% of the airfoil, but further downstream the heat transfer enhancements were seen to decrease as the turbulence intensity increased [38]. It should be noted that the tested roughness models of this study were uniform and systematic, unlike real ice accretions.

Dunkhan et al. [39] continued the work of Poinsatte et al. [30], Bragg et al. [37], and Bragg et al. [38] by studying the heat transfer enhancement using two aluminum cast surfaces of ice accretions created in the IRT. The aluminum castings were instrumented with heat flux gauges to measure the heat transfer along the surface. The results of this study showed generally higher convective heat transfer values than those achieved by Poinsatte et al. [30] and Bragg et al. [38] using the hemispherical roughness elements, suggesting that the hemispherical ordered elements were not able to replicate the results of real ice roughness. A picture of an aluminum casting of a glaze ice accretion used in this study can be seen in Figure 2.8. Han and Palacios [40] used a similar method to Dunkhan et al. [39] based on infrared thermography. The study used urethane liquid plastic castings to model realistic ice roughness, then compared the heat transfer results from the castings to those predicted using the LEWICE code. LEWICE was found to drastically ovepredict the peak experimental heat transfer coefficient values by 200%-391% [40] when compared to traditional models used for dry ice accretions.

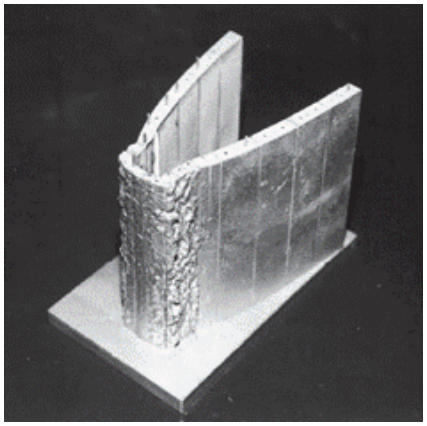

Figure 2.8: Aluminum Casting of Glaze Ice Accretion on a NACA 0012 Airfoil [39]

Anderson et al. [16] studied the roughness characteristics of ice accretions formed in the NASA Glenn IRT on NACA 0012 airfoils of differing sizes. The airfoils were exposed to Appendix C conditions, with varying LWC. Shin [6] also studied the effects of changing LWC and temperature on ice accretions created on a NACA 0012 airfoil in the IRT. He observed these parameters having a direct effect on the roughness height. Both studies confirmed that varying different parameters of the ice accretions effect the location of the smooth-to-rough transition [6], [16].

Croce et al. [41] wanted to remove empirical correlations for ice accretion prediction by developing a Lagrangian simulation technique for ice shapes. The simulation was embedded into an accretion code called FENSAP-ICE and was designed to account for additional stochastic processes of ice accretion such as: bead nucleation, growth, and coalescence into water films or moving droplets. The model was developed by studying the motion and interactions of single droplets impacting an airfoil surface. Tecson and McClain [43] developed a similar Lagrangian droplet simulation for droplets impinging a flat surface to create realistic ice roughness distributions of Appendix C conditions. The simulated surfaces were manipulated to have surface characteristics

matching those studied by Shin [6] and Anderson et al. [16]. The droplet simulator outputs a roughness distribution with random bead diameters and is able to avoid bead overlap while still having random bead location and spacing. Tecson and McClain [43] tested solid models of surfaces created using the Lagrangian droplet simulation of Tecson and McClain [42] to determine the convective heat transfer of the hemispherical elements in flows with negligible freestream acceleration and a constant flux boundary condition. Walker et al. [44] later investigated the same surfaces with varying flux boundary conditions to analyze any convective heat transfer enhancements. This study observed that varying the thermal boundary conditions had little effect on the convective heat transfer.

In 2014, McClain et al. [45] studied ice accretion on a NACA 0012 airfoil during short duration SLD icing events in the IRT. Ice roughness was created on airfoils under differing conditions with different exposure times to characterize roughness development. This study concluded that ice roughness increases proportionally to accretion time or accumulation parameter. The study was also able to conclude that while the roughness height is thought to be most heavily influenced by accumulation parameter, the MVD of the droplet cloud also influences the roughness variation on a surface [45]. The four real ice roughness surfaces used for the current study were created during this experimentation.

With the development of laser scanning technology producing more detailed representations of ice roughness than ever before, interest arose to reevaluate the Appendix C ice roughness historically used in icing studies. McClain et al. [46] used the SOM method of McClain and Kreeger [47], which will be discussed in the next section,

to characterize the ice shapes created in these icing conditions and evaluated the variations along the surface. The roughness parameters found using this method were then compared to those historically measured for Appendix C ice roughness. This study found that the differences in the parameters could only be attributed to a difference in experimental methods between studies. However, the laser scan data was able to provide significant advancement into the ice roughness formation and development on a surface exposed to Appendix C conditions.

Shannon and McClain [48] investigated two more surfaces created using the Lagrangian droplet simulator of Tecson and McClain [42]. One surface was created with an abrupt smooth-to-rough transition location as is common in historical roughness studies, while the second surface had roughness heights scaled to match the measured height variations from a laser scanned ice accretion formed in the IRT. This second surface had a more gradual smooth-to-rough transition. The study exposed the surfaces to accelerating freestream velocity using a ceiling insert which was created to mimic the flow acceleration along an airfoil. The surfaces were fabricated from both ABS plastic and CNC machined aluminum, and then exposed to negligible flow acceleration and accelerating flow for data comparison purposes. When the surfaces were exposed to negligible flow acceleration, the difference in smooth-to-rough transition had little effect on the convective heat transfer downstream. For the accelerating flow cases the surface with the more gradual roughness transition was observed to have lower heat transfer. This is believed to be caused by the lower turbulence intensity from the more realistic ice replication.

The ceiling insert created for testing by Shannon and McClain [48] could not correctly model the leading 2% chord of the plate. Hughes et al. [49] was able to overcome this using the Vertical Icing Studies Tunnel (VIST) at NASA Glenn. The study focused on the convective heat transfer of roughness elements in the stagnation region of Lagrangian droplet simulated surfaces. The results, combined with those of Tecson and McClain [43] and Shannon and McClain [48] allowed a full description of the heat transfer associated with the leading edge roughness formation.

McClain et al. [50] then studied the differences in ice roughness accreted on airfoils of two different sizes with the same Weber numbers in the IRT. The object of this study was to observe the variations in glaze ice conditions when scaled to different airfoil sizes. This study found that on a glaze ice surface, liquid film physics are more important than collection physics, and that downstream of the glaze-ice plateau, ice thickness and roughness scaled with the rime-ice stagnation thickness match for Weber number scaled icing conditions.

Hawkins [12] expanded more upon the results of Shannon and McClain [48] by introducing a real ice roughness surface for comparison to the gradual smooth-to-rough transition Lagrangian surface from Shannon and McClain [48]. The real ice surface was created from an unwrapped laser scan of the roughness, with no alteration to the shape or distribution of the roughness elements. The two surfaces were expected to give similar results when exposed to the same flow and heating conditions. The effect of a leading edge trip to induce early transition to turbulent flow on the convective heat transfer was also assessed in this study. It was found that the addition of the leading edge trip did not have any dramatic effect on the heat transfer of the surfaces studied. The important

conclusion of this study was the heat transfer results were not similar between the real ice surface and the realistic ice surface created using the Lagrangian droplet simulator. This suggests the need for the development of a new surface modeling technique.

Recently McClain et al. [20] studied the ice roughness and thickness evolution on a swept airfoil using the IRT. The airfoils were exposed to both Appendix C and Appendix O conditions and compared to roughness formation results for straight airfoils. The maximum roughness values were found to follow the same development trend of that on a straight wing. The spatial variation of roughness on a swept wing reached an asymptotic time value, after which the spatial variations seen in the roughness matched those seen in roughness forming on straight airfoils.

Surface Roughness Background

Surface Roughness Measurement

In 1987 Reehorst and Richter [51] described the two most common methods used in ice shape characterization, ice tracing and casting. The casting method requires a mold to be created from the ice shape. Once the mold has hardened, a casting is created to form a replication of the ice shape. Initially these molds were created from hot wax, but are now fabricated from materials that introduce less heat to the ice surface prior to measurement. The ice tracing method has also been used to characterize ice accretions in only two dimensions. This method uses a hot piece of metal or wire to melt a slot in the chordwise plane of the ice. A piece of cardboard is then inserted into the slot and the ice shape is traced onto the cardboard by hand [52],[53].

One of the biggest issues with ice tracing is the addition of heat prior to ice shape measurement. Melting the ice to create a slot for the cardboard can alter and deform the ice shape. The tracing accuracy is also subject to the tracer; the same ice shape traced by two different people has been seen to vary by as much as a few millimeters in certain areas [52]. The accuracy of the casting method is subject to the grain size of the casting material. If the material grains are larger than some of the ice shape details, those smaller details will not be captured in the casting [51].

Experimentalists began photographing the ice accretions for data collection in an attempt to capture surface roughness more accurately, without surface destruction prior to measurement. Shin [6] was one of the first to do this using a single camera and a ruler to obtain geometric details of the roughness elements. When reproducing the method from Shin [6], Anderson et al. [16] found issues with calibrating the images and defining the roughness features. Some of these issues arose due to the curvature of the airfoil combined with the angle of the camera. As a result, the data obtained using this method was considered fairly subjective [16]. Photographic data collection methods have now advanced to be able to capture an entire three dimensional surface. While this is desirable due to the lack of ice shape destruction, the process has proven to be very complex, requiring multiple cameras at multiple angles, complex calibration processes, and labor intensive data reduction [16].

Laser scanning was of growing interest when Lee et al. [53] evaluated seven different commercial laser scanners for the purposes of scanning ice shapes. The goal of the laser scanning was to record all of the 3D geometric elements of the ice shape in a non-destructive manner, requiring minimal instrumentation, and less complex data

reduction. The ice shapes needed to be painted with a highly reflective white paint prior to scanning for the laser scanners to properly capture the accretion details [53]. The laser scans resulted in point clouds of data that were analyzed in GeoMagic and found to replicate ice shapes like those seen in Figure 2.9. Laser scanning is the most common technology used in modern surface roughness studies.

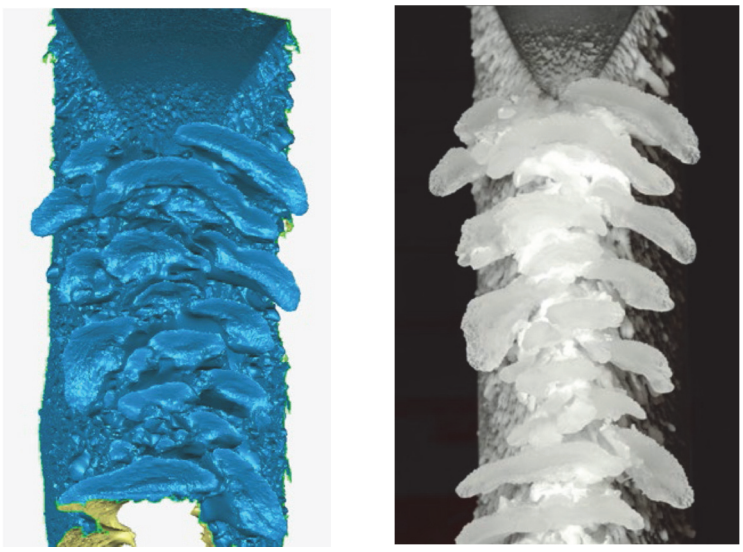

Figure 2.9: 3D Scallop Ice Shape (a) Laser Scan (b) Photograph [53]

With the growing popularity of laser scanning in ice accretion studies, a need arose to quickly and efficiently analyze the noisy scan data. In 2011, McClain et al. [54] introduced the idea of using a self-organizing map (SOM) approach for laser scan data analysis. The SOM approach uses codebook vectors to represent 3D clumps of data in a 2D space using a series of iterative moves, allowing large, noisy clumps of data to be reduced to concise, manageable levels. McClain and Kreeger [47] further refined this method to be used in processing data from a 3D laser scanner and be able to resolve detailed ice shape surface roughness based on the mean ice shape. This refinement allowed the ice shapes to be geometrically unwrapped from the known airfoil surface to a

flat plate representation for experimental purposes. This was done using the 99.9% maximum roughness height (RMH) based on a Gaussian distribution for the laser scan data. The calculation of the RMH values for a surface can be performed using the root mean square roughness height for the surface, R_q or RMS. The equations used to calculate the surface RMS and R_q are presented in Eq. (2.24) and Eq. (2.25), respectively.

$$R_q = RMS = \left[\frac{1}{J}\sum_{j=1}^{J} N_{x^j}{}^2\right]^{\frac{1}{2}} \tag{2.24}$$

$$RMH_{b^n} = 3.09R_q = 3.09\left[\frac{1}{J}\sum_{j=1}^{J} N_{x^j}{}^2\right]^{\frac{1}{2}} \tag{2.25}$$

where N_{x^j} is the normal height of the point x^j , J is the number of points on the surface for which b_n is the winning vector. The result of the SOM analyses and statistics from the scanned surfaces can then be presented in multiple ways using the Airfoil Roughness Evaluation System (ARES), which was created by McClain **Error! Reference source not found.** to perform the analysis of the laser scan point cloud data and display the results. An X-Y projection of processed laser scan data created in ARES for a surface used in the current study is shown in Figure 2.10.

The objective of this investigation is to expand on the studies of Tecson and McClain [42][43], Walker et al. [44], Shannon and McClain [48], Hughes et al. [49], and Hawkins [12] by creating three new real ice surfaces from unwrapped laser scans of ice accretions created in the IRT. As with the previous studies, the surfaces will be fabricated from both 3D printed ABS plastic and CNC machined aluminum. These three surfaces combined with the real ice surface created by Hawkins [12] will form a progression of surface roughness formation with increasing exposure time to icing conditions. The convective heat transfer coefficients and velocity boundary layer profiles will be

measured along the roughness surfaces. All data recorded in this study will be used to improve the heat transfer prediction capabilities of LEWICE.

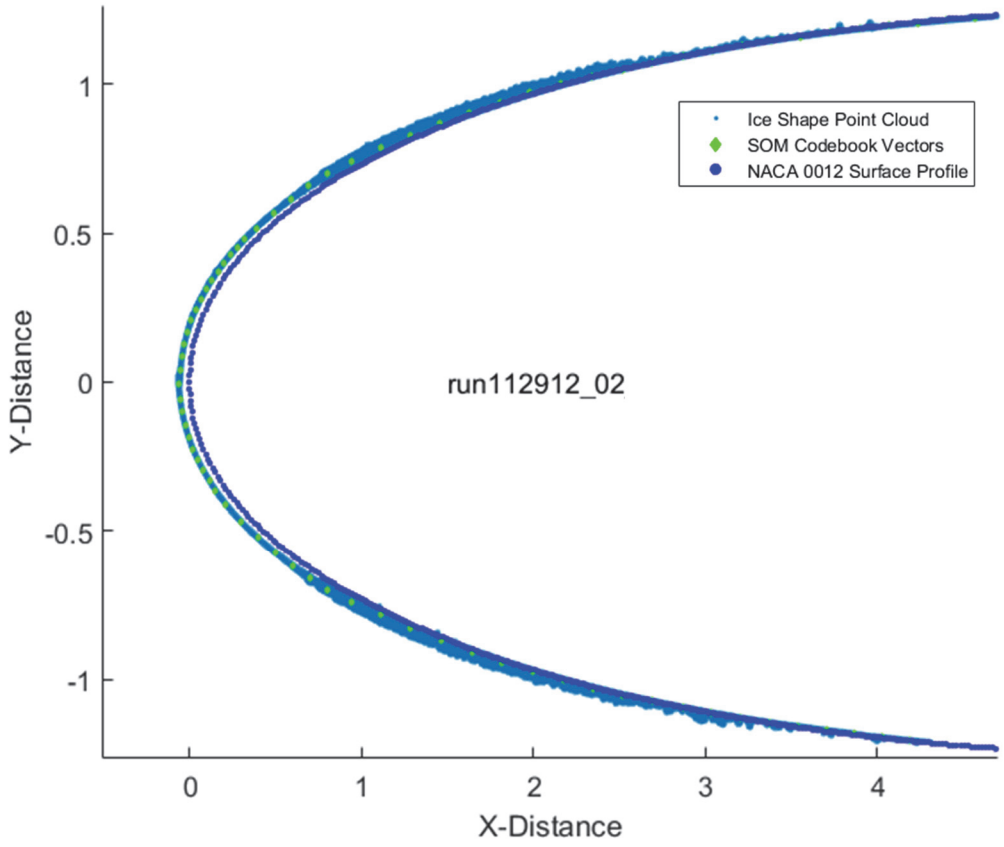

Figure 2.10: X-Y Surface Projection Created Using ARES

CHAPTER THREE

Materials and Methodology

Four real ice surfaces were made to replicate ice accretions created in the IRT at NASA Glenn Research Center. Experiments were performed on these four surfaces to characterize the convective heat transfer occurring on surfaces experiencing real ice roughness. The surfaces were also studied to find the velocity profile changes that occur in the presence of roughness. This section will describe the real ice roughness surfaces and their creation along with the fixtures and procedures used in the experimentation. Finally, this section will detail the data reduction processes used for the two different types of experimental data.

Ice Roughness Surfaces

Four surfaces were chosen from a number of ice accretions created by McClain et al. [45] in the IRT. Three of the surfaces were created and analyzed for this study, while another was used in a previous study by Hawkins [12]. The convective heat transfer of all four surfaces formed with different exposure times is of great interest.

Surface Generation

This investigation focused on Appendix O ice roughness conditions, or supercooled large droplets (SLD). These conditions are of greatest concern in the current aircraft industry based on the FAA standards for safety in flight. Historically the icing conditions of greatest concern were the Appendix C conditions, but this study focused on Appendix O conditions. Aside from differing MVD of the two icing conditions, all other

parameters were set to match those of a previous study by Anderson et al. [16] in Appendix C conditions. The four surfaces investigated were created during an experiment done by McClain et al. in 2014 [45] which studied ice roughness formation in short duration SLD icing events.

For all testing, a 21 inch (53.3 cm) NACA 0012 airfoil spanning the entire 72 inch (182.9 cm) test section was placed within the IRT and set with a 0° angle of attack. The freestream tunnel velocity, freestream total temperature, freezing fraction, and cloud LWC were all kept constant for this study 129.7 knots (66.723 m/s), 27.7 ± 0.1 °F, 0.217, and 0.60 gm/m^3, respectively. The properties of each surface are provided in Table 3.1.

Table 3.1: Properties of the Four Studied Surfaces

Case Identifier	T_t (°F)	V (knots)	MVD (μm)	LWC (gm/m^3)	Δt_s (s)	A_c	β_0	$\overline{N}_{0,R}$ (mm)
113012.05	27.7	129.7	150	0.6	43	0.112	0.969	0.92
112912.02	27.8	129.7	100	0.6	55	0.143	0.950	1.15
113012.04	27.7	129.7	150	0.6	75	0.195	0.969	1.60
112912.06	27.7	129.7	150	0.6	94	0.245	0.969	2.00

Table 3.1 also shows that three of the four surfaces were exposed to droplets with an MVD of 150 μm, while the remaining surface experienced droplets with an MVD of 100 μm. This is because, from the testing done by McClain et al. [45], the case with an MVD of 150 μm following the trend of increasing accumulation parameter and exposure time showed significant spanwise variation. Spanwise variation of this magnitude suggests the occurrence of an error during laser scanning. After analyzing the closest case with a smaller MVD but similar accretion parameter and finding no spanwise variation, the 100 μm MVD case was determined to be the better option. In each of the tests performed by McClain et al. [45] the airfoil was exposed to similar icing conditions for a

different amount of time. This exposure time difference affected the accumulation parameter associated with those conditions.

Once the designated exposure time was reached, the wind tunnel velocity was reduced to approximately 5 m/s and the temperature was held around -4˚C to avoid thawing. The ice accretions were painted with alcohol-based titanium dioxide paint, and then the ROMER Absolute Arm was placed in the IRT test section and used to scan the leading 120-150 mm of both sides of the airfoil leading edge. The scans were approximately 100 cm in the spanwise direction and were performed at the center span location of the airfoil. The elevation maps of the laser scans performed for this study are depicted in Figure 3.1.

The four studied surfaces were categorized based on the date of the roughness scanning and the chronological order of the scan with respect to others performed on the same date. For example, the real ice roughness surface labeled 113012.05 was performed on November 30th, 2012, and was the fifth scan performed on that day. The four surfaces analyzed in this study have been identified as 113012.05, 112912.02, 113012.04, and 112912.06, in order of increasing accumulation parameter. The 113012.04 surface was previously analyzed by Hawkins [12], but will also be included in this analysis to see the effect of temporal roughness development.

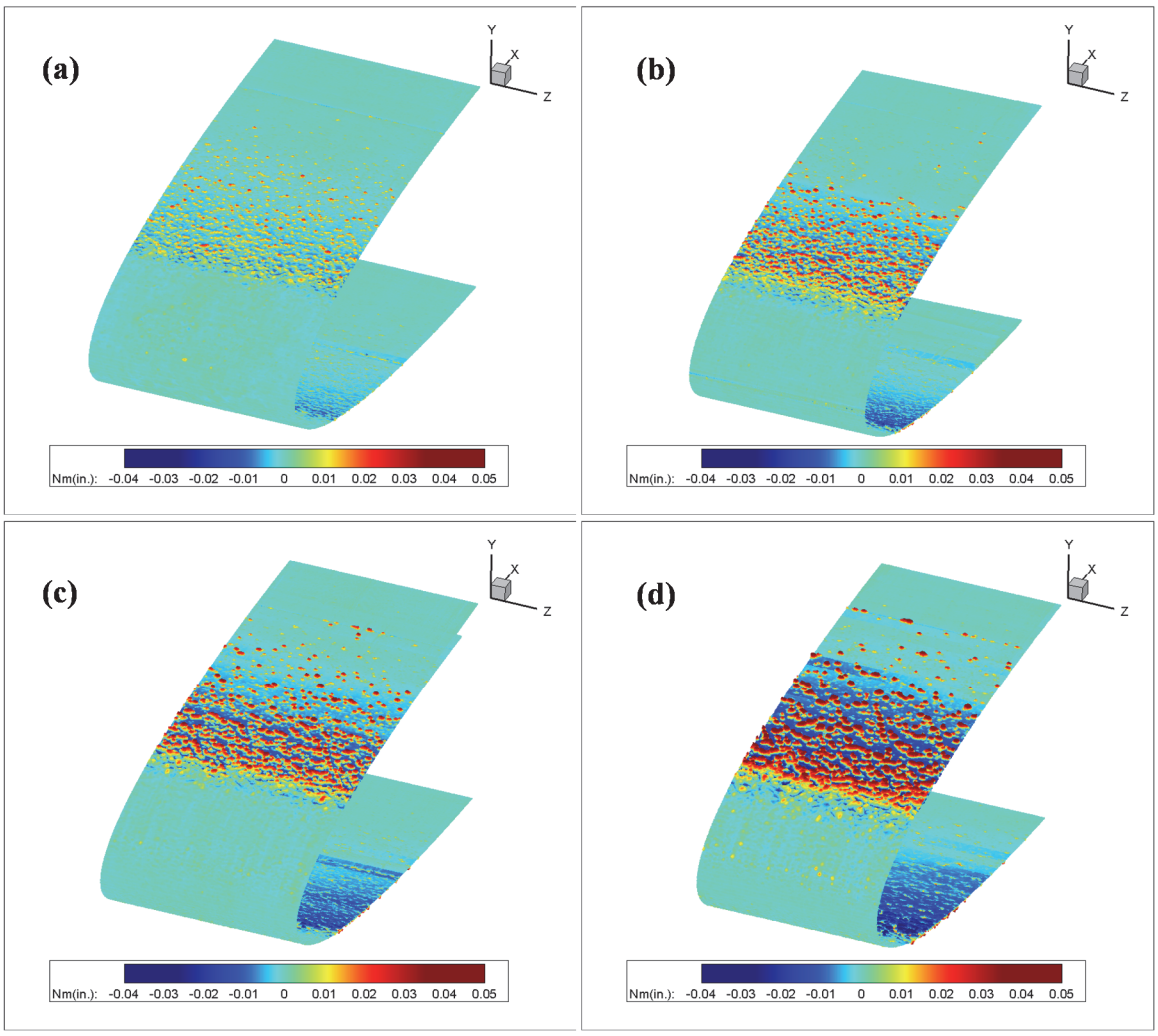

Figure 3.1: Laser Scanned Roughness Data (a) 113012.05, (b) 112912.02, (c) 113012.04, (d) 112912.06

A geometric scaling of x10 was applied to the roughness dimensions and the surface distance from the leading edge for purposes of Reynolds number scaling, which will be discussed later in this chapter. Therefore, all the surfaces created from the laser scan data were increased in scale by a factor of 10.

The real ice roughness surface creation involved many steps. First, the laser scanned roughness data was deconstructed into 12 surface panels using a MATLAB code and saved as 12 separate STL files. The first column of all tested surfaces consisted of the same smooth surface panels due to the relatively negligible roughness near the stagnation

region of an airfoil; this was used as a control region and not reprinted for each surface. Next, the STL files were imported into SolidWorks to generate solid models of the roughness distribution on each surface panel. The surface panels were then manufactured using 3D printing processes. A Dimension 768 SST was used to print ABS plastic models of the surface panels. The test row (row C in Figure 3.7) was also manufactured from 6061 aluminum using CNC machining. Holes were drilled into the surfaces for attachment to the test plate, and then 1/16" neoprene gaskets were affixed to the bottom of each surface panel. For the heated section, the gasket allowed for even contact between each panel and its respective Mylar film heater. For the rest of the panels the gasket was used purely for height matching with the heated panels. Lastly, the manufactured panels for Row C (the heated section) were spray painted with flat black paint to provide a known surface emissivity of 0.95. Figure 3.2 and 3.3 depict an aluminum test row before painting and a full plastic 3D printed surface, respectively.

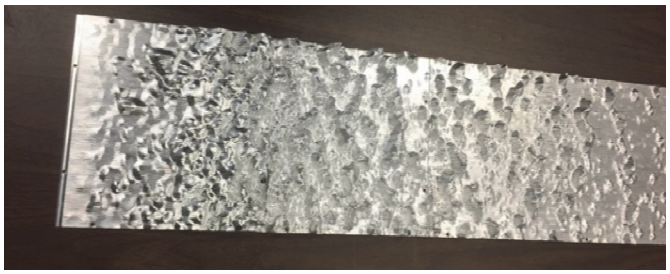

Figure 3.2: Unpainted Aluminum Roughness Surface

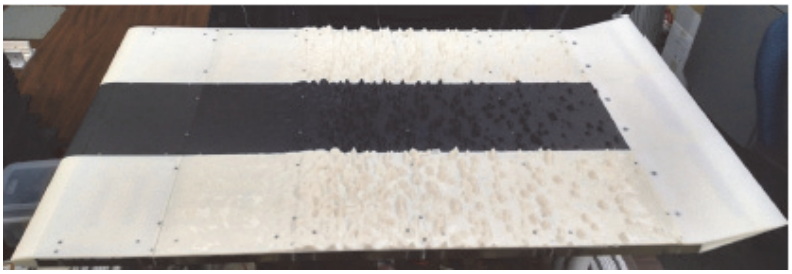

Figure 3.3: Full Plastic Real Ice Roughness Surface [12]

Convection Heat Transfer Testing

The heat transfer of real ice roughness surfaces was studied using an instrumented test plate, a wind tunnel ceiling insert, and four replicated real ice roughness surfaces. The creation and utilization of the test apparatus, the laser scan data reduction process, and the setup and procedure for this experiment will be described in the following sections.

Test Apparatus

The test apparatus used to perform the convective heat transfer testing required two major components: an instrumented test plate, and a ceiling insert to accelerate the flow over the plate. The creation and use of these two components will be discussed in the following sub-sections.

Instrumented test plate. The leading 17.1% (3.6") following the stagnation point of an airfoil is where most of the ice formation occurs during an accretion event. Therefore, the instrumented test plate used to perform the heat transfer experiments was designed to replicate that region of a NACA 0012 with a 21" chord, as used in the experiments of Anderson et al. [16]. To achieve better test resolution the surfaces were geometrically scaled using a factor of 10x the roughness height and distance from the leading edge. The fluid velocity experienced by the scaled surfaces needed to be decreased by a factor of 10 to match the Reynolds numbers achieved during the accretion events. This Reynolds number similarity allowed the results to be easily scaled and applied to real ice accretions. The instrumented test plate was fabricated by Tecson [8]. This fabrication will be briefly discussed in this paper for a general understanding of the

experimental setup, for more details refer to [8]. A solid model of the test plate is depicted in Figure 3.4.

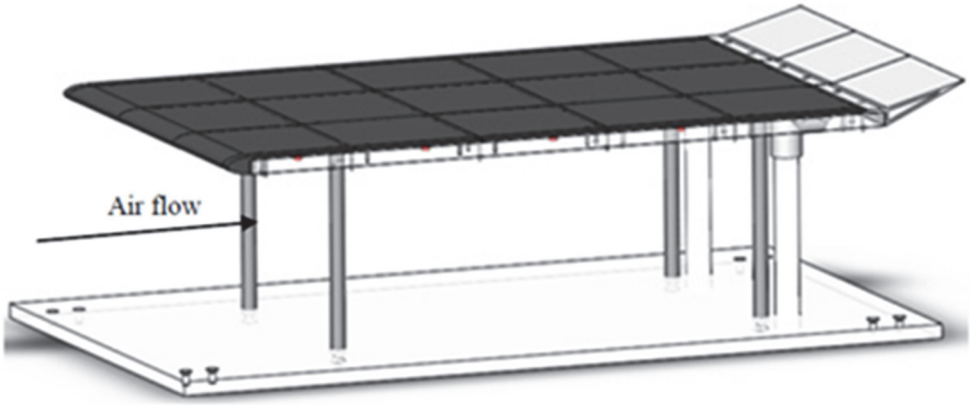

Figure 3.4: Solid Model of Instrumented Test Plate [8]

The base of the test plate is comprised of the Plexiglas sub-plate, which was fabricated from 3/4" thick Plexiglas with the dimensions of 24"x 36" to fit in the wind tunnel test section. Holes were drilled in the plate and used for the attachment of the test surface panels. The sub-plate was attached to the wind tunnel floor using steel rods. Channels were drilled into the plate for thermocouple and copper electrode placement on the top surface.

Five gold-deposited Mylar film heaters were installed onto the center row of the test plate for the purpose of heating the test panels. Each heater provided a constant heat flux boundary condition to one of the five heated sections. The heaters connected to the copper electrodes. Figure 3.5 shows the heater location on the test plate as the gray shaded region; the center row of the surface panels was designated as the test section for the convective heat transfer experiments.

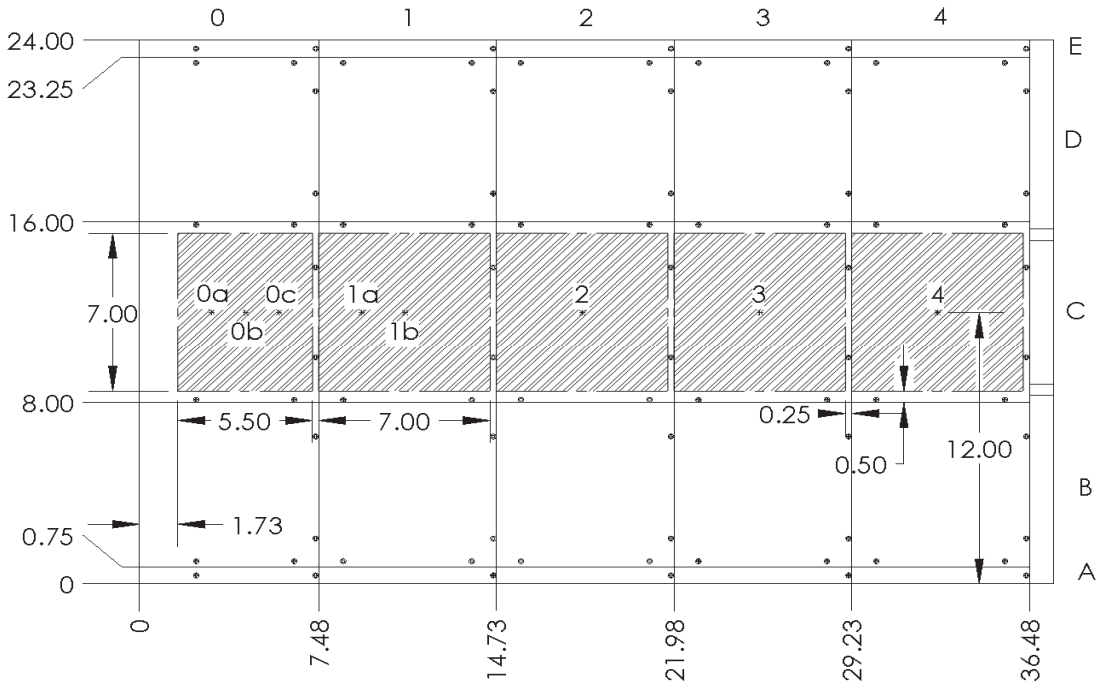

Figure 3.5: Mylar Heater Placement on Plexiglas sub-plate (flow from left to right) [8]

Type K thermocouples were installed into the thermocouple channels with the thermocouple beads aligned in the center of the test plate. One thermocouple was located at the center of each of the five heated sections, and then an additional three were placed toward the front of the plate where the most drastic changes in flow are expected. Two of these additional thermocouples were located in the first section while the third is located in the second section. Additional self-adhesive thermocouples were attached directly below the embedded thermocouples on the bottom side of the Plexiglas sub-plate for use in characterizing the heat loss through the test plate. Figure 3.5 depicts the placement of the thermocouple pairs on the sub-plate. Each pair was numbered with respect to the heated section in which it was located, with the addition of lettering for those sections including more than one pair.

Ceiling Insert. A ceiling insert was designed and attached to the ceiling of the wind tunnel test section to mimic the flow acceleration experienced by a 21" chord NACA 0012 airfoil at 0˚ angle of attack. The design and construction of this ceiling insert was performed by Shannon [10]. Enough information will be given for a fundamental understanding of the design and creation process. For a more thorough and complete description of the process, refer to Shannon [10]. A solid model of the fabricated ceiling insert is shown in Figure 3.6.

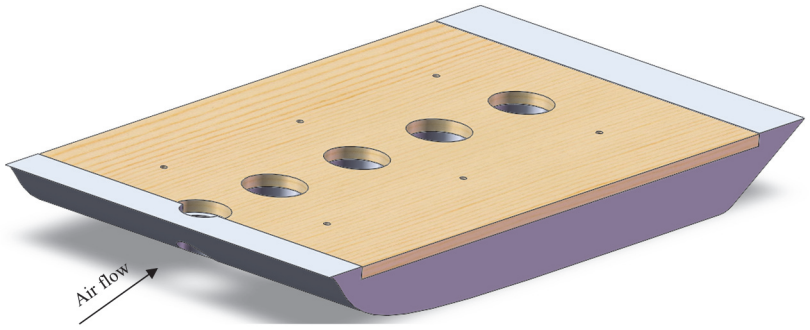

Figure 3.6: Solid Model of Ceiling Insert [10]

A vortex-panel solver was used to generate the pressure coefficient variation along the surface of a NACA 0012 airfoil. The resulting pressure coefficient distribution can be seen in Figure 3.7, where the region to the left of the vertical green line is the region of interest for this study, the leading 17.1%.

The pressure coefficient distribution was then converted into the velocity variation using a surface geometry scaling factor. The resulting velocity variation can be seen in Figure 3.8. It is evident in the figure that the leading 0.02% acceleration was not matched using the insert. When a flat plate is used to model flow acceleration, flow stagnation cannot be matched, so a cut-in velocity of 5 m/s was applied at the bullnose, causing the flow velocity to converge to that of an airfoil further down the plate. This

velocity variation was then used to compute the momentum thickness along the test plate surface. Finally, the thickness of the ceiling insert profile was calculated from the momentum thickness variation.

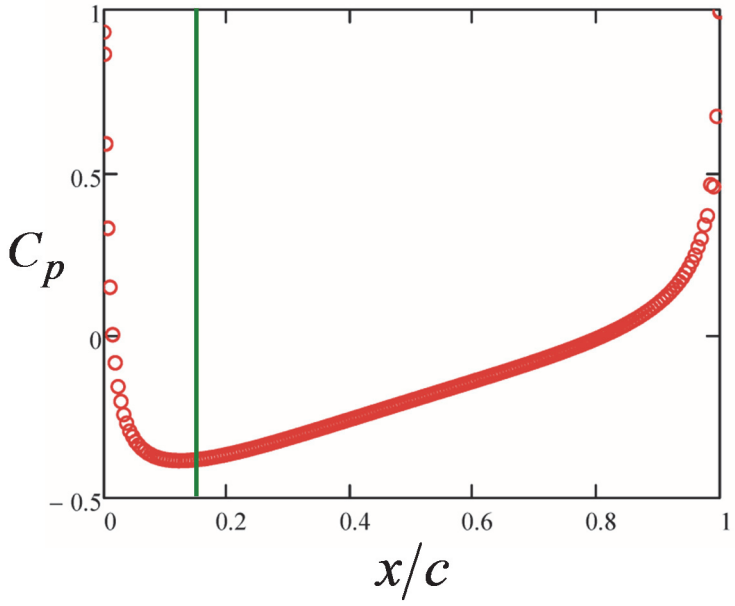

Figure 3.7: Pressure Coefficient Distribution over NACA 0012 Airfoil [10]

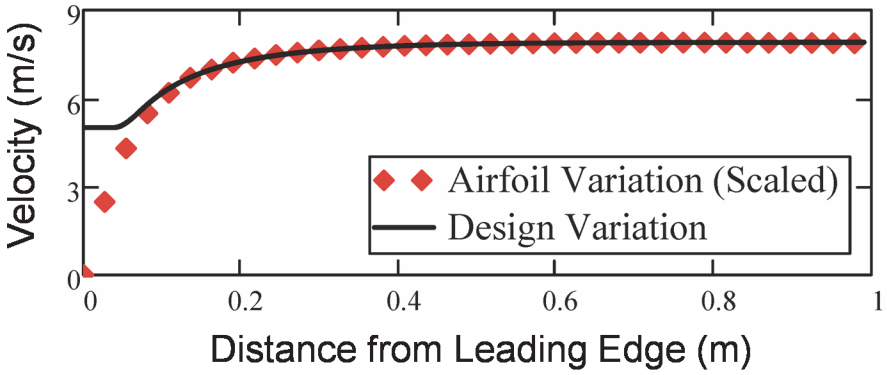

Figure 3.8: Scaled Airfoil and Design Velocity Variation [10]

The ceiling insert was made from a solid block of surfboard foam and includes a wooden panel for mounting to the ceiling of the wind tunnel test section. The insert also includes five viewing ports centered over each of the five surface panels of the test row

for measurement purposes during testing. The port closest to the leading edge is smaller than the rest in an effort to minimize its interference with the curved profile of the foam at the location. A solid model with these features included is pictured in Figure 3.6.

Laser Scan Data Processing

The laser scans of the real ice roughness profiles performed by the ROMER Absolute Arm resulted in point clouds of approximately one million points. This data needed to be reduced since this large quantity of points is not ideal for data processing. A method for this was developed by McClain et al. [54] and McClain and Kreeger [47] using Self Organizing Map (SOM) concepts. SOMs are neural-network approaches for representing noisy, multi-dimensional data in a lower-dimensional and nonlinear space. The technique uses codebook vectors to represent large clumps of data from the laser scans. The method then iterates to move the codebook vectors toward the closest clump of points until all of the codebook vectors are connected in a daisy-chain of vectors across the surface.

The resulting daisy-chain of codebook vectors represents the mean iced airfoil surface, also known as the ice manifold. The SOM approach assumes the manifold is a first-order, two-dimensional shape and that its local slope at each codebook vector is equal to the central finite-difference evaluated using the two closest codebook vectors. Deviations in the surface measurements normal to the line through its codebook vector are considered the 'height' of the surface point. Figure 3.9 depicts the coordinate system on the airfoil used to describe the mean ice manifold and the airfoil surface. Also evident is the X-Y, or chord-chord normal, plane.

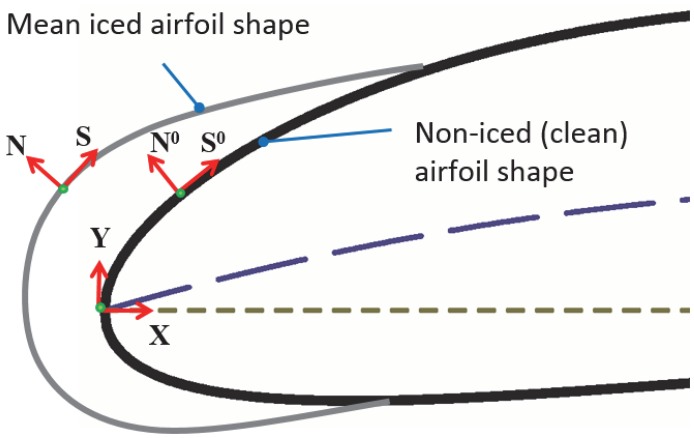

Figure 3.9: SOM Method Coordinate System [56]

In the SOM coordinate system, N is the direction normal to the ice manifold surface, while S is the direction along the surface. S is positive in the direction of flow. N^0 and S^0 can be described similarly, but with respect to the airfoil surface. For testing purposes the laser scanned surfaces needed to be unwrapped from the airfoil shape, to a flat plate surface. This required redefining the airfoil shape in terms of traditional x-y coordinates, using a discrete arc-length approach with the S and N coordinates. The arc length at one end of the daisy-chained codebook vectors was defined to be a known distance from the airfoil stagnation point, and the surface distance of each codebook vector was calculated as an S-distance along the ice manifold. At each codebook vector the RMH was calculated to determine the statistical distance in the N-direction (normal to the surface) away from the mean ice manifold. Converting S-distance from stagnation into x-distance from stagnation gives a skewed representation of a flat plate surface, as seen in Figure 3.10.

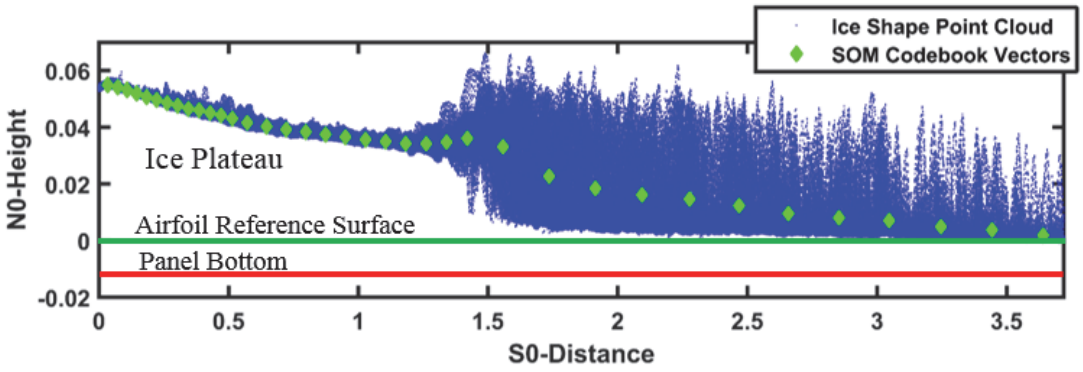

Figure 3.10: Surface Thickness Distribution of Laser Scanned Ice Roughness Points [12]

In Figure 3.10, the lowest relative height of the coordinates corresponds to the airfoil reference surface. It should be noted, however, that the first ten to fifteen inches of the scaled airfoil surface have only negligible surface roughness due to the glaze ice conditions; this region is referred to as the glaze ice plateau. This plateau is formed from a film liquid layer of droplets freezing near the stagnation point. Due to this formation, the leading edge points will only represent surface thickness, not roughness. For this study, the roughness associated with the glaze ice is considered negligible when compared to the roughness which builds during and after the smooth-to-rough transition. Since the glaze ice plateau was considered smooth, the data points in that area should have a nearly constant N^0 value, the next step in the adjustment was to 'level' all of the data points with respect to the leading edge. To focus on roughness instead of thickness, the point cloud clumps and their codebook vectors were shifted into S-N coordinates. This process makes thickness negligible so that only roughness remains on the mean ice manifold.

The results of the leveling process lower the points near the fifteen inch mark below the panel bottom, while the points near the rear of the airfoil were raised above the panel bottom. One more shift was applied to the data to maintain the relative roughness

features and allow it to sit flat with the panel surface. The final result was a geometrically accurate unwrapped point cloud on a surface resembling a flat plate. The resulting plot of the surface height per distance from stagnation point can be seen in Figure 3.11.

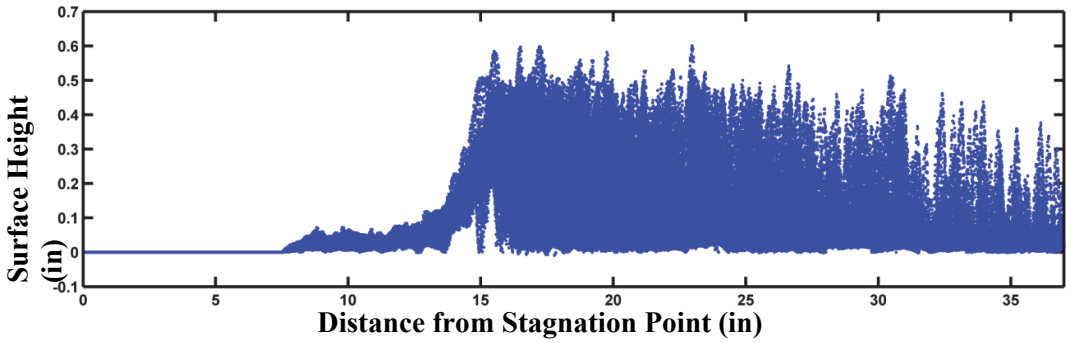

Figure 3.11: Surface Height Distribution of Laser Scanned Ice Roughness [12]

The process described above can be performed using the ARES code, which was created by McClain **Error! Reference source not found.**. This MATLAB code begins with the laser-scan point cloud, creates the codebook vectors, and unwraps the surface resulting in a point cloud like that depicted in Figure 3.11. The ARES code can also rotate the point cloud to account for swept wing angles or slight spanwise variation in laser scan data.

Once a point cloud was successfully leveled, a higher quality surface was created from the unwrapped surface map by interpolating and resampling the data. This was beneficial for manufacturing the 3D surface. A surface function fitting the point cloud was generated with a quadratic interpolation code, but was found to create sparse surfaces, with undesirably large gaps between data points. To combat this, the surface function was resampled for new surface points, which filled more of the surface gaps. When an STL file was created for the surface, this resampling improved the ability to

accurately 3D print and CNC machine the roughness. A newly leveled surface map can be seen in Figure 3.12 along with its resulting resampled surface.

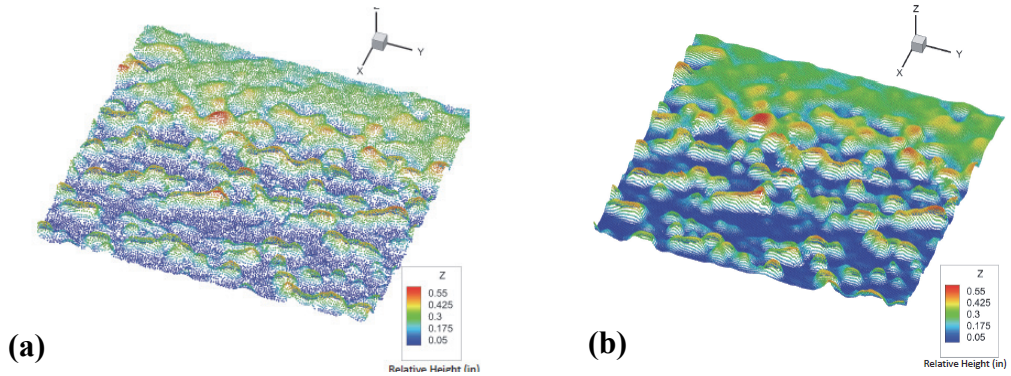

Figure 3.12: (a) Leveled Surface Height Map from Point Cloud, (b) Resampled Point Cloud Data Map [12]

Experimental Setup and Procedure

All heat transfer experimentation was done in the Baylor University Subsonic Wind Tunnel (BUSWT), which is a model 406B and was manufactured by Engineering Laboratory Design, Inc. This tunnel includes a 40 horsepower variable speed electric motor to drive its constant pitch fan. It is capable of airflow speeds of 0.1 m/s to 50 m/s with a velocity variation of less than ±1% within the 24"x 24" x 48" test section. The tunnel also includes a honeycomb inlet and three high porosity screens to provide a turbulence intensity of approximately 0.2% at the inlet. Figure 3.14(a) depicts the experimental setup for the heat transfer experiments.

A FLIR SC4000 ThermoVision Infrared camera with a 25 mm lens was used to take convection and radiation measurements during the heat transfer testing. The data from this camera was recorded using the ExamineIR software package created by FLIR. The SC4000 is capable of generating 320 by 256 pixel maps of the temperature distribution across a surface using an indium-antimonide detector. The images recorded

using this camera spanned a total area of 6.4” in the streamwise direction and 5.12” in the spanwise direction.

A 6” Pitot-static probe was paired with an Omega PCL-2A pressure transducer to monitor the freestream velocity. The ambient pressure, temperature, and relative humidity were measured using an Omega zSeries-THPB-LCD atmospheric conditions monitor. Additionally, a type K thermocouple was attached to the pitot-static probe to monitor the freestream temperature.

FLIR IRW-3C calcium-fluoride windows were installed into the five viewing ports in the ceiling of the wind tunnel to allow the IR camera to collect data over the center of each heated section of the test plate. An aluminum bracket was used to mount the IR camera to a Velmex traversing system, which was mounted to the ceiling of the wind tunnel test section. This traverse allows automated control of the camera position. Figure 3.13 shows the IR windows and the traverse system as they were installed into the test section of the BUSWT.

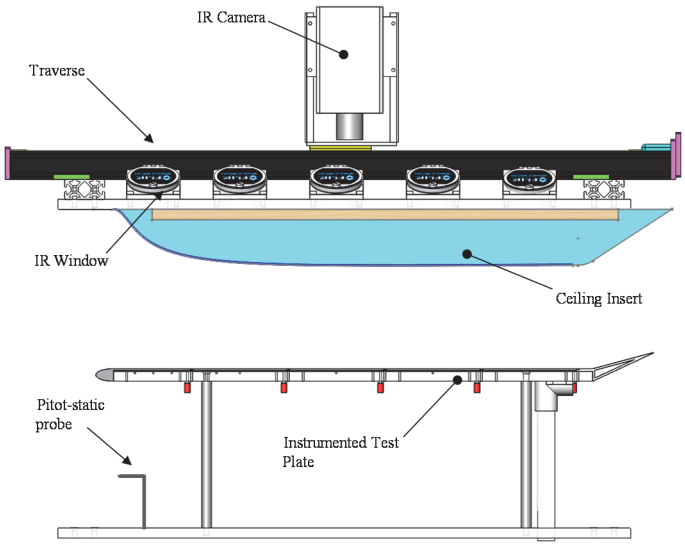

Figure 3.13: Side View of Test Section Setup [10]

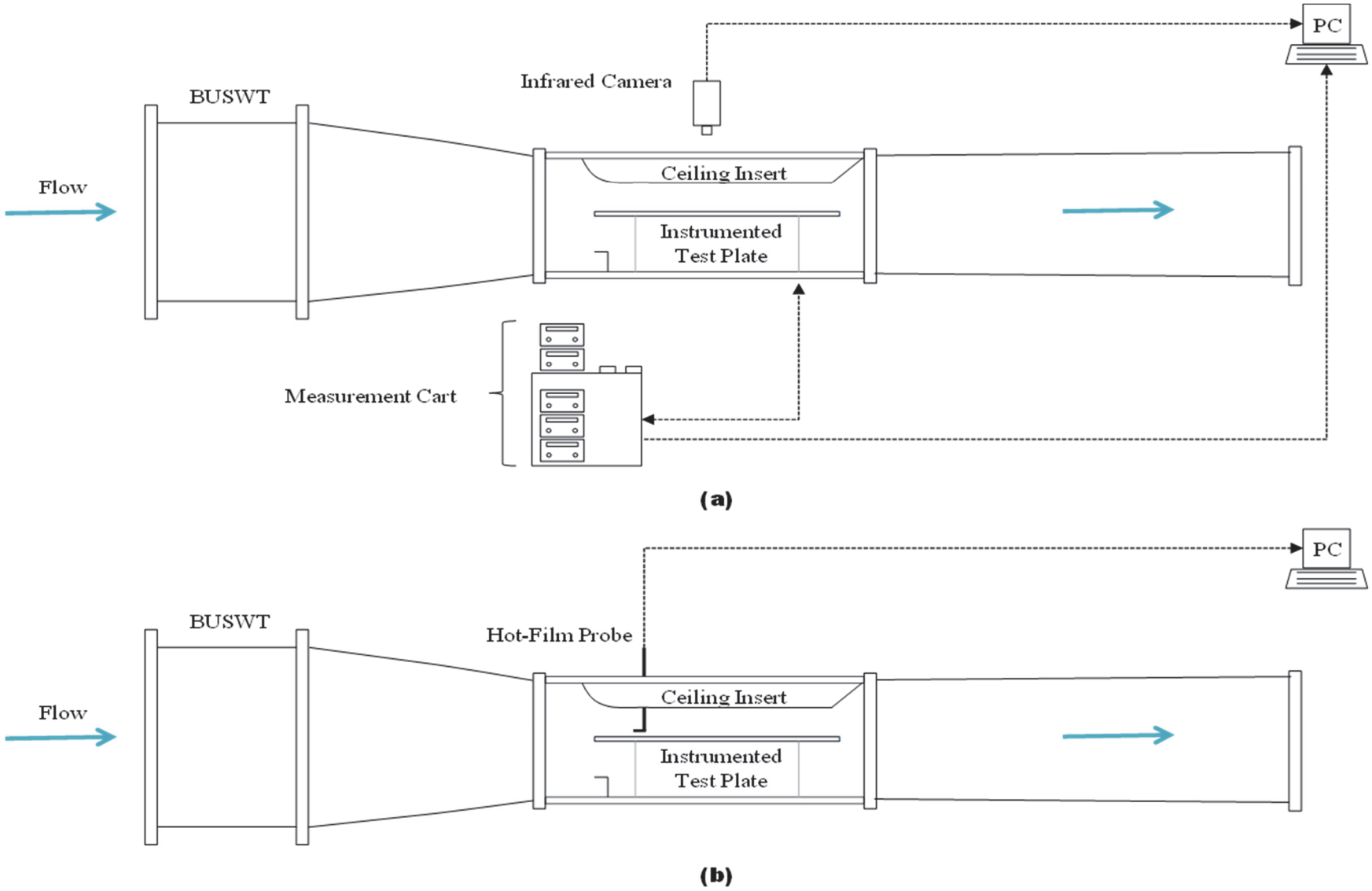

Figure 3.14: (a) Convective Heat Transfer Experimental Setup (b) Velocity Testing Experimental Setup [10]

For test cases involving negligible freestream acceleration (cases where no ceiling insert was used), the Pitot-static probe was installed in the ceiling of the wind tunnel test section. For the cases with freestream acceleration, the probe could not be installed into the ceiling due to interference with the ceiling insert. A calibration procedure was performed by Shannon [10] in order to ensure the correct freestream velocity was reached when the pitot-static probe was installed into the floor of the wind tunnel test section. This calibration determined a baseline pressure beneath the plate of approximately 0.1595 in H_2O was needed to match the flow conditions experienced over the top of the plate to those seen with negligible freestream acceleration. This pressure value was then used as a baseline for all of the accelerating flow experimentation, by matching this dynamic pressure each time, the desired flow velocity was ensured. For more information concerning this calibration process see Shannon [10]. The pitot-static probe placement for accelerating flow cases can be seen in Figure 3.14.

A wooden rolling cart was retro-fitted by Tecson [8] to house the majority of the test instrumentation including: power supplies, data acquisition (DAQ) modules, current transducers, and supermeters. Five BK Precision power supplies were used to supply power to the Mylar Film heaters; each heater had its own corresponding power supply. The voltage across each heater in sections 0-3 was measured using a National Instruments (NI) 9929 DAQ module. The current through sections 0-3 was measured using current transducers, Powertek CTH/20A/TH/24Vdc Type 1 for section 0 and Powertek CTH/10A/TH/24Vdc for sections 1-3. An NI 9205 DAQ module was used to read the outputs of these four transducers. The two NI DAQ modules (9929 and 9205) were then mounted in an NI cDAQ-9172 chassis. The current through and voltage across

the heater in section 4 were measured using two Newport TrueRMS HHM290/N Supermeters due to equipment availability. The freestream thermocouple along with the eight thermocouple pairs that were installed in the instrumented test plate were connected to five NI 9211 DAQ modules which were mounted in a separate NI cDAQ-9172 chassis. The outputs from the DAQ modules were interpreted by a LabVIEW program. Once all the instrumentation was connected, a black felt sheet was draped over the test section and the lights were dimmed to limit the amount of light pollution in the IR readings. The wooden instrumentation cart is depicted in Figure 3.15.

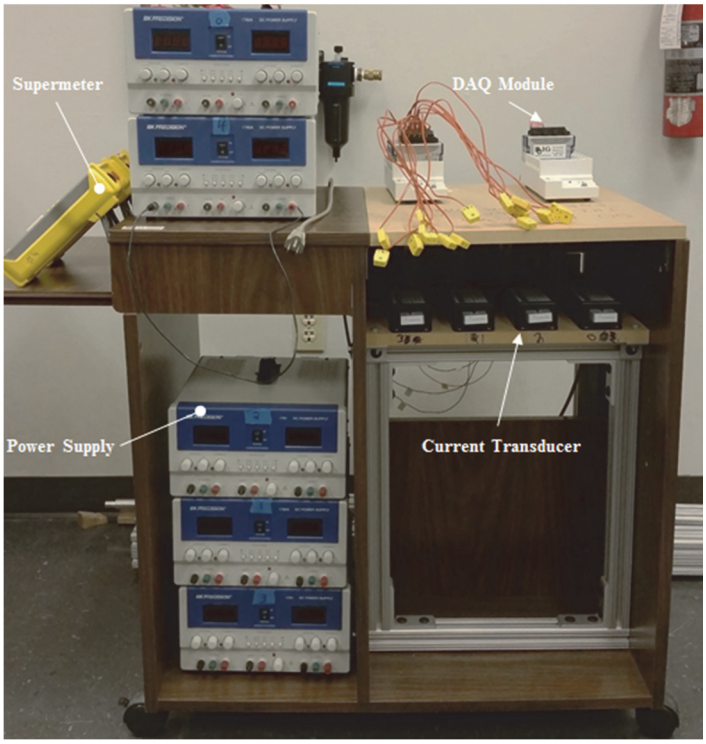

Figure 3.15: Wooden Cart Retrofitted for Experimental Equipment [10]

One day prior to testing, several preparatory procedures were performed. The surface to be tested was installed onto the instrumented test plate, and the test plate was then placed inside the test section of the wind tunnel. The pitot-static probe was inserted

in its respective place within the test section depending on the desired flow acceleration for the test. The wiring from the instrumentation on the test panel was connected to its corresponding equipment on the wooden cart, and the IR camera was focused. The sheet was then placed over the test section and the setup was left undisturbed overnight. This allowed all of the equipment and the ambient air to reach an equilibrium temperature before the testing began. The following is the procedure used to perform a convective heat transfer test:

1. The IR camera was turned on and left undisturbed for approximately 15 minutes in order for its detector to reach operating temperature.
2. The current transducers, DAQ modules, traversing system, and PCL-2A pressure transducer were powered on.
3. Three LabVIEW Programs were started. The first program read the DAQ, zSeries, and PCL-2A measurements. Voltage measurements were taken at 100 samples per second for 100 samples. Temperature measurements were performed at 3 samples per second for 21 samples. The second program controlled the position of the IR camera through the traversing system. Then the third program remotely controlled the speed of the wind tunnel fan.
4. ExamineIR software was started and calibration videos were taken at each of the five heated sections. The 70 frames were recorded at 7 frames per second for each heated section.
5. The PCL-2A pressure transducer was zeroed and the wind tunnel was started. The velocity of the tunnel was set according to the desired dynamic pressure.

6. The five power sources were turned on and the power was slowly increased until a nominal heat flux of 500 W/m^2 was provided to each heater.
7. The temperatures of the thermocouple pairs attached to the test plate were monitored using the LabVIEW program until steady state was achieved; this generally took 2 hours.
8. Steady state images were taken at each heated section using the same process that was used to take the calibration images.
9. The voltage and current in Section 4 was recorded manually when the images for the section were recorded.

Velocity Boundary Layer Measurements

The second set of tests performed on the ice roughness surfaces were hotwire anemometry tests. The data extracted from these tests were used to characterize the velocity boundary layer at the center of each heated section for each of the surfaces. The experimental setup and procedure will be described in the following section.

Experimental Setup and Procedure

The velocity boundary layer tests were performed in the same wind tunnel (BUSWT) and with a setup very similar to that used for the convective heat transfer tests. This setup is depicted in Figure 3.14 (b). The surface roughness sections were not heated for this test. The pitot-static probe, zSeries condition monitor, and PCL-2A pressure transducer were the only instrumentation carried over for this test. Another Velmex traverse system was added to the ceiling of the wind tunnel to allow vertical motion as well as horizontal. A model 1246-20 x-array hot-film probe was attached to the vertical

traverse using a probe holder. The setup is pictured in Figure 3.16. The probe was powered by a TSI Inc. IFA300 constant temperature anemometry system was used to collect velocity boundary layer data. ThermalPro software was utilized to assign channels to the x-array probe and initialize the IFA300 system.

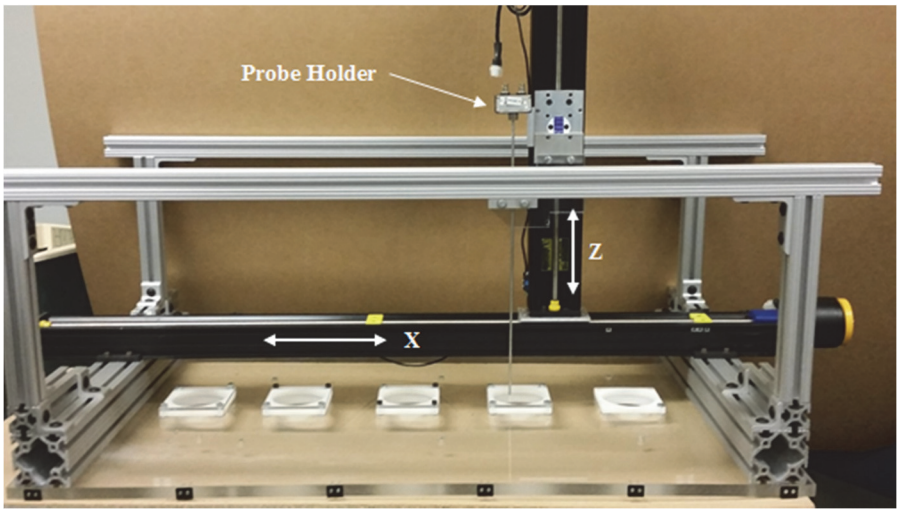

Figure 3.16: Wind Tunnel Ceiling with 2D Traverse System [10]

Prior to the boundary layer measurements, the x-array probe was calibrated. The probe was mounted to a Velmex B487TS rotary table at the same height as the pitot-static probe. The table was then rotated in 5˚ increments over a range of ±20˚ using a LabVIEW program. For each angle, a velocity sweep ranging from 0-20 m/s was performed. At each rotation angle and velocity, an NI 9223 DAQ module in an NI cDAQ-9178 chassis was used to acquire the velocity data from each wire.

For the velocity boundary layer measurements, the wind tunnel velocity was set using the same procedure and LabVIEW program as those discussed for the convection heat transfer tests. The hot-film probe was lowered through the viewing ports in the test section ceiling as close as possible to the test surface. The open viewing port was then

taped off to block the air flow, but not impeded the motion of the probe. A small piece of foam was placed around the probe holder to minimize any vibrations caused by the probe motion. Another LabVIEW program was used to move the probe vertically 6", through a 101 station, geometrically expanding grid with an expansion factor of 1.07. The velocity data at the 101 stations was acquired using the same system as the previously discussed calibration. 300,000 samples were taken at each station at a rate of 200,000 samples per second.

Data Reduction and Uncertainty Analysis

The data collected from the two types of tests required processing. This processing resulted in clearly interpreted result that could be used for comparison to past and future studies. The processes used for this data reduction are described in the sections to follow.

Heat Transfer Tests

The infrared and thermocouple data taken during the convective heat transfer tests required four additional components to become usable data. These components include: the data reduction equation, the ambient air properties, the temperature calibration, and the uncertainty analysis. These allowed the raw data to be transformed into values quantifying the convective heat transfer of the surface roughness being studied and are described in the subsections below.

Data reduction equation. Energy dissipation was modeled to track the heat transfer enhancement with different ice roughness shapes. Heat loss is a major factor in the energy leaving the system during a steady-state experiment. Hence, heat loss is a

vital part of the energy balance. Using the same methodology as Hawkins [12] and Shannon [10], a one-dimensional energy balance was applied to the test plate. Energy was supplied to the system through the Mylar film heaters, this was designated $\dot{Q}_{GEN}$. Heat conduction through the plate was designated as the heat loss, $\dot{Q}_{HL}$, which was recorded using the thermocouple pairs on the instrumented test plate. The rest of the heat was conducted through the Neoprene gasket and roughness surface panels, then either radiated or convected away. These values were designated $\dot{Q}_{RAD}$ and $\dot{Q}_{CONV}$, respectively, and where captured using the infrared camera. The resulting energy balance used for the data reduction of the system is given in Eq. (3.1). A schematic of the heat flow through one of the heated sections is depicted in Figure 3.17.

$$\dot{Q}_{GEN} = \dot{Q}_{HL} + \dot{Q}_{RAD} + \dot{Q}_{CONV} \tag{3.1}$$

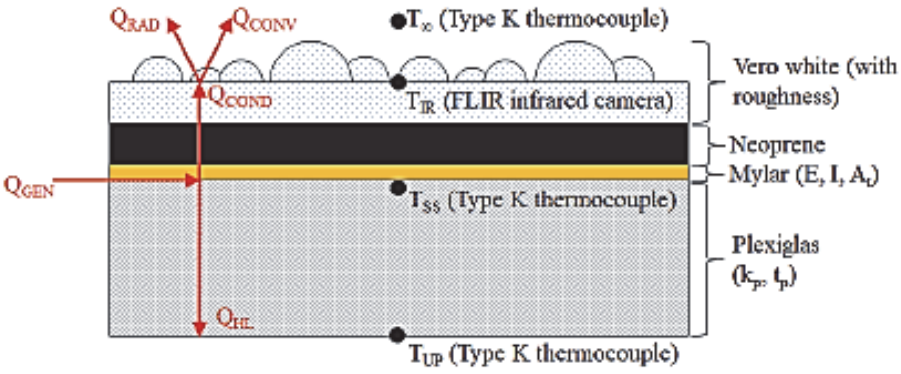

Figure 3.17: Schematic of Heat Flow through Heated Sections [10]

Shannon [10] began with Eq. (3.1) then inserted Fourier's Law of Conduction, Newton's Law of Cooling, Ohm's Law for Power, and Stefan Boltzmann's Law of radiation for $\dot{Q}_{HL}$, $\dot{Q}_{CONV}$, $\dot{Q}_{GEN}$, and $\dot{Q}_{RAD}$, respectively. Next, dividing by the pixel area

of the infrared camera images, and solving for the convective heat transfer coefficient h, Shannon [10] derived Eq. (3.2)

$$h = \frac{\frac{EI}{A_t} - C_k \frac{k_p(T_{SS} - T_{UP})}{t_p} - \varepsilon\sigma(T_{IR}^4 - T_\infty^4)}{(T_{IR} - T_\infty)} \tag{3.2}$$

under the assumptions that the Mylar film heaters generated a constant uniform flux [8], lateral conduction in the spanwise direction was negligible, and the heat lost through the test plate was constant across each heated section. The variable C_k that appears in Eq. (3.2) represents a calibrated conduction parameter. This parameter was derived by Walker [9] to adjust the conduction term of the energy balance. A conduction parameter was calculated for each heated section to account for the difference in thermocouple measurements that results from embedding the thermocouples in epoxy. This measurement discrepancy is a result of the differing thermal conductivities of the epoxy and the Plexiglas sub-plate. For more details about the derivation of the parameters, refer to Walker [9]. The resulting conduction parameters can be seen in Table 3.2.

Table 3.2: Calibrated Conduction Parameter Values [9]

Heated Section Number	C_k
0	0.90
1	0.90
2	1.05
3	1.10
4	1.05

Air properties. Multiple sets of data cannot be accurately compared until the properties of the air used during each test are taken into account. The data for this study was collected over a span of multiple weeks, so the air properties had potential to differ

greatly between data sets. For comparison purposes, the data was converted to non-dimensional Stanton numbers using the air properties. An Omega zSeries atmospheric conditions monitor was used to track the air pressure, temperature, and relative humidity at the inlet of the wind tunnel for the duration of the each test. Applying the same method as Tecson [8], Walker [9], Shannon [10], and Hawkins [12], a MathCad program based on the International Association for the Properties of Water and Steam guidelines [57], Wilke's equation for gas mixtures [58], and Sutherland's Law [59] was used to calculate additional properties using the measured values. These air properties included: air density, Prandtl number, specific heat, thermal conductivity, and dynamic viscosity.

Temperature calibration. The thermocouples for this study were calibrated *in situ* to an average group of pixels from the IR measurements. The IR camera measurements were considered accurate based on the experimentation of Walker [9]. The calibration equation resulting from this analysis can be seen in Eq. (3.3).

$$T_{TC,calibrated} = T_{TC,test} - (T_{TC,cal} - \overline{T}_{IR,cal}) \tag{3.3}$$

The $\overline{T}_{IR,cal}$ variable in this equation was achieved by averaging a square area of pixels around each thermocouple location. Since real ice roughness surfaces do not include repeating patterns of droplets, an area of ±1 inch in both the spanwise and streamwise directions from the thermocouple was selected for area averaging of the IR images. The average of the IR images was found for the designated region, and then used for comparison to the thermocouple data taken in that location. This averaging process was performed for all heated sections and all test surfaces with the exception of the third thermocouple on the first heated section (designated 0c in Figure 3.5) during the accelerated flow testing. This was due to the first hole in the ceiling insert being smaller

than the rest, so the IR images taken for section zero include part of the foam insert on the downstream end of the picture. This causes a skew in the heat transfer data for that thermocouple, so the foam region was cropped out of the data reduction and only ½ inch downstream of this thermocouple was used for the area averaging, while one inch was used in all other directions.

The thermocouple connected to the pitot static probe in the wind tunnel collected data for freestream temperature of the air throughout the entire test. These temperatures did not fluctuate much at the different locations along the plate, so the freestream temperature at each of the heated sections was averaged to yield one overall freestream temperature for association with the recorded data. The temperatures were averaged according to Eq. (3.4) below.

$$T_{\infty} = \frac{T_{FS_0} + T_{FS_1} + T_{FS_2} + T_{FS_3} + T_{FS_4}}{5} \tag{3.4}$$

Uncertainty analysis. The real ice roughness surfaces in this study have no repeated droplet pattern, unlike previous studies of similar nature that have been performed at Baylor. Heat flux is known to vary through different thicknesses, meaning that the average temperature for a 50 x 50 pixel area could vary greatly from the average temperature found using the entire 320 x 256 pixel frame. The uncertainty of each convective heat transfer coefficient found was calculated using the large sample size method of Coleman and Steele [60], which is based upon the work of Kline and McClintock [61]. This is the same method as that used by Walker [9], Shannon [10], Hughes [11], and Hawkins [12]. The total uncertainty for each of the measured values used to find the convective heat transfer coefficient (from Eq. (3.2)) is presented in Table 3.3. The random uncertainty was found using the statistical term known as Student's t-

value, the standard deviation of the data, and the sample size of the data in Eq. (3.5). For more detail about this analysis, refer to Shannon [10].

$$U_{random} = \frac{t \cdot S}{\sqrt{N}} \tag{3.5}$$

Table 3.3: Convective Heat Transfer Coefficient Measurement Uncertainty [10]

Variable	Total Uncertainty	Uncertainty Components
E	$\sqrt{U_{E,fixed}^2 + \left(\frac{tS_E}{\sqrt{N}}\right)^2}$	$U_{E,fixed} = 0.03\%\ E$ (sections 0 - 3) $U_{E,fixed} = 0.25\%\ E$ (section 4)
I	$\sqrt{U_{I,fixed}^2 + \left(\frac{tS_I}{\sqrt{N}}\right)^2}$	$U_{I,fixed} = 0.1$ A (section 0) $U_{I,fixed} = 0.05$ A (sections 1 - 3) $U_{I,fixed} = 2.5\%\ I$ (section 4)
A_t	$\sqrt{\left(U_{d,fixed} W_{ha}\right)^2 + \left(U_{d,fixed} L_{ha}\right)^2}$	$U_{d,fixed} = 1/32$ "
T_{IR}	$\sqrt{B_T^2 + \left(\frac{tS_{T_{IR}}}{\sqrt{N}}\right)^2}$	$B_T = 1.4\text{K}$
T_{SS}	$\sqrt{B_T^2 + \left(\frac{tS_{T_{IR}}}{\sqrt{N}}\right)_{cal}^2 + \left(\frac{tS_{T_{SS}}}{\sqrt{N}}\right)_{cal}^2 + \left(\frac{tS_{T_{SS}}}{\sqrt{N}}\right)_{test}^2}$	$B_T = 1.4\text{K}$
T_{UP}	$\sqrt{B_T^2 + \left(\frac{tS_{T_{IR}}}{\sqrt{N}}\right)_{cal}^2 + \left(\frac{tS_{T_{UP}}}{\sqrt{N}}\right)_{cal}^2 + \left(\frac{tS_{T_{UP}}}{\sqrt{N}}\right)_{test}^2}$	$B_T = 1.4\text{K}$
T_∞	$\sqrt{B_T^2 + \left(\frac{tS_{T_{IR}}}{\sqrt{N}}\right)_{cal}^2 + \left(\frac{tS_{T_\infty}}{\sqrt{N}}\right)_{test}^2}$	$B_T = 1.4\text{K}$

Velocity Boundary Layer Measurements

Additional steps also needed to be taken after the collection of the velocity boundary layer data. Calibration of the x-array probe was needed to ensure proper interpretation of the raw data, and the data needed to be further reduced into terms that were comparable with other data sets. Both of these processes are described in the sub-sections that follow.

Probe calibration. The x-array probe was calibrated using a rotary holder to sample different velocities at multiple angles. The probe calibration used for this study is the same as that used by Hawkins [12]. Each of the probe wires output a voltage that corresponded to the pressures found using a PCL-2A pressure transducer connected to a pitot-static probe. Bernoulli's equation was then used to convert these pressures into velocities. Eqs. (3.6) and (3.7) were then used to calculate the effective velocity experienced by each wire of the probe.

$$V_{eff,1} = \sqrt{(V_{meas}\ cos\ \alpha_1)^2 + \kappa^2 (V_{meas}\ sin\ \alpha_1)^2} \tag{3.6}$$

$$V_{eff,2} = \sqrt{(V_{meas}\ sin\ \alpha_2)^2 + \kappa^2 (V_{meas}\ sin\ \alpha_2)^2} \tag{3.7}$$

The α values in these equations represent the angle of the wires with respect to the flow direction. The κ value represents the tangential attenuation factor, 0.115 according to the manufacturer of the x-array probe used in this experimentation. The measured voltages of each wire were then plotted with the effective velocity values. These data points were then fitted using a fourth order polynomial fit. The resulting calibration curves are evident in Figure 3.18.

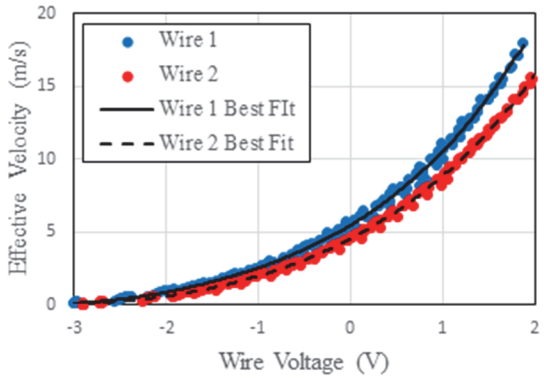

Figure 3.18: X-Array Probe Calibration Plot [12]

Data reduction equations. Following the calibration of the x-array probe, the flow velocity components experienced by the probe could be calculated. This process is described in Hawkins [12], and is very similar to that used by Shannon [10] but with double the amount of calibration points along the ±20˚ span. The normal and tangential velocity flow to Wire 1 of the probe was found using Eqs (3.8) and (3.9), respectively.

$$V_{N1} = \left(\frac{V_{eff,1}^2 - \kappa^2 V_{eff,2}^2}{1-\kappa^4} \right)^{1/2} \tag{3.8}$$

$$V_{T1} = \left(\frac{V_{eff,2}^2 - \kappa^2 V_{eff,1}^2}{1-\kappa^4} \right)^{1/2} \tag{3.9}$$

The two velocity components were then broken down into the x-direction and z-direction velocities relative to the probe using Eqs (3.10) and (3.11).

$$u_i = \frac{V_{T1} + V_{N1}}{\sqrt{2}} \tag{3.10}$$

$$w_i = \frac{V_{T1} - V_{N1}}{\sqrt{2}} \tag{3.11}$$

This resulted in 30,000 velocity components that were found for each of the measurement stations. The velocity components were then averaged using Eqs (3.12) and (3.13).

$$\overline{u} = \frac{1}{N} \sum_{i=1}^{N} u_i \tag{3.12}$$

$$\overline{w} = \frac{1}{N} \sum_{i=1}^{N} w_i \tag{3.13}$$

Finally, the root mean square turbulence velocity components were able to be calculated from all the information using Eqs (3.14) and (3.15).

$$u'_{RMS} = \sqrt{\frac{1}{N-1} \sum_{i=1}^{N} (u_i - \overline{u})^2} \tag{3.14}$$

$$w'_{RMS} = \sqrt{\frac{1}{N-1} \sum_{i=1}^{N} (w_i - \overline{w})^2} \tag{3.14}$$

CHAPTER FOUR

Results and Discussion

This chapter presents the test results for the convective heat transfer testing on all four surfaces experiencing both accelerating flow and flow with negligible freestream acceleration. Results are included for surfaces made from both plastic and aluminum. The real ice roughness case designated 113012.04 was presented previously by Hawkins [12]; the results were replicated to represent temporal ice roughness development for this study. The results of the velocity boundary layer measurements are also presented for the same flow conditions. The four roughness cases discussed in this study are 113012.05, 112912.02, 113012.04 [12], and 112912.06.

Ice Roughness Surfaces

The four ice roughness surfaces were made from laser scans of ice accretions created in the NASA Glenn IRT. Although the four roughness surfaces were created in similar cloud conditions, a significant difference is seen in the locations of both the smooth-to-rough transitions and the maximum roughness heights for each ice accretion. Figure 4.1 shows this location difference by plotting the root-mean-squared (RMS) roughness height, calculated using Eq. (2.24), on the surfaces with respect to spanwise location along the test plate. From Figure 4.1, the smooth-to-roughness transition occurs on surfaces 112912.02 and 112912.06 further upstream than it does on surfaces 113012.05 and 113012.04.The results of the geometric unwrapping of these laser scanned ice shapes are presented in Figure 4.2. The figure shows a roughness height map

of each surface as it was 3D printed or machined in order of increasing accumulation parameter. Both Figure 4.1 and Figure 4.2 show the roughness height increasing as a result of increasing accumulation parameter, which was expected based on the conclusions of McClain et al. [45]. The differing smooth-to-rough transition locations between surfaces are also evident in Figure 4.2. This difference of transition location demonstrates the truly stochastic nature of ice accretion. Figures 4.2 and 4.1 show that even though all of the surfaces were exposed to similar cloud conditions, there is still significant variability in the roughness characteristics, most obviously the smooth-to-rough transition location and maximum the roughness height location. The amount of variability in the surfaces suggests that there will always be statistical uncertainty associated with ice roughness formation. Figures 4.2 and 4.1 both show that as the accumulation parameter increases, so does the height of the roughness elements on the surface.

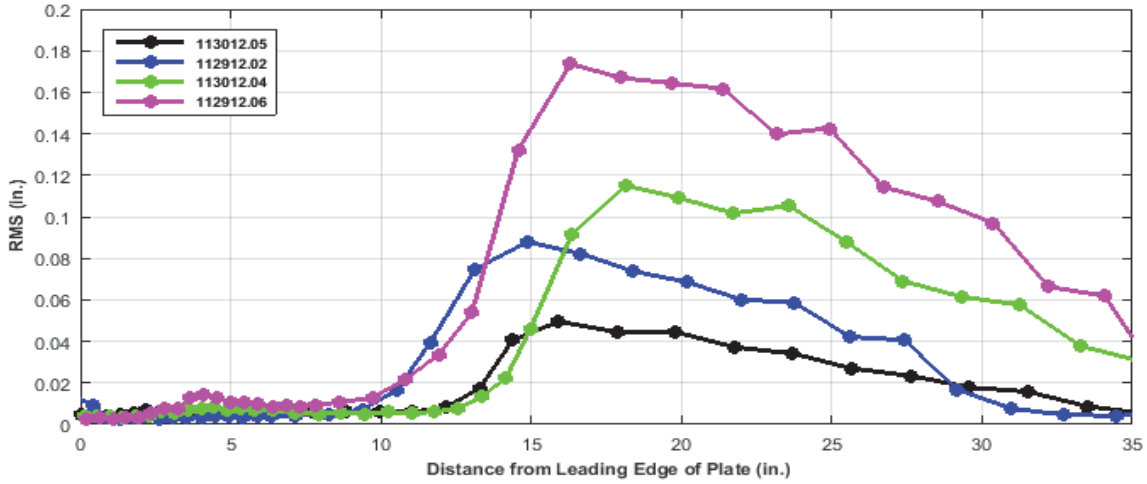

Figure 4.1: RMS vs. Distance from Leasing Edge of Plate for All Surfaces as Scaled and Printed

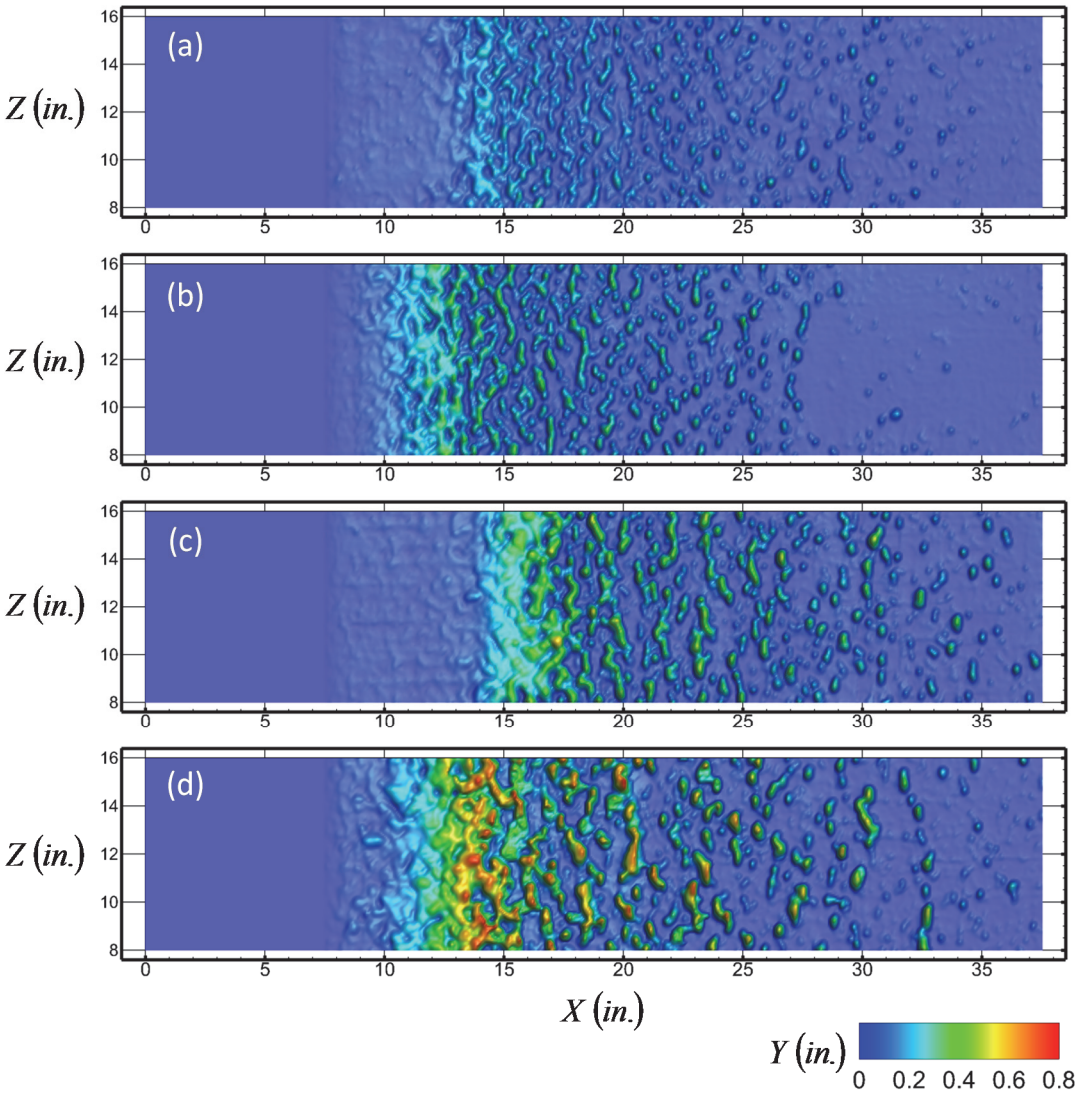

Figure 4.2: Roughness Height Distribution on Unwrapped Surfaces (a) 113012.05, (b) 112912.02, (c) 113012.04, (d) 112912.06 [62]

Heat Transfer Tests

The heat transfer measurements were taken using aluminum and plastic surface roughness panels employed in the test section. The roughness panels made from each material were tested in both accelerating and non-accelerating flow conditions. As a result, four tests were performed for each of the four real ice roughness surfaces for a

total of sixteen heat transfer data sets. The data collected during these tests can be found in Appendix A.

Non-Accelerating vs. Accelerating Flow Results

To account for differing air properties and conditions during each test, the convective heat transfer values were non-dimensionalized using the Stanton numbers; this made for easier comparability between test results. The local Stanton numbers at each thermocouple location for the four surfaces experiencing negligible flow acceleration can be seen in Figure 4.3, while the results for the same surfaces exposed accelerating flow similar to that experienced by a NACA 0012 airfoil are pictured in Figure 4.4. These figures compare the results obtained using both the plastic and the aluminum test surfaces for each of the designated flow condition. The effect of material thermal conductivity on convective heat transfer of the roughness surfaces is evident from this comparison. The Stanton number plots use two flow correlations, one turbulent and one laminar, to display the expected results if the test were performed on a completely smooth surface; these correlations were discussed in chapter 2. Comparing the results of Figures 4.3 and 4.4 shows the difference in convective heat transfer due to surface material. Both figures show that for all cases, the aluminum surfaces produce higher Stanton numbers than the plastic surfaces. In the cases experiencing flow with negligible acceleration the Stanton number increase seen when using aluminum test panels was up to 232% when compared to the plastic results. Additionally, the increase for aluminum surfaces experiencing accelerating flow was up to 160% relative to the plastic results. The use of the high conductivity material provides insight to the convective heat transfer resulting from the liquid layer covering the glaze ice. The liquid

layer results from a phase change occurring in the surface of a glaze ice accretion and has a very high thermal conductivity. The plastic surface Stanton number results are expected to be lower than those of the aluminum surfaces due to the higher thermal resistance of plastic. The comparison of the Figures 4.3 and 4.4 shows that the addition of the ceiling insert induces accelerating flow conditions and generally lowers the local Stanton number values because of increased Reynolds numbers along the surface. Accelerating the flow over the surface provides heat transfer results more representative of those seen over an ice accretion on a real airfoil. While the heat transfer is increases with accelerating flow, the local Stanton numbers decrease by as much as 33% for the same roughness surfaces exposed to accelerated flow when compared to negligible flow acceleration. The increase in heat transfer with accelerating flow is overshadowed by the increase in Reynolds number due to the flow acceleration.

Figure 4.5 compares the Stanton number results for all the plastic surfaces and all the aluminum surfaces for the negligible acceleration and accelerating flow cases. For each test, the first column of panels on the test plate was kept constant. These were smooth panels made from plastic, and were used as a control for each test. Since those panels did not change throughout the study, the first three local Stanton numbers should be the same for every test, within the calculated uncertainty. The drastic difference in Stanton numbers seen in Figures 4.5(c) and 4.5(d) at the fourth and fifth thermocouple locations are a result of the differing smooth-to-rough transition locations. A possible cause of this Stanton number difference is the flow transition from laminar to turbulent, which occurs at the smooth-to-rough transition. Flow transition generally causes higher convective heat transfer values. The surfaces that have an earlier transition to roughness

produce higher Stanton number values at these thermocouple locations. Once the roughness and flow transitions occur, the results from all surfaces follow expected trends with larger roughness heights resulting in larger Stanton number values. The issues caused by differing smooth-to-rough transition locations could potentially be resolved by recreating the surfaces to have the same geometries, but have roughness transitions that all begin at the same location.

Surfaces incorporating larger roughness heights were expected to produce greater heat transfer enhancement than those with smaller roughness elements. Based on the results of Figures 4.5, this expectation proved true for all cases except the aluminum surfaces that were exposed to accelerating flow conditions (Figure 4.5 (d)). The aluminum surfaces experiencing accelerating flow conditions are expected to behave most like real ice accretions on airfoils. The differing smooth-to-rough transition locations of the four surfaces make a trend difficult to discern until the roughness has fully developed and begun to decay on all the surfaces, which occurs at surface panel 3 and 4. The Stanton number values for the surfaces at these panel locations show that greater roughness height results in greater convective heat transfer. The overlap of the uncertainty bars of Figure 4.5 (d) show a difference in convective heat transfer enhancement that is not as substantial as expected. These results suggest that the convective heat transfer is not as sensitive to changes in roughness height as the skin friction coefficient. These observations provide reasoning for the similarities between experimental measurements and the predictions of LEWICE, even using its simplistic sand-grain roughness model with a single roughness height that does not evolve with

time. The surfaces in the legend of the Figure 4.5 have been arranged in order of increasing accretion time, and hence in order of roughness size.

Figures 4.6 and 4.7 present the convection coefficient contour maps from the IR camera recordings when all four surfaces experienced flow with negligible acceleration. Figure 4.6 shows the results for the four plastic surfaces and Figure 4.7 shows the results for the four aluminum surfaces. Similarly, Figures 4.8 and 4.9 show the convection coefficient contour maps for all four surfaces made from plastic and aluminum, respectively, experiencing accelerating flow conditions. These contour maps also make the later roughness transition for the 113012.04 and 113012.05 evident. The aluminum surface results seen in Figures 4.7 and 4.9 best show the influence of the earlier roughness transition on the convective heat transfer. These four figures show the amount of higher convective heat transfer values (the darker red area) increasing with both the flow acceleration and larger roughness elements. The center of the fourth surface panel for the 112912.06 surface appears to be in a relatively large valley that does not include many roughness elements. A valley like this could cause the Stanton number results to be skewed lower for that particular panel made from either material due to the thermocouple measurement for that panel being taken where very little roughness is present. The local convection coefficients calculated at each thermocouple location for each surface and material and flow condition have been compounded and can be seen in Table 4.1.

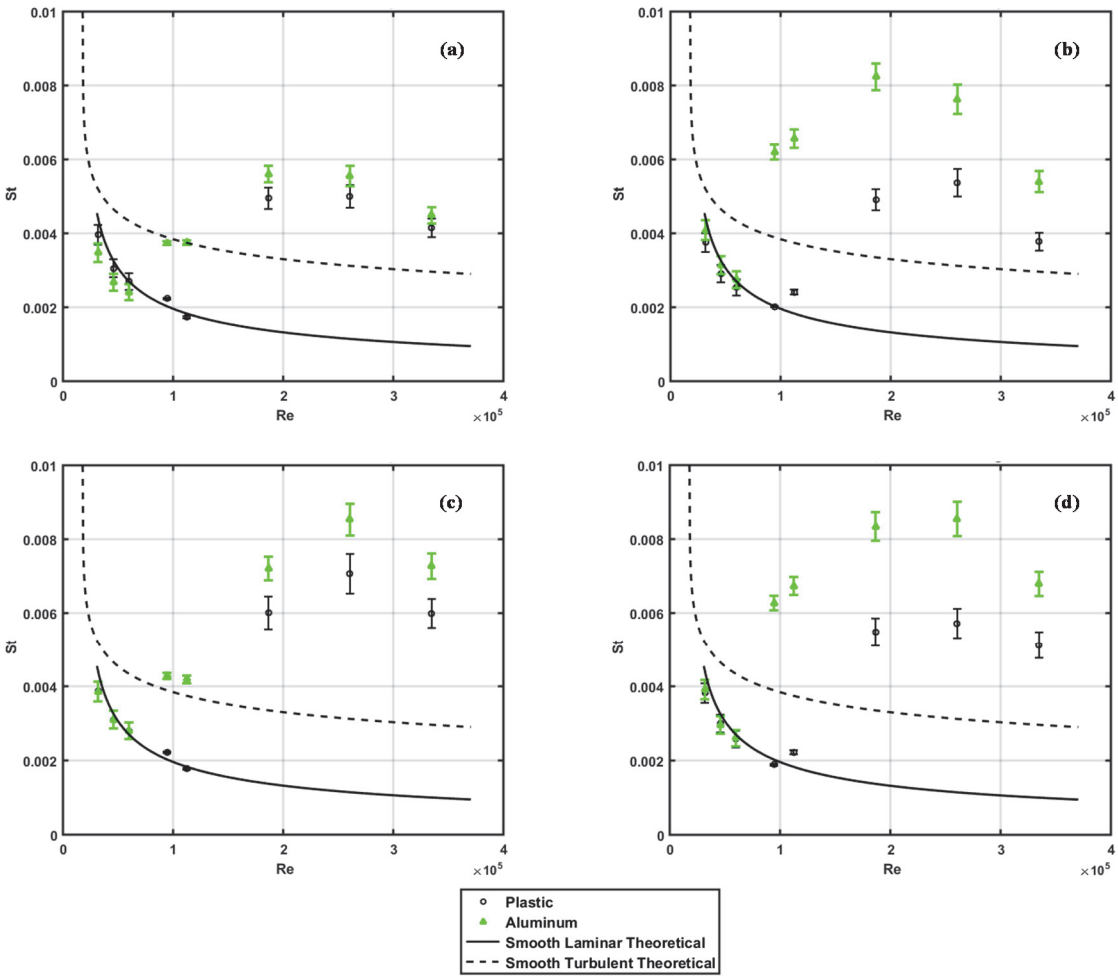

Figure 4.3: Plastic vs. Aluminum Stanton Number Plot for Negligible Flow Acceleration over Surface (a) 113012.05, (b) 112912.02, (c) 113012.04 [12], (d) 112912.06

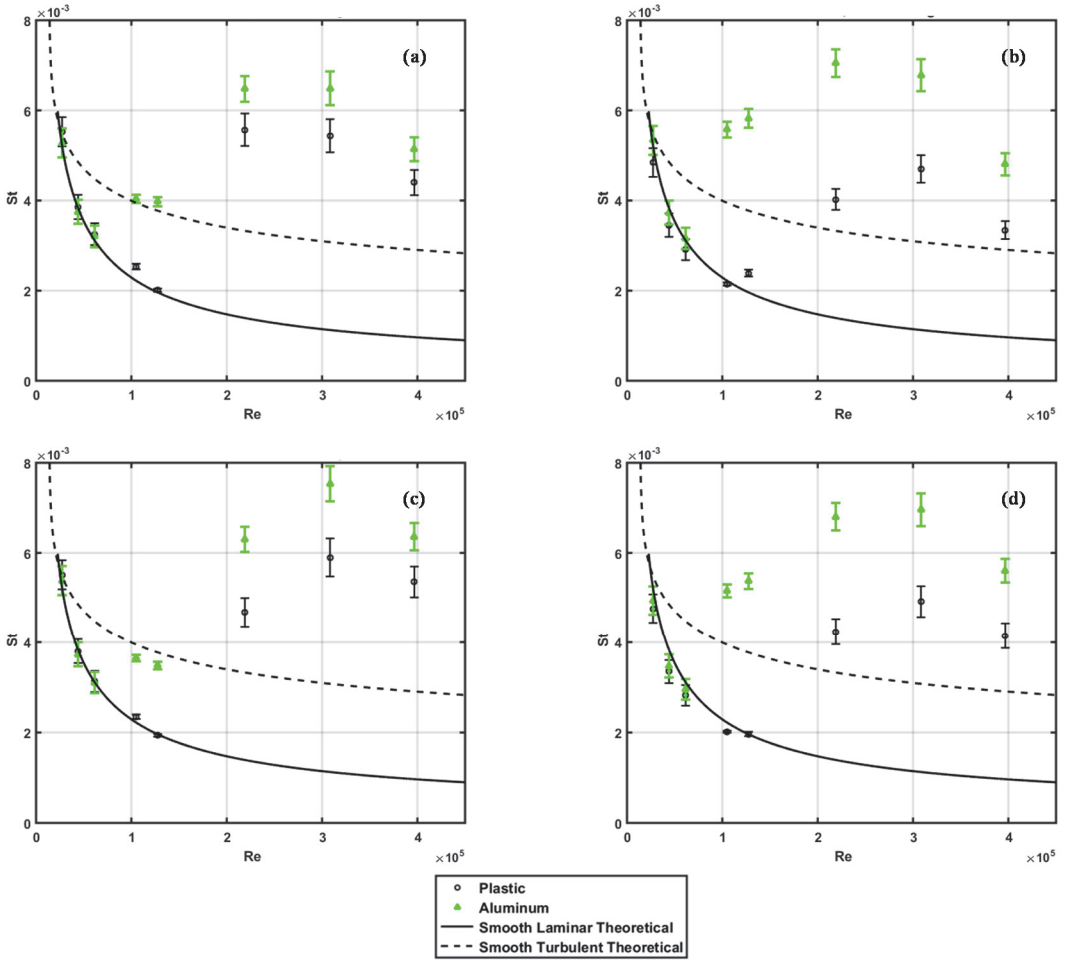

Figure 4.4: Plastic vs. Aluminum Stanton Number Plot for Accelerated Flow over Surface (a) 113012.05, (b) 112912.02, (c) 113012.04 [12], (d) 112912.06

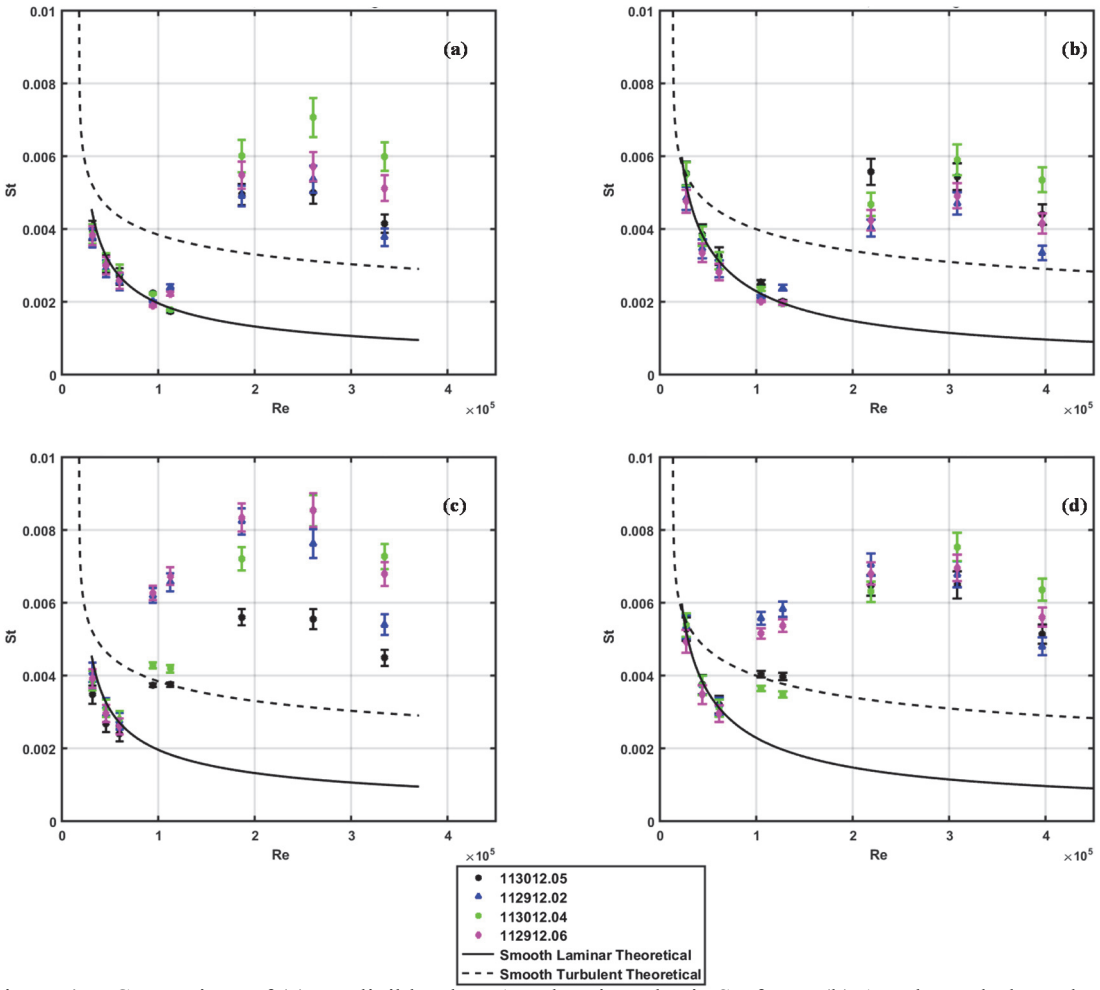

Figure 4.5: Comparison of (a) Negligible Flow Acceleration Plastic Surfaces, (b) Accelerated Flow Plastic Surfaces, (c) Negligible Flow Acceleration Aluminum Surfaces, (d) Accelerated Flow Aluminum Surfaces

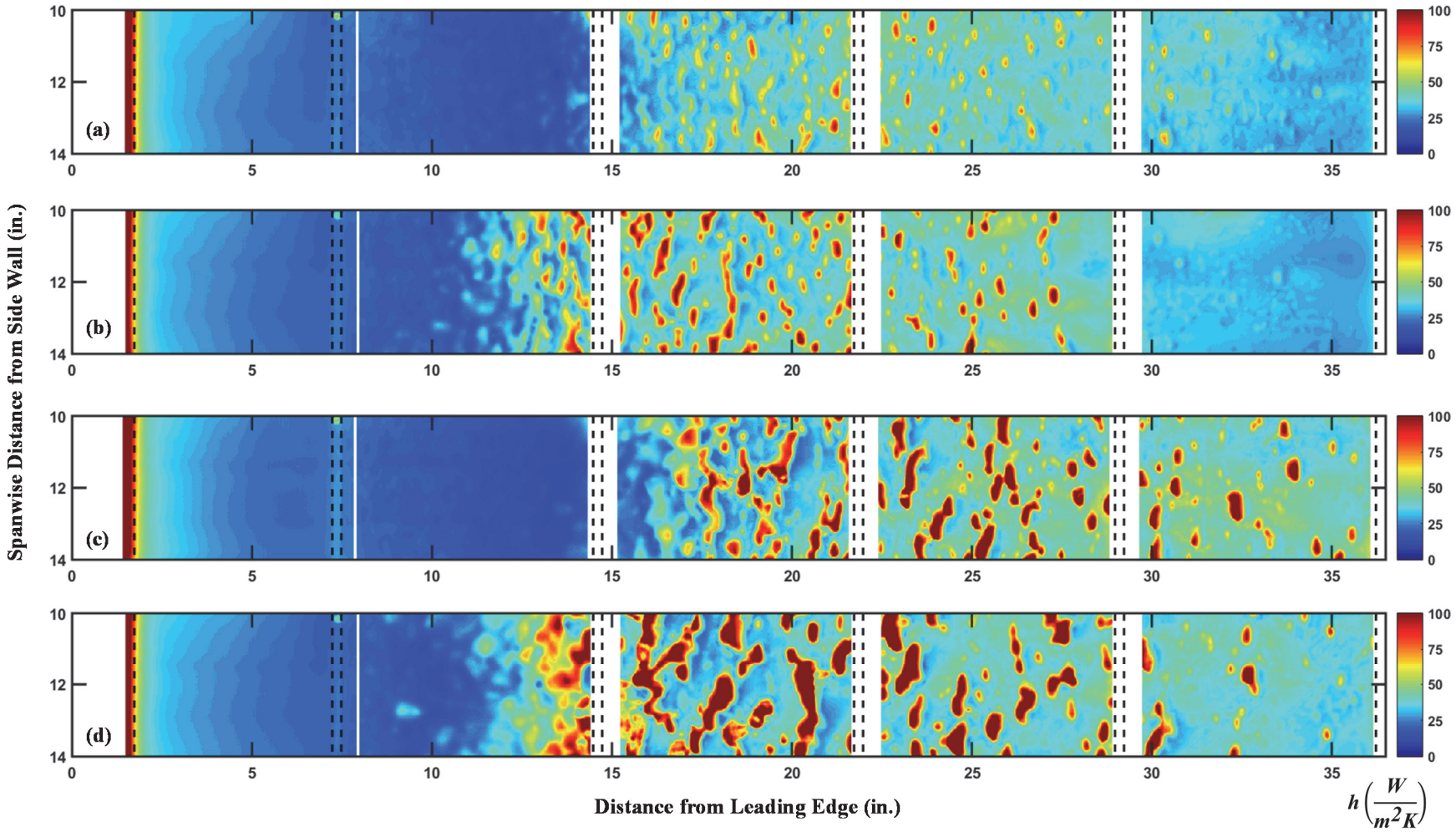

Figure 4.6: Convective Heat Transfer Coefficient Distribution Non-Accelerating Flow over Plastic Surfaces (a) 113012.05, (b) 112912.02, (c) 113012.04, (d) 112912.06

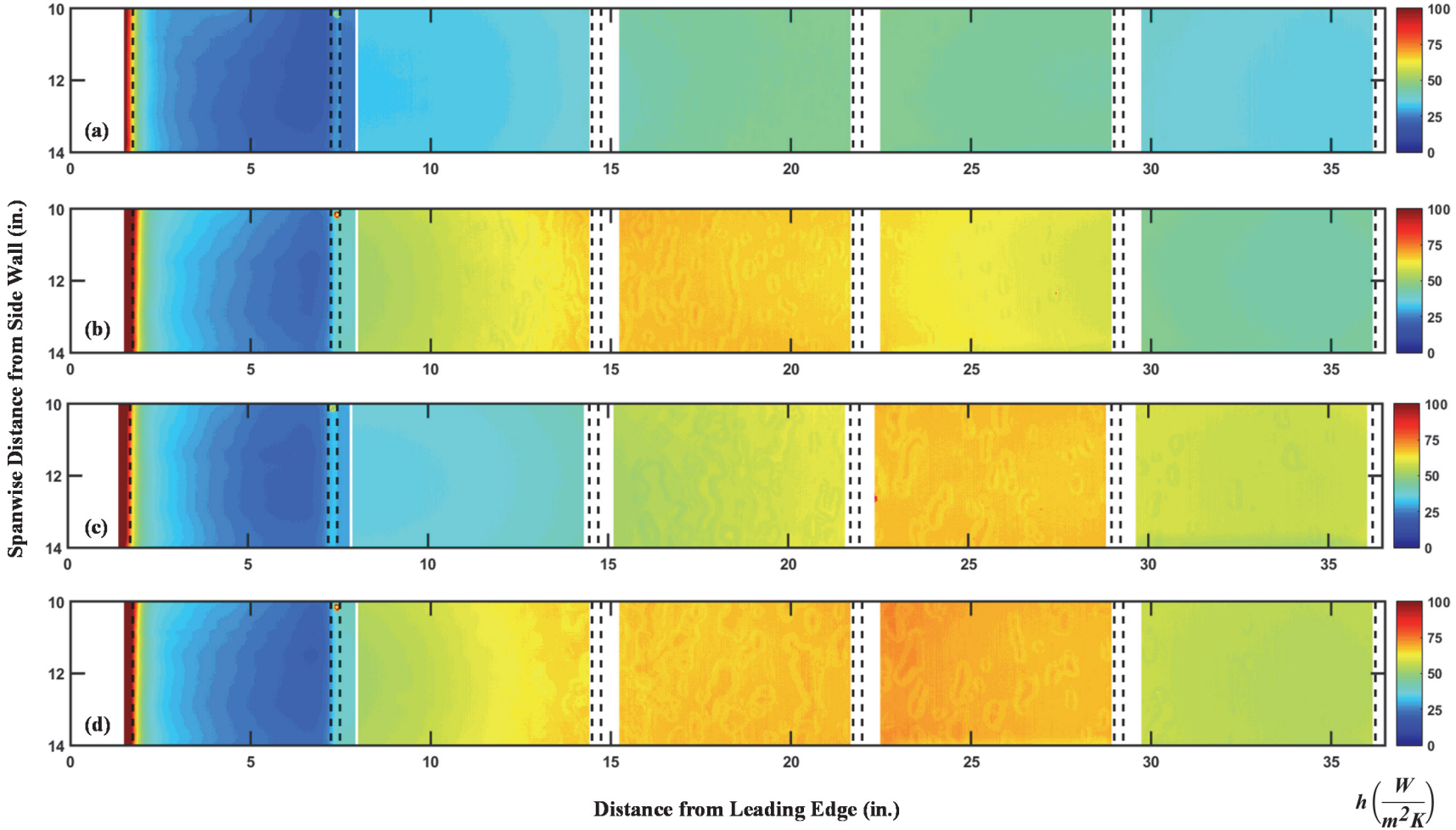

Figure 4.7: Convective Heat Transfer Coefficient Distribution Non-Accelerating Flow over Aluminum Surfaces (a) 113012.05, (b) 112912.02, (c) 113012.04, (d) 112912.06

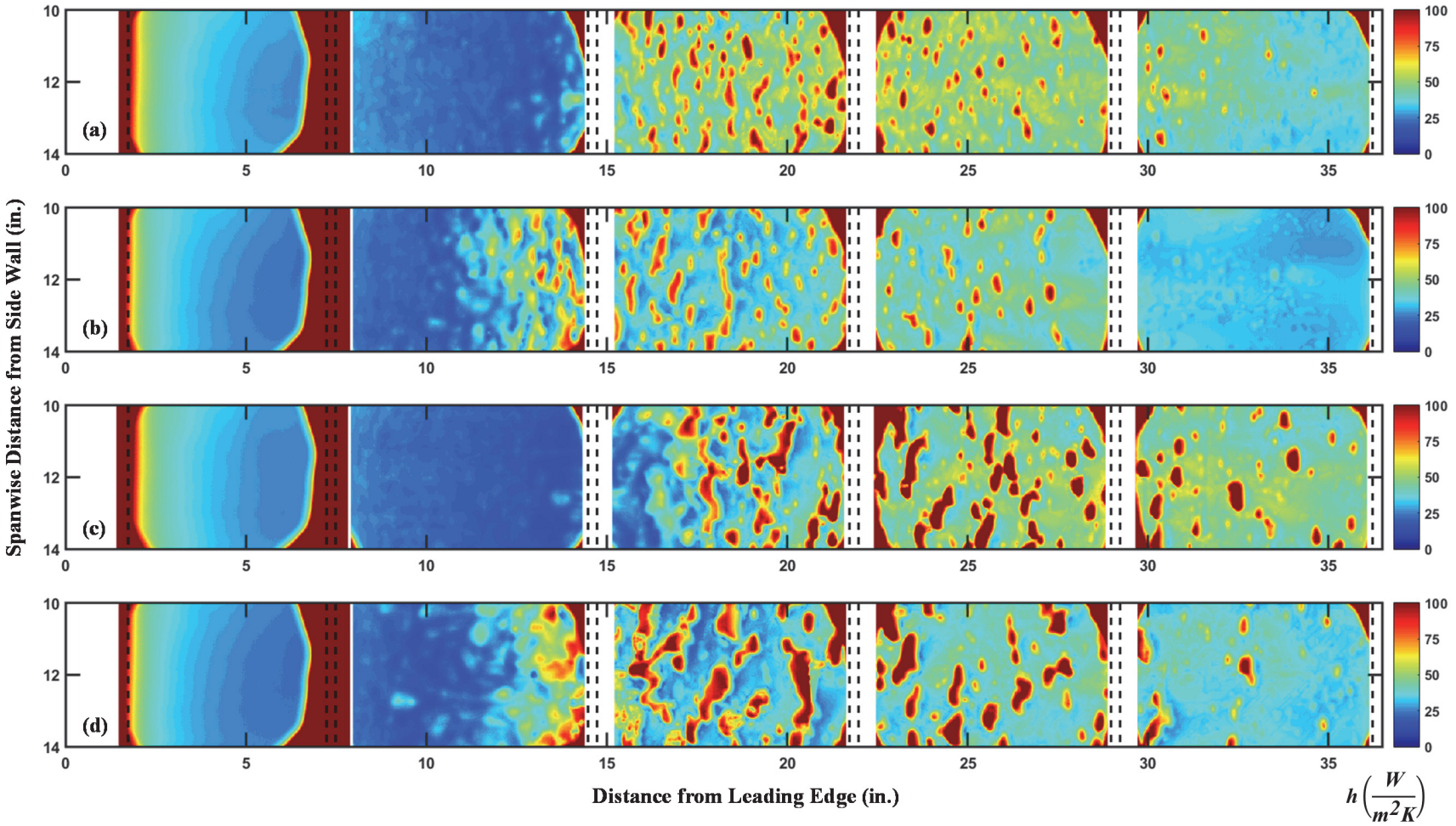

Figure 4.8: Convective Heat Transfer Coefficient Distribution Accelerating Flow over Plastic Surfaces (a) 113012.05, (b) 112912.02, (c) 113012.04, (d) 112912.06

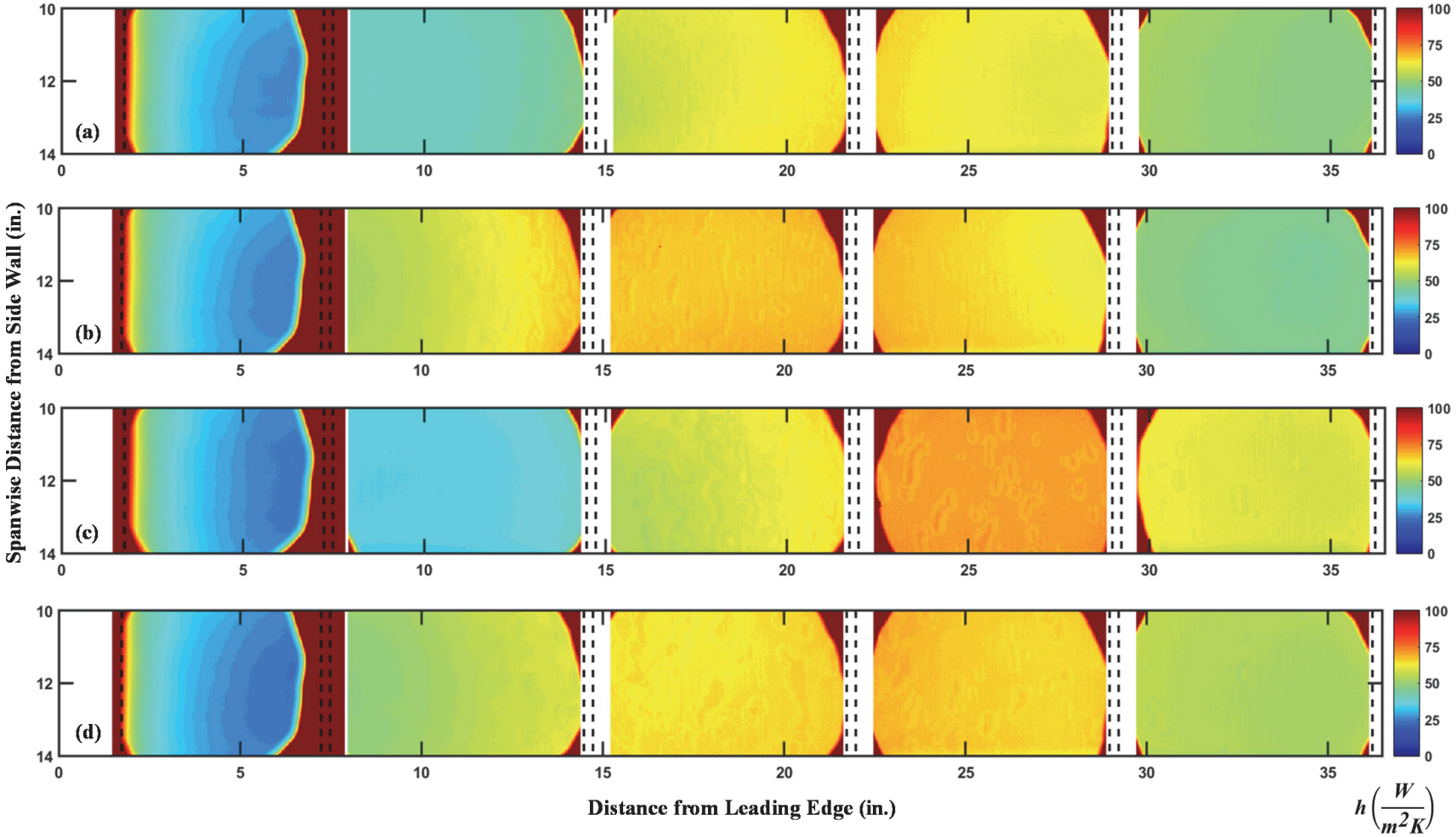

Figure 4.9: Convective Heat Transfer Coefficient Distribution Accelerating Flow over Aluminum Surfaces (a) 113012.05, (b) 112912.02, (c) 113012.04, (d) 112912.06

Table 4.1: Convective Heat Transfer Coefficient Results for all Surfaces experiencing both Flow Conditions

Case	0a	0b	0c	1a	1b	2	3	4
113012.05_RealIce								
Non-Accelerated								
Plastic	31.49 ± 2.12	24.55 ± 1.95	21.60 ± 1.83	18.02 ± 0.19	14.01 ± 0.24	40.20 ± 2.37	41.34 ± 2.56	32.78 ± 1.98
Aluminum	27.52 ± 2.00	21.43 ± 1.83	19.10 ± 1.72	29.87 ± 0.40	29.96 ± 0.50	44.84 ± 1.79	44.40 ± 2.21	35.86 ± 1.78
Accelerated								
Plastic	37.42 ± 2.21	29.42 ± 2.07	26.28 ± 1.97	22.59 ± 0.57	18.36 ± 0.36	53.79 ± 3.53	53.62 ± 3.72	41.42 ± 2.63
Aluminum	35.82 ± 2.20	28.65 ± 2.04	26.04 ± 1.97	35.93 ± 0.81	36.05 ± 0.91	60.87 ± 2.67	61.46 ± 3.53	48.67 ± 2.51
112912.02_RealIce								
Non-Accelerated								
Plastic	30.32 ± 2.08	23.65 ± 1.90	20.63 ± 1.79	16.57 ± 0.16	19.43 ± 0.57	42.59 ± 2.55	46.98 ± 3.41	30.51 ± 1.95
Aluminum	32.62 ± 2.14	25.25 ± 1.96	21.81 ± 1.82	49.79 ± 1.63	52.75 ± 1.99	66.08 ± 2.89	61.37 ± 3.19	43.42 ± 2.28
Accelerated								
Plastic	32.98 ± 2.18	26.48 ± 1.99	23.50 ± 1.89	19.35 ± 0.35	21.90 ± 0.74	40.70 ± 2.38	48.71 ± 3.35	32.08 ± 1.90
Aluminum	36.41 ± 2.20	28.69 ± 2.04	25.61 ± 1.93	49.72 ± 1.56	53.13 ± 1.91	66.39 ± 2.89	64.54 ± 3.38	45.73 ± 2.34
113012.04_RealIce								
Non-Accelerated								
Plastic	30.37 ± 2.10	24.31 ± 1.88	21.88 ± 1.77	17.67 ± 0.21	13.99 ± 0.20	47.32 ± 3.51	55.67 ± 4.23	47.21 ± 3.09
Aluminum	30.06 ± 2.08	24.23 ± 1.87	21.64 ± 1.74	33.39 ± 0.64	32.64 ± 0.81	56.64 ± 2.50	66.64 ± 3.36	56.81 ± 2.69
Accelerated								
Plastic	37.04 ± 2.20	29.05 ± 2.03	25.33 ± 1.91	20.92 ± 0.45	17.62 ± 0.28	46.91 ± 3.34	57.77 ± 4.25	53.54 ± 3.51
Aluminum	36.04 ± 2.18	28.37 ± 2.03	24.90 ± 1.90	32.05 ± 0.64	31.22 ± 0.75	58.69 ± 2.61	70.56 ± 3.65	59.68 ± 2.84
112912.06_RealIce								
Non-Accelerated								
Plastic	30.58 ± 2.10	24.09 ± 1.93	20.79 ± 1.80	14.85 ± 0.22	16.47 ± 0.34	48.64 ± 3.50	41.41 ± 2.69	44.85 ± 3.21
Aluminum	31.15 ± 2.09	23.75 ± 1.89	20.68 ± 1.76	50.16 ± 1.57	54.00 ± 1.96	67.01 ± 3.11	68.81 ± 3.74	54.43 ± 2.62
Accelerated								
Plastic	32.35 ± 2.16	25.66 ± 1.96	22.88 ± 1.87	17.79 ± 0.20	16.76 ± 0.33	45.16 ± 3.22	42.58 ± 2.81	43.02 ± 3.00
Aluminum	33.50 ± 2.16	26.53 ± 1.96	23.79 ± 1.86	45.69 ± 1.26	48.66 ± 1.57	63.90 ± 2.87	65.90 ± 3.45	53.03 ± 2.49

Velocity Boundary Layer Traces

Figures 4.10 - 4.13 depict the results of the velocity boundary layer tests performed on each surface experiencing flow with negligible acceleration and accelerating flow induced by a wind tunnel ceiling insert. For each of these figures the left side plot presents the negligible flow acceleration results, while the right side presents the accelerating flow results.

The boundary layers for the negligible acceleration cases developed as expected with growth as the flow progressed along the test plate. The variation of the freestream velocities from surface to surface can be seen in the figures as well. The accelerated flow cases generally developed as expected, but a few disturbances in the development can be seen. These are particularly evident in Figures 4.10(b) and 4.11 (b). The flow disturbances are suspected to be caused by the interaction of the roughness elements with the boundary layer. Most disturbances are seen in sections 1 and 2 of the roughness plates, where the greatest amounts of roughness are typically present, while none were evident in the other tests of the surfaces due to the negligible acceleration of the flow over the surfaces. The air flow is not forced to interact with the surface as much in non-accelerating flow. The accelerating flow cases can also be seen to produce higher velocity readings than those with negligible acceleration.

Some of the velocity profiles shown in the figures appear to begin at a higher elevation than others. The reason for this is the roughness element placement with respect to the hotwire probe measurement location. The measurements for each profile were taken as close to the test reference surface as possible without damaging the probe. In the 112912.06 case, the velocity measurements for section 2 are seemingly constant within

one half inch vertical distance from the test surface. The reasoning for this is that the measurements were taken beginning directly behind a large roughness element, in a region of recirculation. When comparing the velocity measurements from all four surfaces, it can noted that the boundary layer height increases with increasing roughness height, this was expected based on the results of previous studies.

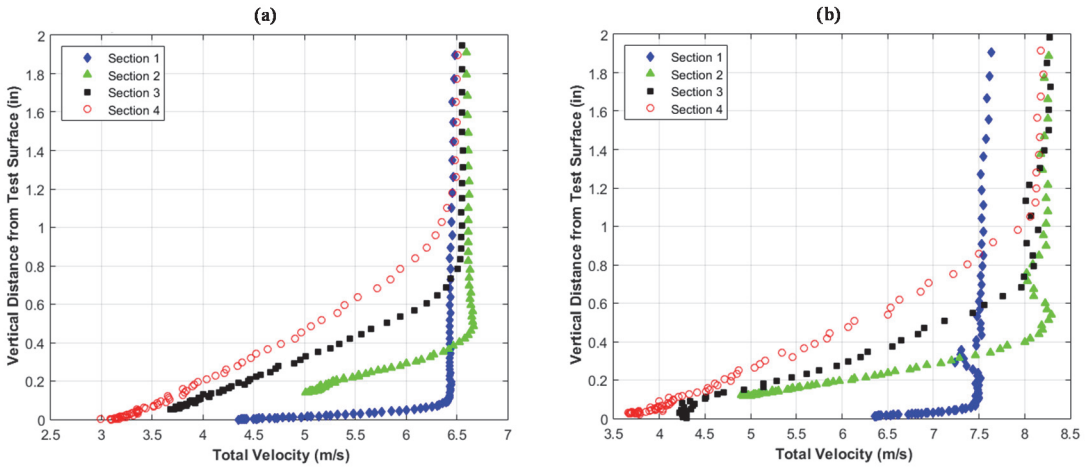

Figure 4.10: Velocity Profiles at Center of each 113012.05 Test Panel for (a) Non-Accelerating Flow, (b) Accelerating Flow

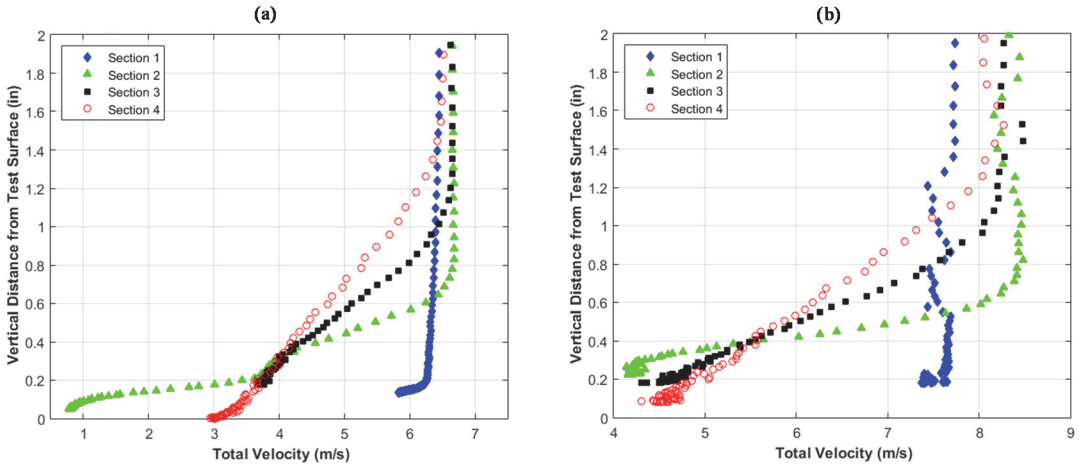

Figure 4.11: Velocity Profiles at Center of each 112912.02 Test Panel for (a) Non-Accelerating Flow, (b) Accelerating Flow

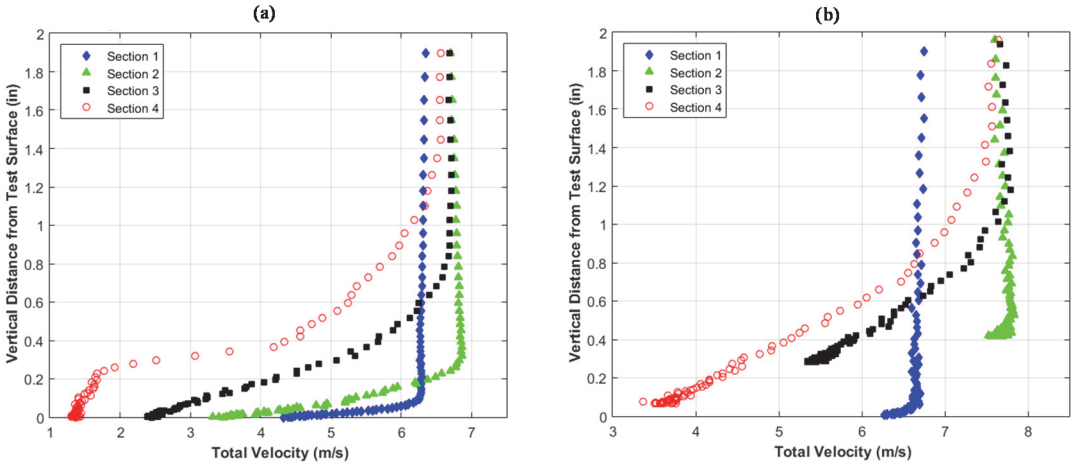

Figure 4.12: Velocity Profiles at Center of each 113012.04 Test Panel for (a) Non-Accelerating Flow [12], (b) Accelerating Flow [12]

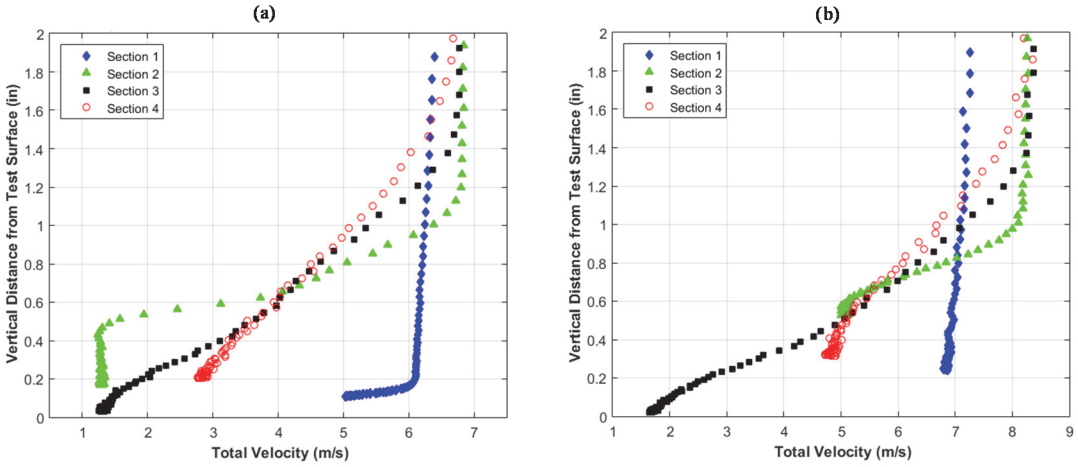

Figure 4.13: Velocity Profiles at Center of each 112912.06 Test Panel for (a) Non-Accelerating Flow, (b) Accelerating Flow

CHAPTER FIVE

Conclusions

Summary of Work

This thesis presented a series of experiments on four surfaces fabricated from laser scans of ice accretions formed in the IRT. These four surfaces form a temporal progression of ice roughness evolution with increasing supercooled cloud exposure time. The study investigated the effect of increasing exposure time on the convective heat transfer of ice roughened surfaces. Each of the surfaces was fabricated from both plastic and aluminum to study the effect of differing thermal conductivity on the convective heat transfer capabilities. All four surfaces were tested in flow with negligible freestream acceleration due to wind tunnel friction and accelerating flow similar to that experienced by a NACA 0012 airfoil to investigate the effect of freestream acceleration on the convective heat transfer of the roughness. The primary findings of this study were:

- For accelerating flow over aluminum roughness panels, the convective heat transfer is not as substantially influenced by increasing roughness heights associated with increasing supercooled cloud exposure time. This explains why LEWICE's is able to predict similar ice formations to those achieved experimentally even when using a sand-grain equivalent roughness height that does no evolve in time.
- Even when exposed to similar cloud conditions there is potential for significant variability in the roughness surfaces, especially in the location of the smooth-to-

rough-transition. There will always be statistical uncertainty due to the stochastic nature of ice accretion formation.

- A smooth-to-rough transition closer to the leading edge results in greater convective heat transfer for the accelerating flow cases. A possible explanation for this is that the flow is transitioning at the smooth-to-rough transition location. Turbulence caused by flow transition typically results in increased convection over a surface.
- The use of a material with a higher thermal conductivity results in an increase in the measured convective heat transfer of the roughness surfaces. In cases where the surface roughness, location on the surface, and flow conditions were similar, the Stanton numbers values were seen to increase by up to 232% with the use of aluminum instead of plastic for the surface material. The increased thermal conductivity materials better model the high conductivity of the liquid layer covering glaze ice accretions.

Future Work

Future works will continue collecting data on real ice accretions as well as attempting to model the heat transfer of real ice accretions. The results of the current study and the future works will be used to aid in the improvement of the ice accretion prediction heat transfer prediction capabilities of LEWICE. The process of improving LEWICE will be continued by 1) attempting to replicate the convective heat transfer results of the real ice surface using a new analog modeling method, 2) collecting detailed skin friction coefficient data along the roughness surfaces, and 3) performing heat transfer measurements on the same real ice roughness surfaces experiencing higher

velocities to scale the Reynolds number over the surface. The data collected from these studies, along with heat transfer data gathered in this study and previous studies also included on this research grant, will be used to build a correlation for the prediction of ice formation. The correlation will then be used to improve the characterization of convective heat transfer enhancement in LEWICE.

APPENDIX

APPENDIX A

Test Data

This appendix provides the test data for the all of the 113012.05, 112912.02, 113012.04, and 112912.06 convective heat transfer tests.

Table A.1: Non-Accelerated 113012.05 Plastic

Parameter	0a	0b	0c	1a	1b	2	3	4
x (in)	3.10	4.48	5.85	9.23	10.98	18.23	25.48	32.73
A_t (in^2)	35.06	35.06	35.06	44.62	44.62	44.62	44.62	44.62
ε	0.95	0.95	0.95	0.95	0.95	0.95	0.95	0.95
σ (W/m^2K^4)	5.67e-8	5.67e-8	5.67e-8	5.67e-8	5.67e-8	5.67e-8	5.67e-8	5.67e-8
t_p (in)	0.72	0.72	0.72	0.72	0.72	0.72	0.72	0.72
C_k	0.90	0.90	0.90	0.90	0.90	1.05	1.10	1.05
E (V)	6.07	6.07	6.07	5.92	5.92	5.96	6.33	6.24
I (A)	2.06	2.06	2.06	2.62	2.62	2.57	2.70	2.60
k_p (W/mK)	0.205	0.205	0.205	0.205	0.205	0.205	0.205	0.205
T_{SS} (K)	315.91	316.47	317.57	318.30	320.97	315.46	315.39	317.37
T_{UP} (K)	300.31	297.54	298.49	299.54	300.01	300.17	300.62	301.12
T_∞ (K)	294.18	294.18	294.18	294.18	294.18	294.18	294.18	294.18
T_{IR} (K)	304.69	306.07	307.26	308.87	310.70	301.96	303.15	303.70
h (W/m^2K)	31.49 ± 2.12	24.55 ± 1.95	21.60 ± 1.83	18.02 ± 0.19	14.01 ± 0.24	40.20 ± 2.37	41.34 ± 2.56	32.78 ± 1.98

Table A.2: Non-Accelerated 113012.05 Aluminum

Parameter	0a	0b	0c	1a	1b	2	3	4
x (in)	3.10	4.48	5.85	9.23	10.98	18.23	25.48	32.73
A_t (in^2)	35.06	35.06	35.06	44.62	44.62	44.62	44.62	44.62
ε	0.95	0.95	0.95	0.95	0.95	0.95	0.95	0.95
σ (W/m^2K^4)	5.67E-08	5.67E-08	5.67E-08	5.67E-08	5.67E-08	5.67E-08	5.67E-08	5.67E-08
t_p (in)	0.72	0.72	0.72	0.72	0.72	0.72	0.72	0.72
C_k	0.90	0.90	0.90	0.90	0.90	1.05	1.10	1.05
E (V)	6.06	6.09	6.09	5.86	5.86	5.97	6.20	6.09
I (A)	2.04	2.04	2.04	2.64	2.64	2.58	2.76	2.58
k_p (W/mK)	0.205	0.205	0.205	0.205	0.205	0.205	0.205	0.205
T_{SS} (K)	316.13	316.44	317.25	308.43	309.17	306.21	309.68	309.93
T_{UP} (K)	300.56	297.21	298.09	297.44	297.52	297.44	298.41	298.71
T_∞ (K)	293.06	293.06	293.06	293.06	293.06	293.06	293.06	293.06
T_{IR} (K)	304.77	306.02	307.25	305.04	304.83	301.62	302.18	303.03
h (W/m^2K)	27.52 ± 2.00	21.43 ± 1.83	19.10 ± 1.72	29.87± 0.40	29.96 ± 0.50	44.84 ± 1.79	44.40 ± 2.21	35.86 ± 1.78

Table A.3: Non-Accelerated 112912.02 Plastic

Parameter	0a	0b	0c	1a	1b	2	3	4
x (in)	3.10	4.48	5.85	9.23	10.98	18.23	25.48	32.73
A_t (in^2)	35.06	35.06	35.06	44.62	44.62	44.62	44.62	44.62
ε	0.95	0.95	0.95	0.95	0.95	0.95	0.95	0.95
σ (W/m^2K^4)	5.67E-08	5.67E-08	5.67E-08	5.67E-08	5.67E-08	5.67E-08	5.67E-08	5.67E-08
t_p (in)	0.72	0.72	0.72	0.72	0.72	0.72	0.72	0.72
C_k	0.90	0.90	0.90	0.90	0.90	1.05	1.10	1.05
E (V)	6.01	6.01	6.01	5.90	5.90	6.05	6.25	6.08
I (A)	2.07	2.07	2.07	2.64	2.64	2.54	2.72	2.59
k_p (W/mK)	0.205	0.205	0.205	0.205	0.205	0.205	0.205	0.205
T_{SS} (K)	317.20	318.33	319.23	320.46	322.11	315.17	317.22	318.34
T_{UP} (K)	301.06	298.99	299.47	300.25	300.61	300.41	301.35	301.70
T_∞ (K)	295.21	295.21	295.21	295.21	295.21	295.21	295.21	295.21
T_{IR} (K)	305.94	307.26	308.45	310.14	307.97	302.66	302.71	304.84
h (W/m^2K)	30.32 ± 2.08	23.65 ± 1.90	20.63 ± 1.79	16.57 ± 0.16	19.43 ± 0.57	42.59 ± 2.55	46.98 ± 3.41	30.51 ± 1.95

Table A.4: Non-Accelerated 112912.02 Aluminum

Parameter	0a	0b	0c	1a	1b	2	3	4
x (in)	3.10	4.48	5.85	9.23	10.98	18.23	25.48	32.73
A_t (in^2)	35.06	35.06	35.06	44.62	44.62	44.62	44.62	44.62
ε	0.95	0.95	0.95	0.95	0.95	0.95	0.95	0.95
σ (W/m^2K^4)	5.67E-08	5.67E-08	5.67E-08	5.67E-08	5.67E-08	5.67E-08	5.67E-08	5.67E-08
t_p (in)	0.72	0.72	0.72	0.72	0.72	0.72	0.72	0.72
C_k	0.90	0.90	0.90	0.90	0.90	1.05	1.10	1.05
E (V)	5.99	5.99	5.99	5.84	5.84	6.06	6.23	6.05
I (A)	2.06	2.06	2.06	2.64	2.64	2.52	2.74	2.58
k_p (W/mK)	0.205	0.205	0.205	0.205	0.205	0.205	0.205	0.205
T_{SS} (K)	316.67	317.47	317.96	307.66	308.18	305.75	308.16	311.04
T_{UP} (K)	300.94	299.12	299.49	298.27	298.26	298.22	298.94	299.70
T_∞ (K)	295.68	295.68	295.68	295.68	295.68	295.68	295.68	295.68
T_{IR} (K)	305.73	307.25	308.62	303.63	303.14	301.83	302.81	303.97
h (W/m^2K)	32.62 ± 2.14	25.25 ± 1.96	21.81 ± 1.82	49.79 ± 1.63	52.75 ± 1.99	66.08 ± 2.89	61.37 ± 3.19	43.42 ± 2.28

Table A.5: Non-Accelerated 113012.04 Plastic [12]

Parameter	0a	0b	0c	1a	1b	2	3	4
x (in)	3.10	4.48	5.85	9.23	10.98	18.23	25.48	32.73
A_t (in^2)	35.06	35.06	35.06	44.62	44.62	44.62	44.62	44.62
ε	0.95	0.95	0.95	0.95	0.95	0.95	0.95	0.95
σ (W/m^2K^4)	5.67e-8	5.67e-8	5.67e-8	5.67e-8	5.67e-8	5.67e-8	5.67e-8	5.67e-8
t_p (in)	0.72	0.72	0.72	0.72	0.72	0.72	0.72	0.72
C_k	0.90	0.90	0.90	0.90	0.90	1.05	1.10	1.05
E (V)	5.98	5.98	5.98	5.89	5.89	5.86	6.26	6.18
I (A)	2.06	2.06	2.06	2.61	2.61	2.60	2.72	2.55
k_p (W/mK)	0.205	0.205	0.205	0.205	0.205	0.205	0.205	0.205
T_{SS} (K)	316.92	317.24	318.03	320.02	322.27	318.31	316.40	316.26
T_{UP} (K)	300.12	300.53	301.23	301.00	300.98	301.50	301.59	301.50
T_∞ (K)	295.45	295.45	295.45	295.45	295.45	295.45	295.45	295.45
T_{IR} (K)	305.83	307.92	308.96	309.92	311.40	301.69	302.10	302.52
h (W/m^2K)	30.37 ± 2.10	24.31 ± 1.88	21.88 ± 1.77	17.67 ± 0.21	13.99 ± 0.20	47.32 ± 3.51	55.67 ± 4.23	47.21 ± 3.09

Table A.6: Non-Accelerated 113012.04 Aluminum [12]

Parameter	0a	0b	0c	1a	1b	2	3	4
x (in)	3.10	4.48	5.85	9.23	10.98	18.23	25.48	32.73
A_t (in^2)	35.06	35.06	35.06	44.62	44.62	44.62	44.62	44.62
ε	0.95	0.95	0.95	0.95	0.95	0.95	0.95	0.95
σ (W/m^2K^4)	5.67E-08	5.67E-08	5.67E-08	5.67E-08	5.67E-08	5.67E-08	5.67E-08	5.67E-08
t_p (in)	0.72	0.72	0.72	0.72	0.72	0.72	0.72	0.72
C_k	0.90	0.90	0.90	0.90	0.90	1.05	1.10	1.05
E (V)	6.00	6.00	6.00	5.87	5.87	5.85	6.20	6.09
I (A)	2.06	2.06	2.06	2.65	2.65	2.60	2.75	2.61
k_p (W/mK)	0.205	0.205	0.205	0.205	0.205	0.205	0.205	0.205
T_{SS} (K)	316.84	317.13	317.47	309.97	311.61	307.31	306.95	307.32
T_{UP} (K)	300.13	300.51	301.10	299.10	299.05	298.54	298.71	298.77
T_∞ (K)	295.09	295.09	295.09	295.09	295.09	295.09	295.09	295.09
T_{IR} (K)	305.64	307.69	308.95	306.05	305.83	301.93	301.88	302.29
h (W/m^2K)	30.06 ± 2.08	24.23 ± 1.87	21.64 ± 1.74	33.39 ± 0.64	32.64 ± 0.81	56.46 ± 2.50	66.64 ± 3.36	56.81 ± 2.69

Table A.7: Non-Accelerated 112912.06 Plastic

Parameter	0a	0b	0c	1a	1b	2	3	4
x (in)	3.10	4.48	5.85	9.23	10.98	18.23	25.48	32.73
A_t (in^2)	35.06	35.06	35.06	44.62	44.62	44.62	44.62	44.62
ε	0.95	0.95	0.95	0.95	0.95	0.95	0.95	0.95
σ (W/m^2K^4)	5.67E-08	5.67E-08	5.67E-08	5.67E-08	5.67E-08	5.67E-08	5.67E-08	5.67E-08
t_p (in)	0.72	0.72	0.72	0.72	0.72	0.72	0.72	0.72
C_k	0.90	0.90	0.90	0.90	0.90	1.05	1.10	1.05
E (V)	6.01	6.01	6.01	5.91	5.91	6.07	6.30	6.06
I (A)	2.07	2.07	2.07	2.63	2.63	2.53	2.72	2.55
k_p (W/mK)	0.205	0.205	0.205	0.205	0.205	0.205	0.205	0.205
T_{SS} (K)	316.88	318.15	319.12	320.58	322.57	316.45	316.29	316.90
T_{UP} (K)	300.41	299.01	299.38	299.93	300.17	300.35	300.95	301.11
T_∞ (K)	294.81	294.81	294.81	294.81	294.81	294.81	294.81	294.81
T_{IR} (K)	305.33	306.70	307.92	310.70	308.81	301.15	303.39	301.74
h (W/m^2K)	30.58 ± 2.10	24.09 ± 1.93	20.79 ± 1.80	14.85 ± 0.22	16.47 ± 0.34	48.64 ± 3.50	41.41 ± 2.69	44.85 ± 3.21

Table A.8: Non-Accelerated 112912.06 Aluminum

Parameter	0a	0b	0c	1a	1b	2	3	4
x (in)	3.10	4.48	5.85	9.23	10.98	18.23	25.48	32.73
A_t (in^2)	35.06	35.06	35.06	44.62	44.62	44.62	44.62	44.62
ε	0.95	0.95	0.95	0.95	0.95	0.95	0.95	0.95
σ (W/m^2K^4)	5.67E-08	5.67E-08	5.67E-08	5.67E-08	5.67E-08	5.67E-08	5.67E-08	5.67E-08
t_p (in)	0.72	0.72	0.72	0.72	0.72	0.72	0.72	0.72
C_k	0.90	0.90	0.90	0.90	0.90	1.05	1.10	1.05
E (V)	6.01	6.01	6.04	5.86	5.86	5.89	6.23	6.03
I (A)	2.07	2.07	2.07	2.65	2.65	2.60	2.74	2.62
k_p (W/mK)	0.205	0.205	0.205	0.205	0.205	0.205	0.205	0.205
T_{SS} (K)	316.35	316.94	317.63	306.93	307.18	306.34	307.41	307.72
T_{UP} (K)	300.76	298.15	298.81	297.82	297.72	297.92	298.45	298.64
T_∞ (K)	295.00	295.00	295.00	295.00	295.00	295.00	295.00	295.00
T_{IR} (K)	305.62	307.16	308.54	303.00	302.43	300.97	301.48	302.36
h (W/m^2K)	31.15 ± 2.09	23.75 ± 1.89	20.68 ± 1.76	50.16 ± 1.57	54.00 ± 1.96	67.01 ± 3.11	68.81 ± 3.74	54.43 ± 2.62

Table A.9: Accelerated 113012.05 Plastic

Parameter	0a	0b	0c	1a	1b	2	3	4
x (in)	3.10	4.48	5.85	9.23	10.98	18.23	25.48	32.73
A_t (in^2)	35.06	35.06	35.06	44.62	44.62	44.62	44.62	44.62
ε	0.95	0.95	0.95	0.95	0.95	0.95	0.95	0.95
σ (W/m^2K^4)	5.67E-08	5.67E-08	5.67E-08	5.67E-08	5.67E-08	5.67E-08	5.67E-08	5.67E-08
t_p (in)	0.72	0.72	0.72	0.72	0.72	0.72	0.72	0.72
C_k	0.90	0.90	0.90	0.90	0.90	1.05	1.10	1.05
E (V)	6.02	6.02	6.02	5.93	5.93	5.98	6.32	6.15
I (A)	2.07	2.07	2.07	2.61	2.61	2.57	2.71	2.57
k_p (W/mK)	0.205	0.205	0.205	0.205	0.205	0.205	0.205	0.205
T_{SS} (K)	313.40	315.08	316.22	317.18	319.54	314.75	314.78	316.34
T_{UP} (K)	296.92	297.79	298.41	299.20	299.64	299.99	300.47	300.88
T_∞ (K)	295.10	295.10	295.10	295.10	295.10	295.10	295.10	295.10
T_{IR} (K)	303.99	305.77	306.64	307.62	308.98	301.15	302.14	302.90
h (W/m^2K)	37.42 ± 2.21	29.42 ± 2.07	26.28 ± 1.97	22.59 ± 0.57	18.36 ± 0.36	53.79 ± 3.53	53.62 ± 3.72	41.42 ± 2.63

Table A.10: Accelerated 113012.05 Aluminum

Parameter	0a	0b	0c	1a	1b	2	3	4
x (in)	3.10	4.48	5.85	9.23	10.98	18.23	25.48	32.73
A_t (in^2)	35.06	35.06	35.06	44.62	44.62	44.62	44.62	44.62
ε	0.95	0.95	0.95	0.95	0.95	0.95	0.95	0.95
σ (W/m^2K^4)	5.67E-08	5.67E-08	5.67E-08	5.67E-08	5.67E-08	5.67E-08	5.67E-08	5.67E-08
t_p (in)	0.72	0.72	0.72	0.72	0.72	0.72	0.72	0.72
C_k	0.90	0.90	0.90	0.90	0.90	1.05	1.10	1.05
E (V)	6.04	6.04	6.04	5.88	5.88	5.96	6.28	6.15
I (A)	2.06	2.06	2.06	2.64	2.64	2.58	2.73	2.57
k_p (W/mK)	0.205	0.205	0.205	0.205	0.205	0.205	0.205	0.205
T_{SS} (K)	313.17	314.63	315.92	308.51	309.19	305.97	309.31	309.69
T_{UP} (K)	296.64	297.47	298.10	297.73	297.75	297.66	298.63	298.95
T_∞ (K)	249.69	249.69	249.69	249.69	249.69	249.69	249.69	249.69
T_{IR} (K)	303.93	305.65	306.34	305.01	304.82	301.24	301.60	302.47
h (W/m^2K)	35.82 ± 2.20	28.65 ± 2.04	26.04 ± 1.97	35.93 ± 0.81	36.05 ± 0.91	60.87 ± 2.67	61.46 ± 3.53	48.67 ± 2.51

Table A.11: Accelerated 112912.02 Plastic

Parameter	0a	0b	0c	1a	1b	2	3	4
x (in)	3.10	4.48	5.85	9.23	10.98	18.23	25.48	32.73
A_t (in^2)	35.06	35.06	35.06	44.62	44.62	44.62	44.62	44.62
ε	0.95	0.95	0.95	0.95	0.95	0.95	0.95	0.95
σ (W/m^2K^4)	5.67E-08	5.67E-08	5.67E-08	5.67E-08	5.67E-08	5.67E-08	5.67E-08	5.67E-08
t_p (in)	0.72	0.72	0.72	0.72	0.72	0.72	0.72	0.72
C_k	0.90	0.90	0.90	0.90	0.90	1.05	1.10	1.05
E (V)	6.07	6.07	6.07	5.91	5.91	6.00	6.35	6.19
I (A)	2.06	2.06	2.06	2.62	2.62	2.55	2.71	2.54
k_p (W/mK)	0.205	0.205	0.205	0.205	0.205	0.205	0.205	0.205
T_{SS} (K)	313.07	314.68	315.82	317.39	319.71	314.07	314.86	314.95
T_{UP} (K)	296.03	296.87	297.48	298.49	298.91	298.99	299.80	300.00
T_∞ (K)	293.32	293.32	293.32	293.32	293.32	293.32	293.32	293.32
T_{IR} (K)	303.17	304.89	305.88	307.08	305.16	301.08	300.89	303.11
h (W/m^2K)	32.98 ± 2.18	26.48 ± 1.99	23.50 ± 1.89	19.35 ± 0.35	21.90 ± 0.74	40.70 ± 2.38	48.71 ± 3.35	32.08 ± 1.90

Table A.12: Accelerated 112912.02 Aluminum

Parameter	0a	0b	0c	1a	1b	2	3	4
x (in)	3.10	4.48	5.85	9.23	10.98	18.23	25.48	32.73
A_t (in^2)	35.06	35.06	35.06	44.62	44.62	44.62	44.62	44.62
ε	0.95	0.95	0.95	0.95	0.95	0.95	0.95	0.95
σ (W/m^2K^4)	5.67E-08	5.67E-08	5.67E-08	5.67E-08	5.67E-08	5.67E-08	5.67E-08	5.67E-08
t_p (in)	0.72	0.72	0.72	0.72	0.72	0.72	0.72	0.72
C_k	0.90	0.90	0.90	0.90	0.90	1.05	1.10	1.05
E (V)	6.07	6.07	6.07	5.86	5.86	5.93	6.33	6.14
I (A)	2.08	2.08	2.08	2.65	2.65	2.58	2.71	2.58
k_p (W/mK)	0.205	0.205	0.205	0.205	0.205	0.205	0.205	0.205
T_{SS} (K)	313.89	315.18	315.83	306.69	307.14	305.16	307.22	309.97
T_{UP} (K)	296.97	297.79	298.34	297.50	297.58	297.60	298.21	298.98
T_∞ (K)	294.76	294.76	294.76	294.76	294.76	294.76	294.76	294.76
T_{IR} (K)	303.94	305.84	306.88	302.80	302.28	300.90	301.66	302.94
h (W/m^2K)	36.41± 2.20	28.69 ± 2.04	25.61 ± 1.93	49.72 ± 1.56	53.13 ± 1.91	66.39 ± 2.89	64.54 ± 3.38	45.73 ± 2.34

Table A.13: Accelerated 113012.04 Plastic [12]

Parameter	0a	0b	0c	1a	1b	2	3	4
x (in)	3.10	4.48	5.85	9.23	10.98	18.23	25.48	32.73
A_t (in^2)	35.06	35.06	35.06	44.62	44.62	44.62	44.62	44.62
ε	0.95	0.95	0.95	0.95	0.95	0.95	0.95	0.95
σ (W/m^2K^4)	5.67E-08	5.67E-08	5.67E-08	5.67E-08	5.67E-08	5.67E-08	5.67E-08	5.67E-08
t_p (in)	0.72	0.72	0.72	0.72	0.72	0.72	0.72	0.72
C_k	0.90	0.90	0.90	0.90	0.90	1.05	1.10	1.05
E (V)	6.00	6.00	6.00	5.87	5.87	5.88	6.27	6.14
I (A)	2.09	2.09	2.09	2.63	2.63	2.59	2.72	2.57
k_p (W/mK)	0.205	0.205	0.205	0.205	0.205	0.205	0.205	0.205
T_{SS} (K)	314.31	315.30	316.45	317.92	320.03	317.41	315.09	314.67
T_{UP} (K)	297.53	298.31	298.91	299.71	300.23	301.10	300.98	300.83
T_∞ (K)	295.32	295.32	295.32	295.32	295.32	295.32	295.32	295.32
T_{IR} (K)	304.30	306.28	307.40	308.47	309.61	301.73	301.90	301.81
h (W/m^2K)	37.04 ± 2.20	29.05 ± 2.03	25.33 ± 1.91	20.92 ± 0.45	17.62 ± 0.28	46.91 ± 3.34	57.77 ± 4.25	53.54 ± 3.51

Table A.14: Accelerated 113012.04 Aluminum [12]

Parameter	0a	0b	0c	1a	1b	2	3	4
x (in)	3.10	4.48	5.85	9.23	10.98	18.23	25.48	32.73
A_t (in^2)	35.06	35.06	35.06	44.62	44.62	44.62	44.62	44.62
ε	0.95	0.95	0.95	0.95	0.95	0.95	0.95	0.95
σ (W/m^2K^4)	5.67E-08	5.67E-08	5.67E-08	5.67E-08	5.67E-08	5.67E-08	5.67E-08	5.67E-08
t_p (in)	0.72	0.72	0.72	0.72	0.72	0.72	0.72	0.72
C_k	0.90	0.90	0.90	0.90	0.90	1.05	1.10	1.05
E (V)	6.00	6.00	6.00	5.87	5.87	5.87	6.19	6.05
I (A)	2.07	2.07	2.07	2.64	2.64	2.61	2.75	2.60
k_p (W/mK)	0.205	0.205	0.205	0.205	0.205	0.205	0.205	0.205
T_{SS} (K)	314.70	315.69	316.23	310.44	311.91	307.47	307.01	307.37
T_{UP} (K)	297.71	298.56	299.15	298.92	299.05	298.78	298.94	299.11
T_∞ (K)	295.47	295.47	295.47	295.47	295.47	295.47	295.47	295.47
T_{IR} (K)	304.48	306.44	307.67	306.61	306.50	302.15	301.92	302.35
h (W/m^2K)	36.04 ± 2.18	28.37 ± 2.03	24.90 ± 1.90	32.05 ± 0.64	31.22 ± 0.75	58.69 ± 2.61	70.56 ± 3.65	59.68 ± 2.84

Table A.15: Accelerated 112912.06 Plastic

Parameter	0a	0b	0c	1a	1b	2	3	4
x (in)	3.10	4.48	5.85	9.23	10.98	18.23	25.48	32.73
A_t (in^2)	35.06	35.06	35.06	44.62	44.62	44.62	44.62	44.62
ε	0.95	0.95	0.95	0.95	0.95	0.95	0.95	0.95
σ (W/m^2K^4)	5.67E-08	5.67E-08	5.67E-08	5.67E-08	5.67E-08	5.67E-08	5.67E-08	5.67E-08
t_p (in)	0.72	0.72	0.72	0.72	0.72	0.72	0.72	0.72
C_k	0.90	0.90	0.90	0.90	0.90	1.05	1.10	1.05
E (V)	6.03	6.03	6.03	5.94	5.94	6.03	6.37	6.09
I (A)	2.06	2.06	2.06	2.61	2.61	2.55	2.69	2.59
k_p (W/mK)	0.205	0.205	0.205	0.205	0.205	0.205	0.205	0.205
T_{SS} (K)	313.54	315.30	316.63	318.34	321.53	316.71	315.94	317.22
T_{UP} (K)	296.75	297.54	298.15	298.90	299.58	300.04	300.40	300.86
T_∞ (K)	293.85	293.85	293.85	293.85	293.85	293.85	293.85	293.85
T_{IR} (K)	303.83	305.62	306.50	308.28	307.82	300.48	302.23	301.12
h (W/m^2K)	32.35 ± 2.16	25.66 ± 1.96	22.88 ± 1.87	17.79 ± 0.20	16.76 ± 0.33	45.16 ± 3.22	42.58 ± 2.81	43.02 ± 3.00

Table A.16: Accelerated 112912.06 Aluminum

Parameter	0a	0b	0c	1a	1b	2	3	4
x (in)	3.10	4.48	5.85	9.23	10.98	18.23	25.48	32.73
A_t (in^2)	35.06	35.06	35.06	44.62	44.62	44.62	44.62	44.62
ε	0.95	0.95	0.95	0.95	0.95	0.95	0.95	0.95
σ (W/m^2K^4)	5.67E-08	5.67E-08	5.67E-08	5.67E-08	5.67E-08	5.67E-08	5.67E-08	5.67E-08
t_p (in)	0.72	0.72	0.72	0.72	0.72	0.72	0.72	0.72
C_k	0.90	0.90	0.90	0.90	0.90	1.05	1.10	1.05
E (V)	6.08	6.08	6.08	5.90	5.90	5.98	6.26	6.08
I (A)	2.08	2.08	2.08	2.64	2.64	2.57	2.74	2.61
k_p (W/mK)	0.205	0.205	0.205	0.205	0.205	0.205	0.205	0.205
T_{SS} (K)	313.53	314.96	315.64	306.20	306.59	305.24	306.30	306.31
T_{UP} (K)	296.41	297.19	297.72	296.82	296.80	296.95	297.45	297.58
T_∞ (K)	293.65	293.65	293.65	293.65	293.65	293.65	293.65	293.65
T_{IR} (K)	303.53	305.44	306.46	302.33	301.78	299.93	300.45	301.27
h (W/m^2K)	33.50 ± 2.16	26.53 ± 1.96	23.79 ± 1.86	45.69 ± 1.26	48.66 ± 1.57	63.90 ± 2.87	65.90 ± 3.45	53.03 ± 2.49

REFERENCES

[1] Addy, H.E., 2000, "Ice Accretions and Icing Effects for Modern Airfoils," NASA/TP-2000-210031.

[2] Goraj, Z., 2004, "An Overview of the Deicing and Antiicing Technologies with Prospects for the Future," *24th International Congress of the Aeronautical Sciences* (ICAS), Yokohama.

[3] "14 CFR Part 25: Airworthiness Standards: Transport Category Airplanes – Appendix C, Part I: Atmospheric Icing Conditions," 2012, *Code of Federal Regulations*

[4] "14 CFR Part 25: Airworthiness Standards: Transport Category Airplanes – Appendix O, Part I: Metrology," 2014, *Code of Federal Regulations*

[5] Wright, W.B., and Bidwell, C.S., 2014, "How Roughness Research can Improve LEWICE," Invited Oral Presentation, 6th AIAA Atmospheric and Space Environments Conference, 16-20 June, Atlanta, GA.

[6] Shin, J., 1994, "Characteristics of Surface Roughness Associated with Leading Edge Ice Accretion," NASA TM-106459.

[7] Wright W.B., Rutkowski, A., 1999, "Validation Results for LEWICE 2.0," NASA, NASA/CR-1999-208690, Cleveland, OH.

[8] Tecson, L., 2013, "Convective Heat Transfer from Realistic Ice Roughness Distributions," MS thesis, Department of Mechanical Engineering, Baylor University.

[9] Walker, C.W., 2014, "Convection from Manufactured Ice Roughness with Varying Flux Boundary Conditions," MS thesis, Department of Mechanical Engineering, Baylor University.

[10] Shannon, T.A., 2015, "Convection from Realistic Ice Roughness on a Simulated NACA 0012 Airfoil," MS thesis, Department of Mechanical Engineering, Baylor University.

[11] Hughes, M.T., 2015, "Convective Enhancement on airfoil Due to Ice Roughness Elements in Stagnation Region Flows," MS thesis, Department of Mechanical Engineering, Baylor University.

[12] Hawkins, D.M., 2016, "Convection from Laser-Scanned Real Ice Roughness on a Simulated NACA 0012 Airfoil," MS thesis, Department of Mechanical Engineering, Baylor University.

[13] "Compliance of Transport Category Airplanes with Certification Requirements for Flight in Icing Conditions," 2014, AC No: 25-28.

[14] Ruff , G.A., 1986, "Analysis and Verification of the Icing Scaling Equations," AEDC-TR-85-30.

[15] Bragg, M.B., Hutchison, T., Merret, J., Oltman, R., Pokhariyal, D., 2000, "Effects of Ice Accretion on Aircraft Flight Dynamics," 38th AIAA Aerospace Sciences Meeting and Exhibit, 10-13 January, Reno, NV, AIAA-2000-0360.

[16] Anderson, D.N., Hentschel, D.B., and Ruff, G.A., 1998, "Measurement and Correlation of Ice Accretion Roughness," NASA-CR-2003-211823.

[17] Tsao, J.C., and Lee, S., 2012, "Evaluation of Icing Scaling on Swept NACA 0012 Airfoil Models." NASA CR-2012-217419.

[18] Tsao, J.C., and Kreeger, R.E., 2010, "Experimental Evaluation of Stagnation Point Collection Efficiency of the NACA 0012 Swept Wing Tip," AIAA-2009-4125 and NASA TM-2012-216102.

[19] Langmuir and Blodgett (1946) A Mathematical Investigation of Water Droplet Trajectories

[20] McClain, S.T., Vargas, M., and Tsao, J.C., 2017, "Ice Roughness and Thickness Evolution on a Swept NACA 0012 Airfoil," 9th AIAA Atmospheric and Space Environments Conference, 5-9 June, Denver, CO, AIAA-2017-3585.

[21] Hansman Jr., R.J, Yamaguchi, K., Berkowitz, B., and Potapczuk, M., 1990, "Modeling of Surface Roughness Effects on Glaze Ice Accretion," N90-20925.

[22] Olsen, W., Walker, E., 1986, "Experimental Evidence for Modifying the Current Physical Model for Ice Accretion on Aircraft Surfaces." NASA TM-87184.

[23] Anderson, J.D. Jr., 2005, "Ludwig Prandtl's Boundary Layer," Physics Today, American Institute of Physics, S-0031-9228-0512-020-1

[24] Munson, B.R., Young, D.F., Okiishi, T.H., and Huebsch, W.W., 2009, *Fundamentals of Fluid Mechanics,* 6th ed., John Wiley & Sons, Inc., Hoboken, NJ.

[25] Bejan, A., 2004, *Convection Heat Transfer,* 3rd ed, John Wiley & Sons, Inc., Hoboken, NJ.

[26] Bergman, T.L., Lavine, A.S., Incropera, F.P., and Dewitt, D.P., 2011, *Fundamentals of Heat and Mass Transfer,* 7th ed., John Wiley & Sons, Inc., Hoboken, NJ.

[27] Smith, A.G., and Spaulding, D.B., 1958, "Heat Transfer in a Laminar Boundary Layer with Constant Fluid Properties and Constant Wall Temperature," *J. Roy. Aero. Soc.,* Vol. 62, pg 60-64.

[28] Ambrok, G.S., 1957, "Approximate Solutions of the Equations for the Thermal Boundary Layer with Variations in the Boundary Layer Structure," *Soviet Phys.-Tech. Phys.,* Vol. 2, No. 9, pg 1979-1986.

[29] Messinger, B.L., 1953, "Equilibrium Temperature of an Unheated Icing Surface as a Function of Airspeed," *Journal of Aeronautical Sciences,* pp. 29-42.

[30] Poinsatte, P.E., Van Fossen, G.J., and DeWitt, K.J., 1990, "Convective Heat Transfer Measurements from a NACA 0012 Airfoil in Flight and in the NASA Lewis Icing Research Tunnel," NASA TM-102448.

[31] Nikuradse, J., 1933, "Laws for Flow in rough Pipes," *VDI-Forschungsheft,* **4**, pp.361.

[32] Schlichting, H., 1936, "Experimental Investigation on the Problem of Surface Roughness," TM-832, National Advisory Committee on Aeronautics.

[33] Wright, W.B., 2002, "User Manual for the NASA Glenn Ice Accretion Code LEWICE," NASA/CR-2002-211793.

[34] Bons, J.P., 2002, "St and Cf Augmentation for Real Turbine Roughness with Elevated Freestream Turbulence," *Journal of Turbomachinery,* **124**, pp. 632-644

[35] Bons J.P., and McClain, S.T., 2004, "The Effect of Real Turbine Roughness with Pressure Gradient on Heat Transfer," *Journal of Turbomachinery,* Vol. 126, No. 3, pg 385-394.

[36] Vargas, M., 2007, "Current Experimental Basis for Modeling Ice Accretions on Swept Wings," *Journal of Aircraft,* **44**(1), pp. 274-290.

[37] Bragg, M.B., Kerho, M.F., and Cummings, M.J., 1994, "Effect of Initial Ice Roughness on Airfoil Aerodynamics," AIAA-94-0800.

[38] Bragg, M.B., Cummings, M.J., Lee, S., and Henze, C.M., 1996, "Boundary-Layer and Heat-Transfer Measurements on an Airfoil with Simulated Ice Roughness," AIAA-96-0866.

[39] Dunkhan, N., Van Fossen, G.J., DeWitt, K.J., and Masiulaniec, K.C., 2003, "Experimental Frossling Numbers for Ice-Roughened NACA 0012 Airfoils," *Journal of Aircraft,* **40**(6), pp. 1161-1167.

[40] Han, Y., and Palacios, J., 2014, "Transient Heat Transfer Measurements of Surface Roughness due to Ice Accretion," 6th AIAA Atmospheric and Space Environments Conference, 16-20 June, Atlanta, GA, AIAA-2014-2464.

[41] Croce, G., De Candido, E., Habashi, W.G., Munzar, J., Aubé, M.S., Baruzzi, G.S., and Aliaga, C., 2010, "FENSAP-ICE: Analytical Model for Spatial and Temporal Evolution of In-Flight Icing Roughness," *Journal of Aircraft,* **47**(4), pp. 1283-1289.

[42] Tecson, L., and McClain, S.T., 2013, "Modeling of Realistic Ice Roughness Element Distributions to Characterize Convective Heat Transfer," 5th AIAA Atmospheric and Space Environments Conference, 24-27 June, San Diego, CA, AIAA-2013-3059.

[43] Tecson, L., and McClain, S.T., 2013, "Convective Enhancement of Surfaces with Realistic Ice Roughness Distributions," 5th AIAA Atmospheric and Space Environments Conference, 24-27 June, San Diego, CA, AIAA-2013-3060.

[44] Walker, C.W., McClain, S.T., and Shannon, T.A., 2014, "Convection from Ice Roughness with Varying Flux Boundary Conditions," 6th AIAA Atmospheric and Space Environments Conference, 16-20 June, Atlanta, GA, AIAA-2014-2463.

[45] McClain, S.T., Reed, D., Vargas, M., Kreeger, R.E., and Tsao, J.C., 2014, "Ice Roughness in Short Duration SLD Icing Events," 6th AIAA Atmospheric and Space Environments Conference, 16-20 June, Atlanta, GA, AIAA-2014-2330.

[46] McClain, S.T., Vargas, M., Kreeger, R.E., and Tsao, J., 2015, "A Reevaluation of Appendix C Ice Roughness Using Laser Scanning," SAE Technical Paper 2015-01-2098, 2015, doi:10.4271/2015-01-2097.

[47] McClain, S.T., and Kreeger, R.E., 2013, "Assessment of Ice Shape Roughness Using a Self-Organizing Map Approach," 5th AIAA Atmospheric and Space Environments Conference, 24-27 June, San Diego, CA, AIAA-2013-2546

[48] Shannon, T.A., and McClain, S.T., 2015, "Convection from Simulated NACA 0012 Airfoil with Realistic Ice Accretion Roughness Variations," SAE Technical Paper 2015-01-2097, 2015, doi:10.4721/2015-01-2097.

[49] Hughes, M.T., McClain, S.T., Vargas, M., and Broeren, A., 2015, "Convective Enhancement of Icing Roughness Elements in Stagnation Region Flows," 7th AIAA Atmospheric and Space Environments Conference, 22-26 June, Dallas, TX, AIAA 2015-3021.

[50] McClain Vargas Tsao (2016) Characterization of Roughness Variations in Scaled Glaze Icing Conditions

[51] Reehorst, A.L., and Richter, G.P., 1987, "New Methods for Molding and Casting Ice Formations," NASA TM-100126.

[52] Hovenac, E.A., Vargas, M, 1995, "A Laser-Based Shape Profilometer for Use in Icing Wind Tunnels," NASA TM-106936.

[53] Lee, S., Broeren, A.P., Addy Jr., H.A., Sills, R., and Pifer, E.M., 2012, "Development of 3-D Ice Accretion Measurement Method," NASA TM-2012-217702.

[54] McClain, S.T., Tiňo, P., and Kreeger, R.E., 2011, "Ice Shape Characterization Using Self-Organizing Maps," *Journal of Aircraft,* **48**(2), pp. 724-729.

[55] McClain, S.T., 2016, "Airfoil Roughness Evaluation System (ARES) User's Manual," Version 0.1, Unpublished.

[56] McClain, S.T., 2016, "Manual Point Cloud Registration for Combined Ice Roughness and Ice Thickness Measurements," 8th AIAA Atmospheric and Space Environments Conference, June 13-17, Washington, DC, AIAA-2016-3590.

[57] The International Association for the Properties of Water and Steam, 2007, "Revised Release on the IAPWS Industrial Formulation 1997 for the Thermodynamic Properties of Water and Steam," http://www.iapws.org/.

[58] Wilke, C.R., 1950, "A Viscosity Equation for Gas Mixtures," *Journal of Chemical Physics,* **18**(4), pp. 517-519.

[59] White, F.M., 2006, *Viscous Fluid Flow,* 3rd Ed, Boston, McGraw-Hill, Inc., New York, NY.

[60] Coleman, H.W., and Steele, W.G., 1999, *Experimentation and Uncertainty Analysis for Engineers,* 2nd Ed., John Wiley & Sons, Inc., Hoboken, NJ.

[61] Kline, S.J., and McClintock, F.A., 1953, "Describing Uncertainties in Single Sample Experiments," *Mechanical Engineering,* **75**, pp. 3-8.

[62] McCarrell, J., Shannon, T.A., and McClain, S.T., "Convection from Surfaces with Ice Roughness Characterized at Increasing Accumulation Times," unpublished.